



GRANT / LEWIS

A COMPARISON OF EXPERIMENTAL AND THEORETICAL
RESULTS FOR LEAKAGE, PRESSURE GRADIENTS, AND
ROTORDYNAMIC COEFFICIENTS FOR TAPERED ANNULAR GAS SEAL

Prepared by

David Alan Elrod, Res. Asst.
Dara W. Childs, Professor

September 1986
TRC-SEAL-4-86

IN-28452

{NASA-CR-179709} A COMPARISON OF
EXPERIMENTAL AND THEORETICAL RESULTS FOR
LEAKAGE, PRESSURE GRADIENTS, AND
ROTORDYNAMIC COEFFICIENTS FOR TAPERED
ANNULAR GAS SEAL Progress Report {Texas A&M G3/37

N86-32742

Unclas
44592

**Turbomachinery Laboratories
Mechanical Engineering Department**

Texas A&M University

College Station, Texas 77843-3123

**A COMPARISON OF EXPERIMENTAL AND THEORETICAL RESULTS
FOR LEAKAGE, PRESSURE GRADIENT, AND ROTORDYNAMIC COEFFICIENTS
FOR TAPERED ANNULAR GAS SEAL**

PROGRESS REPORT

NASA GRANT NAG3-181

**Prepared by
DAVID ALAN ELROD
Research Assistant**

**Dara W. Childs, Ph.D, P.E.
Principal Investigator**

September 1986

TRC-SEAL-4-86

ABSTRACT

A Comparison of Experimental and Theoretical Results
for Leakage, Pressure Gradient, and Rotordynamic Coefficients
for Tapered Annular Gas Seals. (December 1986)

David Alan Elrod, B.S., Louisiana State University

Co-Chairs of Advisory Committee: Dr. Dara Childs
Dr. Clayton Nelson

A brief review of current annular seal theory and a discussion of the predicted effect on stiffness of tapering the seal stator are presented. An outline of Nelson's analytical-computational method for determining rotordynamic coefficients for annular compressible-flow seals is included. Modifications to increase the maximum rotor speed of an existing air-seal test apparatus at Texas A&M University are described. Experimental results, including leakage, entrance-loss coefficients, pressure distributions, and normalized rotordynamic coefficients, are presented for four convergent-tapered, smooth-rotor, smooth-stator seals. A comparison of the test results shows that an inlet-to-exit clearance ratio of 1.5 to 2.0 provides the maximum direct stiffness, a clearance ratio of 2.5 provides the greatest stability, and a clearance ratio of 1.0 provides the least stability. The experimental results are compared to theoretical results from Nelson's analysis with good agreement. Test results for cross-coupled stiffness show less sensitivity to fluid prerotation than predicted.

PRECEDING PAGE BLANK NOT FILMED

ACKNOWLEDGEMENT

This project was supported in part by NASA Grant NAS8-33716 from NASA Lewis Research Center and AFOSR Contract F49620-82-K-0033.

TABLE OF CONTENTS

	Page
ABSTRACT	iii
ACKNOWLEDGEMENT.	iv
TABLE OF CONTENTS	v
LIST OF TABLES	vii
LIST OF FIGURES	viii
NOMENCLATURE	xiii
CHAPTER	
I INTRODUCTION	1
II ANNULAR SEAL ANALYSIS REVIEW	5
III NELSON'S ANALYSIS	10
IV TEST METHOD AND APPARATUS.	16
Test method	16
Test apparatus.	19
V TEST APPARATUS: INTRODUCTION.	24
Normalized parameters	28
Relative uncertainty.	32
Selection of report data.	34
VI TEST RESULTS: RELATIVE PERFORMANCE OF SEALS	35
Leakage	35
Direct stiffness.	35
Cross-coupled stiffness	38
Direct damping.	43
Stability analysis.	43
VII TEST RESULTS: COMPARISON TO THEORETICAL PREDICTIONS.	50
Dependence on inlet loss coefficients	50
Comparison of Nelson's analyses	55
Static results comparison	55

CHAPTER	Page
Dynamic results comparison	60
Direct stiffness	60
Direct damping	63
Cross-coupled stiffness.	63
Stability analysis	68
VIII CONCLUSIONS	72
REFERENCES	75
APPENDIX	77

LIST OF TABLES

	Page
Table 1. Test stator specifications	26
Table 2. Test rotor specifications.	26
Table 3. Test seal specifications	27
Table 4. Definitions of symbols used in figures	27
Table 5. Growth of rotor with rotational speed.	31
Table 6. Normalized coefficients.	31

LIST OF FIGURES

	Page
Fig. 1 Small motion of a seal rotor about an eccentric position.	6
Fig. 2 Small motion of a seal rotor about a centered position.	6
Fig. 3 External shaker method used for coefficient identification.	17
Fig. 4 Test apparatus assembly	20
Fig. 5 Cross-sectional view of test section showing rotor-shaft assembly.	22
Fig. 6 Detail of tapered stator.	25
Fig. 7 Inlet circumferential velocity vs. pressure ratio for straight bore seal.	29
Fig. 8 Inlet circumferential velocity vs. pressure ratio for 1.5 taper seal.	29
Fig. 9 Inlet circumferential velocity vs. pressure ratio for 2.0 taper seal.	30
Fig. 10 Inlet circumferential velocity vs. pressure ratio for 2.5 taper seal.	30
Fig. 11 Running speed dependence of direct stiffness of seal 1.0 at different pressure ratios before and after normalization	33
Fig. 12 Experimental mass flow rates through the test seals at 3.08 bar pressure.	36
Fig. 13 Experimental mass flow rates through the test seals at 8.25 bar pressure.	37
Fig. 14 Experimental normalized direct stiffnesses of the test seals at 3.08 bar pressure	39
Fig. 15 Experimental normalized direct stiffnesses of the test seals at 8.25 bar pressure	40

	Page
Fig. 16 Experimental normalized cross-coupled stiffnesses of the test seals at 3.08 bar pressure.	41
Fig. 17 Experimental normalized cross-coupled stiffnesses of the test seals at 8.25 bar pressure.	42
Fig. 18 Experimental normalized direct damping of the test seals at 3.08 bar pressure	44
Fig. 19 Experimental normalized direct damping of the test seals at 8.25 bar pressure	45
Fig. 20 Forces on a precessing seal rotor	46
Fig. 21 Whirl frequency ratios of seal 1.0.	48
Fig. 22 Whirl frequency ratios of seal 1.5.	48
Fig. 23 Whirl frequency ratios of seal 2.0.	49
Fig. 24 Whirl frequency ratios of seal 2.5.	49
Fig. 25 Dependence of stiffness and damping on entrance loss coefficient.	51
Fig. 26 Pressure gradient in seal 1.0, pressure 1, inlet swirl 4 of Table 4.	53
Fig. 27 Entrance loss for seal 1.0, high velocity swirl in the direction of rotor rotation	54
Fig. 28 Direct stiffness, comparison of Nelson's analyses .	54
Fig. 29 Cross-coupled stiffness, comparison of Nelson's analyses.	56
Fig. 30 Direct damping, comparison of Nelson's analyses . .	56
Fig. 31 Experimental and theoretical mass flow rates of air through the test seals at 3.08 bar pressure . .	57
Fig. 32 Experimental and theoretical mass flow rates of air through the test seals at 8.25 bar pressure . .	58
Fig. 33 Experimental and theoretical normalized direct stiffnesses of the test seals at 3.08 bar pressure.	61
Fig. 34 Experimental and theoretical normalized direct stiffnesses of the test seals at 8.25 bar pressure.	62

	Page
Fig. 35 Experimental and theoretical normalized direct damping of the test seals at 3.08 bar pressure. . .	64
Fig. 36 Experimental and theoretical normalized direct damping of the test seals at 8.25 bar pressure. . .	65
Fig. 37 Experimental and theoretical normalized cross-coupled stiffnesses of the test seals at 3.08 bar pressure.	66
Fig. 38 Experimental and theoretical normalized cross-coupled stiffnesses of the test seals at 8.25 bar pressure.	67
Fig. 39 Theoretical whirl frequency ratios of seal 1.0 at 16000 rpm.	69
Fig. 40 Theoretical whirl frequency ratios of seal 1.5 at 16000 rpm.	69
Fig. 41 Theoretical whirl frequency ratios of seal 2.0 at 16000 rpm.	70
Fig. 42 Theoretical whirl frequency ratios of seal 2.5 at 16000 rpm.	70
Fig. A1 Mass flow rate of air through seal 1.0 at 3000 rpm and 16000 rpm	78
Fig. A2 Mass flow rate of air through seal 1.5 at 3000 rpm and 16000 rpm	79
Fig. A3 Mass flow rate of air through seal 2.0 at 3000 rpm and 16000 rpm	80
Fig. A4 Mass flow rate of air through seal 2.5 at 3000 rpm and 16000 rpm	81
Fig. A5 Normalized direct stiffness of seal 1.0 at 3000 rpm and 16000 rpm	82
Fig. A6 Normalized direct stiffness of seal 1.5 at 3000 rpm and 16000 rpm	83
Fig. A7 Normalized direct stiffness of seal 2.0 at 3000 rpm and 16000 rpm	84
Fig. A8 Normalized direct stiffness of seal 2.5 at 3000 rpm and 16000 rpm	85

	Page
Fig. A9 Normalized cross-coupled stiffness of seal 1.0 at 3000 rpm and 16000 rpm.	86
Fig. A10 Normalized cross-coupled stiffness of seal 1.5 at 3000 rpm and 16000 rpm.	87
Fig. A11 Normalized cross-coupled stiffness of seal 2.0 at 3000 rpm and 16000 rpm.	88
Fig. A12 Normalized cross-coupled stiffness of seal 2.5 at 3000 rpm and 16000 rpm.	89
Fig. A13 Normalized direct damping of seal 1.0 at 3000 rpm and 16000 rpm	90
Fig. A14 Normalized direct damping of seal 1.5 at 3000 rpm and 16000 rpm	91
Fig. A15 Normalized direct damping of seal 2.0 at 3000 rpm and 16000 rpm	92
Fig. A16 Normalized direct damping of seal 2.5 at 3000 rpm and 16000 rpm	93
Fig. A17 Entrance loss of seal 1.0, inlet air swirls 1 and 2 from Table 4.	94
Fig. A18 Entrance losses of seal 1.0, inlet air swirl 3 and 4 of Table 4.	95
Fig. A19 Entrance losses of seal 1.5, inlet air swirl 1 and 2 of Table 4.	96
Fig. A20 Entrance losses of seal 1.5, inlet air swirls 3 and 4 of Table 4.	97
Fig. A21 Entrance losses of seal 1.5 inlet air swirl 5 and seal 2.0 inlet air swirl 1.	98
Fig. A22 Entrance losses of seal 2.0, inlet air swirls 2 and 3	99
Fig. A23 Entrance losses of seal 2.0, inlet air swirls 4 and 5	100
Fig. A24 Entrance losses of seal 2.5, inlet air swirl 1 and 2	101

	Page
Fig. A25 Entrance losses of seal 2.5, inlet air swirls 3 and 4	102
Fig. A26 Entrance losses of seal 2.5, inlet air swirl 5. . .	103
Fig. A27 Pressure gradients of seal 1.0, inlet swirl 1 . . .	103
Fig. A28 Pressure gradients of seal 1.0, inlet air swirls 2 and 3	104
Fig. A29 Pressure gradients of seal 1.0, inlet air swirls 4 and 5	105
Fig. A30 Pressure gradients of seal 1.5, inlet air swirls 1 and 2	106
Fig. A31 Pressure gradients of seal 1.5, inlet air swirls 3 and 4	107
Fig. A32 Pressure gradients of seal 1.5 inlet air swirl 5 and seal 2.0 inlet air swirl 1.	108
Fig. A33 Pressure gradients of seal 2.0, inlet air swirls 2 and 3	109
Fig. A34 Pressure gradients of seal 2.0, inlet air swirls 4 and 5	110
Fig. A35 Pressure gradients of seal 2.5, inlet air swirls 1 and 2	111
Fig. A36 Pressure gradients of seal 2.5, inlet air swirls 3 and 4	112
Fig. A37 Pressure gradients of seal 2.5, inlet air swirl 5 .	113

NOMENCLATURE

A, B	= Fourier coefficients for rotor motion
C, c	= direct and cross-coupled damping coefficients (FT/L)
e	= surface roughness (L)
e_o	= displacement of seal rotor from centered position (L)
f	= fanning friction factor
H_i	= inlet seal clearance (L)
H_o	= exit seal clearance (L)
\bar{H}	= average seal clearance (L)
K, k	= direct and cross-coupled stiffness coefficients (F/L)
\bar{k}	= entrance-loss coefficient
M, m	= direct and cross-coupled added-mass coefficients (M)
\dot{m}	= fluid mass flow rate (M/T)
n_o, m_o	= Hirs' coefficients
p	= fluid pressure (F/L ²)
R	= seal radius (L)
R_z	= $2\rho U_z C / \mu$ = nominal axial Reynolds number
R_e	= $2\rho UC / \mu$ = nominal Reynolds number
U	= $\sqrt{(U_\theta)^2 + (U_z)^2}$ = mean fluid flow velocity (L/T)
U_θ	= mean fluid circumferential velocity (L/T)
U_z	= mean fluid axial velocity (L/T)
X, Y	= radial seal displacements (L)
γ	= ratio of specific heats for air
ϵ_o	= e_o / C_r = equilibrium eccentricity ratio
μ	= fluid viscosity (FT/L ²)

- ρ = fluid density (M/L^3)
 τ = fluid shear stress (F/L^2)
 ϕ = fluid preswirl angle (rad)
 ω = shaft angular velocity ($1/T$)
 Ω = shaft precessional velocity ($1/T$)
 μ = fluid viscosity (FT/L^2)

Subscripts

- r rotor
s stator
z axial
 θ circumferential

CHAPTER I

INTRODUCTION

Recent trends in turbomachinery design have been toward increased speeds, tighter clearances, and higher power to weight ratios. As a result, problems with vibration and dynamic stability have become more critical. To industrial plants, the cost of equipment outage can be devastating. The ability to predict and/or modify the dynamic characteristics of turbomachines can reduce this cost.

Most vibrations detected in rotating machinery are caused by orbital motion of the rotor. If the frequency of this motion coincides with the rotational speed of the rotor, the vibration is called "synchronous". "Subsynchronous" vibration refers to an orbital frequency below the rotational speed.

The most frequent cause of synchronous vibration is unbalance in the rotor. The response to unbalance is also called forced vibration because the unbalance exerts a rotating force on the rotor as it spins. Synchronous vibration amplitude reaches a relative maximum when the rotor rotational speed coincides with a damped natural frequency of the rotor. Damping in the rotor system helps to reduce the peak synchronous vibration levels. If critical speeds must be traversed during start-up and shut-down of a turbomachine, the designer aspires to introduce additional damping into the system.

Journal Model: ASME Journal of Tribology

Subsynchronous vibration problems are far less frequent in practice than synchronous. Self-excited motion is a type of subsynchronous vibration which can be particularly destructive. It is often the result of a tangential force acting on the rotor due to some fluid or friction mechanism. This motion occurs at a natural frequency of the rotor below the running speed. Motion which is self-excited appears suddenly at some threshold speed with large amplitudes which sustain or grow as the running speed increases. The consequences range from the prevention of running speed increases to catastrophic failure of the equipment.

The forces developed in annular seals can play a role in both synchronous and self-excited vibration. Black et al. [1 - 3] have demonstrated the critical effects that forces developed by neck-ring and interstage seals have on the rotordynamic behavior of pumps. Also, stability difficulties with the Space Shuttle Main Engine (SSME) high-pressure fuel turbopump [4] have prompted further research into the forces developed by liquid seals.

Experiences have shown that various gas seal configurations can similarly influence the rotordynamic behavior of turbomachines. For example, in the high-pressure oxygen turbopump (HPOTP) of the SSME, initial vibration problems were remedied by changing the turbine interstage seal from a stepped-labyrinth configuration to a convergent taper seal with a honeycomb stator and a smooth rotor [5]. Compressible flow in annular seals has been analyzed by Fleming [6, 7] and Nelson [8 - 10]. Both Fleming [6] and Nelson [9] suggest that

the inlet to exit clearance ratio in a tapered seal can be optimized to improve rotordynamic behavior by maximizing seal stiffness. Nelson et al. [11] have reported experimental leakage, stiffness, and damping data on two smooth rotor/smooth stator seals in which a tapered seal with an inlet to exit clearance ratio of 1.5 was shown to be stiffer than a straight bore seal. No dependence of seal behavior on rotor speed was noted through the 8000 rpm maximum speed of these tests. Comparisons of the experimental data to the predictions of Nelson's analysis [9] showed Nelson underpredicts stiffness. Furthermore, the underprediction grew worse as the relative roughness, $e/2H_0$, of the seal increased. There have been no comparisons of experimental data to Nelson's most recent analysis [10].

The purpose of this report is threefold. Modifications on an existing air seal test apparatus at Texas A & M University are described, which make seal tests at rotor speeds up to 16000 rpm possible. A comparison of experimental data is provided from the tests of four smooth rotor/smooth stator seals with different inlet to exit clearance ratios. A comparison is provided between theoretically-predicted and experimentally-obtained data for the four seals. The leakage of the working fluid through the seal, the pressure gradient along the seal length, entrance pressure-loss data, and rotordynamic coefficients provide a basis for comparison. A short discussion on seal theory is included, as is a description of the rotordynamic identification scheme used. The work presented

herein is intended to add to the database on seal forces and to determine the validity of a theoretical analysis for predicting those forces.

CHAPTER II

ANNULAR SEAL ANALYSIS REVIEW

As related to rotordynamics, seal analysis has the objective of determining the reaction forces acting on the rotor arising from shaft motion within the seal. Due to similarities between plain journal bearings and annular seals, seal analysis is generally based on governing equations which have previously been developed for bearings.

Annular seals and plain bearings are geometrically similar, but seals typically have radial clearance-to-radius ratios on the order of 0.005, versus C_r/R ratios of 0.001 for bearings. Due to seal clearances and pressure differentials, fully-developed turbulent flow normally exists. Also, seals are nominally designed to operate in a centered position. Journal bearings, on the other hand, have operating eccentricities which vary with running speed and load. Therefore, most of the rotordynamic work for bearings has been done to determine dynamic coefficient versus eccentricity relationships.

Two linearized seal models, expressed in terms of dynamic coefficients, have been suggested for the motion/reaction-force relationship. For small motions of the rotor about an arbitrary position in the seal, as shown in Fig.1, the relation can be written

$$-\begin{Bmatrix} F_X \\ F_Y \end{Bmatrix} = \begin{bmatrix} K_{XX}(\epsilon_0) & K_{XY}(\epsilon_0) \\ K_{YX}(\epsilon_0) & K_{YY}(\epsilon_0) \end{bmatrix} \begin{Bmatrix} X \\ Y \end{Bmatrix} + \begin{bmatrix} C_{XX}(\epsilon_0) & C_{XY}(\epsilon_0) \\ C_{YX}(\epsilon_0) & C_{YY}(\epsilon_0) \end{bmatrix} \begin{Bmatrix} \dot{X} \\ \dot{Y} \end{Bmatrix} + \begin{bmatrix} M_{XX}(\epsilon_0) & M_{XY}(\epsilon_0) \\ M_{YX}(\epsilon_0) & M_{YY}(\epsilon_0) \end{bmatrix} \begin{Bmatrix} \ddot{X} \\ \ddot{Y} \end{Bmatrix} \quad (1)$$

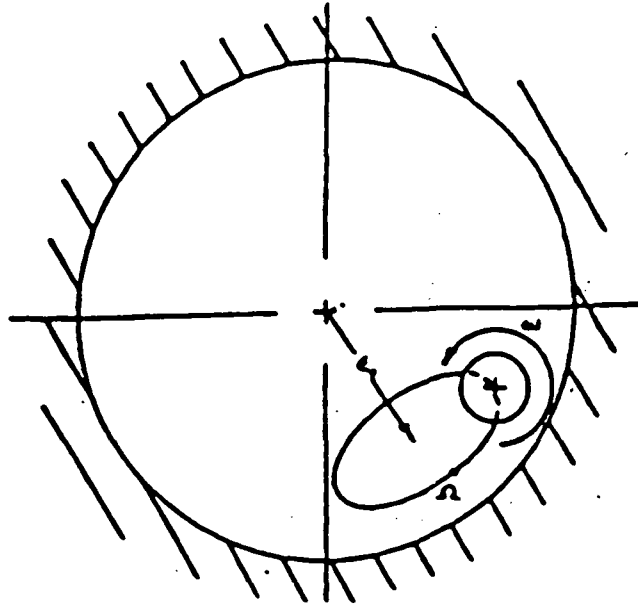


Fig. 1 Small motion of a seal rotor about an eccentric position (ω is the rotor spin speed, Ω is the precessional orbit frequency).

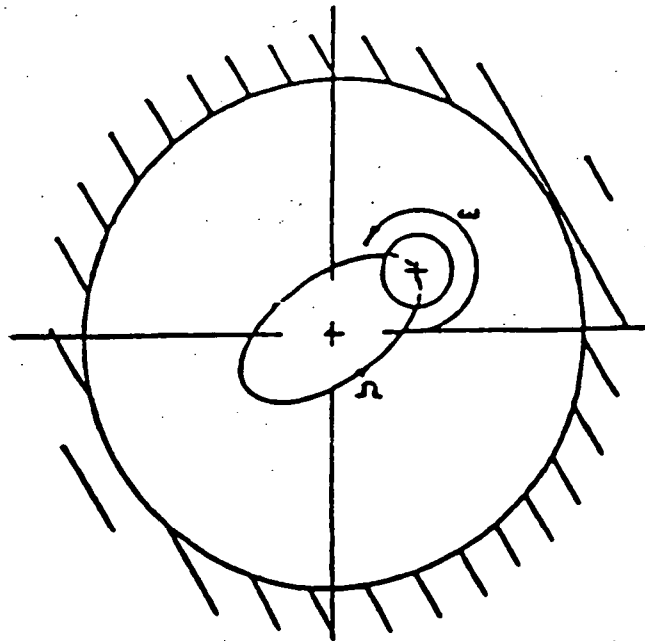


Fig. 2 Small motion of a seal rotor about a centered position (ω is the rotor spin speed, Ω is the precessional orbit frequency).

In this equation, $\{X, Y\}$ define the motion of the seal rotor relative to its stator, $\{F_x, F_y\}$ are the components of the reaction force acting on the rotor, and the dynamic coefficients $\{K_{xx}, K_{yy}, C_{xx}, C_{yy}, M_{xx}, M_{yy}\}$ and $\{K_{xy}, K_{yx}, C_{xy}, C_{yx}, M_{xy}, M_{yx}\}$ represent the "direct" and "cross-coupled" stiffness, damping, and added-mass terms, respectively. These coefficients are functions of the equilibrium eccentricity ratio $\epsilon_0 = e_0 / C_r$, where the eccentricity ratio ϵ_0 equals the displacement (e_0) of the rotor from the centered position divided by the nominal radial clearance (C_r). The term "cross-coupled" refers to the coupling effect exhibited by the off-diagonal terms; specifically, motion in one plane introduces reaction forces in an orthogonal one. These cross-coupled terms arise from the fluid's circumferential velocity component, and show a strong dependency on both the magnitude and direction (with respect to rotor rotation) of the fluid velocity. This circumferential velocity component may arise from the prerotation of the fluid as it enters the seal due to some rotating element upstream, or it may develop as the fluid passes through the seal, with rotor shear forces "dragging" the viscous fluid around its periphery. The cross-coupled stiffness term usually produces a destabilizing force component, and, therefore, is of considerable interest. The cross-coupled damping and added-mass terms are generally much less influential than the cross-coupled stiffness term with respect to stability. For no fluid rotation, these cross-coupled terms are zero.

The second linearized seal model applies for small motions of

the rotor about a centered position in the seal, as shown in Fig. 2.

This model can be expressed

$$-\begin{Bmatrix} F_X \\ F_Y \end{Bmatrix} = \begin{bmatrix} K & k \\ -k & K \end{bmatrix} \begin{Bmatrix} X \\ Y \end{Bmatrix} + \begin{bmatrix} C & c \\ -c & C \end{bmatrix} \begin{Bmatrix} \dot{X} \\ \dot{Y} \end{Bmatrix} + \begin{bmatrix} M & m \\ -m & M \end{bmatrix} \begin{Bmatrix} \ddot{X} \\ \ddot{Y} \end{Bmatrix} \quad (2)$$

where the dynamic coefficient matrices are skew-symmetric.

Theoretical work on annular seals has been done for both incompressible and compressible fluids. Black et al. [12] have developed analytical "short-seal" solutions for incompressible seals, which account for circumferential fluid flow due to wall shear stresses but not pressure perturbations. The analysis employs a bulk-flow assumption and accounts for fluid prerotation as it enters the seal. Childs' [13] incompressible seal analysis provides "finite-length" solutions, in which both shear and pressure-induced flow are included. Childs utilizes Hirs' [14] turbulent bulk-flow model, and accounts for inlet swirl as well as perturbations in axial and circumferential Reynolds numbers due to clearance perturbations.

Compressible flow in seals has been analyzed by Fleming [6, 7] and Nelson [9]. Fleming presents a short seal solution for the leakage, direct stiffness, and direct damping coefficients of straight and tapered, smooth, annular gas seals. However, he does not include the effects of the circumferential momentum equation, and thus cannot obtain the cross-coupled terms. Nelson includes the effect of circumferential momentum in analyzing both smooth and surface-roughened annular seals in the straight and tapered

configurations, and he solves for the cross-coupled coefficients. Nelson has developed two analyses, one of which [8, 9] is based on Hirs' [14] turbulent bulk-flow model. The other [10], which is used for comparison in this report, is a bulk-flow analysis which utilizes Moody's friction factor equation [15]. An outline of Nelson's analysis is included in the section that follows.

One interesting result of Fleming's analysis which was later supported by Nelson's analysis concerned the behavior of convergent-tapered seals. A convergent-tapered seal is one which has an inlet clearance which is larger than the exit clearance. Both Fleming and Nelson predict that if the inlet clearance of a constant clearance annular seal is increased while the exit clearance is held constant, the direct stiffness of the seal will increase to a point and then decrease as the inlet clearance is increased further. Nelson et al. [11] have reported on the experimental verification of an increase of stiffness with taper (inlet to exit clearance ratio). An experimental investigation of the effect of taper on rotordynamic coefficients is included in this report.

CHAPTER III

NELSON'S ANALYSIS

Nelson [8-10] has developed analyses which provide both static and dynamic results for annular gas seals. The static results include fluid leakage through the seal, pressure gradient along the seal axis, and the fluid axial and circumferential velocities through the seal. Dynamic data provided by the analyses consist of the rotordynamic coefficients (direct and cross-coupled stiffness and damping terms) for small rotor motion about a centered position (equation (2)). Nelson assumes that the added-mass terms are negligible for gas seals, and, hence, equation (2) is written

$$-\begin{Bmatrix} F_X \\ F_Y \end{Bmatrix} = \begin{bmatrix} K & k \\ -k & K \end{bmatrix} \begin{Bmatrix} X \\ Y \end{Bmatrix} + \begin{bmatrix} C & c \\ -c & C \end{bmatrix} \begin{Bmatrix} \dot{X} \\ \dot{Y} \end{Bmatrix}. \quad (3)$$

In one approach, Nelson [8,9] utilizes a modified Hirs' [14] turbulent bulk-flow fluid model to develop governing axial and circumferential momentum equations, and his model is completed by the continuity and energy equations. Hirs' model assumes that the rotor and stator friction factors (f_r and f_s , respectively) can be written as:

$$f = no(R_e)^{mo} \quad (4)$$

where R_e is the Reynolds number relative to the surface upon which the shear stress is acting, and the constants no and mo are generally empirically determined from static pressure flow experiments.

Comparisons of the predictions of this model with experimental results [16] show that the model underpredicts the experimentally measured direct stiffness. Furthermore, this underprediction worsens as the relative roughness ($e/2H$) of the seal increases.

In another bulk-flow analysis, Nelson [10] uses Moody's pipe friction formula [15]. Previously used by von Pragenau [17] in an incompressible seal analysis, this formula approximates the Moody chart:

$$f = 0.001375 \{ 1 + [20000 e/2H + (10)^6 / R_e]^{1/3} \} \quad (5)$$

where e is the roughness ("bump" height), H is the seal clearance, $2H$ is the hydraulic diameter, and R_e is the Reynolds number relative to the surface upon which the shear stress is acting. This equation gives friction factors within 5% of those in Moody's diagram for Reynolds numbers between 4000 and 10^7 and values of $e/2H$ up to 0.01. For $e/2H > 0.01$, equation (5) significantly underestimates the friction factor. The Reynolds numbers at the stator, R_{es} , and rotor, R_{er} , are

$$R_{es} = \rho (2H) (U_z^2 + U_\theta^2)^{1/2} / \mu$$

$$R_{er} = \rho (2H) [U_z^2 + (U_\theta - R\omega)^2]^{1/2} / \mu$$

where U_z and U_θ are the axial and circumferential components of the mean fluid velocity, ρ is the fluid density, μ is the fluid viscosity, R is the seal radius, and ω is the rotor speed in radians per second. As applied to an annular pressure seal, f_s and f_r

become:

$$f_s = 0.001375 \left\{ 1 + \left[\frac{(10)^4 e_s}{H} + \frac{5(10)^5 \mu}{\rho H (U_z^2 + U_\theta^2)^{1/2}} \right]^{1/3} \right\} \quad (6)$$

$$f_r = 0.001375 \left\{ 1 + \left[\frac{(10)^4 e_r}{H} + \frac{5(10)^5 \mu}{\rho H [U_z^2 + (U_\theta^2 - R\omega)^2]^{1/2}} \right]^{1/3} \right\} \quad (7)$$

For this report, the rotor and stator surface roughnesses were determined using a profilometer.

Assuming small motion of the rotor about a centered position, Nelson uses a perturbation analysis similar to that employed by Childs [13] to develop zeroth and first-order perturbation equations. The zeroth-order solution represents a zero-eccentricity flow condition, with rotor rotation but without precession. This solution is developed iteratively and yields the mass-leakage flow rate, and the axial distribution of pressure, axial velocity, density, and circumferential velocity. The iterative solution scheme uses initial guesses for the zeroth-order seal entrance Mach number and entrance pressure-loss coefficient. The entrance-loss relationship is defined by

$$p_o(0) = \{1 + [(\gamma-1)(\bar{k}+1)M_o^2(0)] / 2\}^{\gamma/(1-\gamma)} \quad (8)$$

where $p_o(0)$ is the seal entrance/reservoir pressure ratio and $M_o(0)$ is the entrance Mach number. The entrance Mach number is iteratively

adjusted, and the loss coefficient \bar{k} is recalculated for a given seal according to the empirical relationship

$$\bar{k} = a + b(R_z)^c \quad (9)$$

In equation (9), R_z is the axial Reynolds number, and a , b , and c are constants calculated from test data and provided as input parameters for Nelson's analysis. The iterative solution procedure for $M_0(0)$ and \bar{k} continues until either:

- 1) the Mach number at the exit reaches unity and the exit pressure is greater than the sump pressure (choked flow), or
- 2) the exit pressure equals the sump pressure and the exit Mach number is less than unity (unchoked flow).

The pressure, density, and velocity distribution and their derivatives which are determined in the zeroth-order solution, and the entrance-loss relationship determined from test data, are used in defining coefficients of the first-order perturbation equations. These equations define the pressure, density, and axial and circumferential velocity perturbations due to rotor motion. The four physical boundary conditions required for the solution of these equations depend on the perturbation conditions that are specified at the seal entrance and exit. The inlet circumferential velocity perturbation is zero. Expansion of the entrance pressure-loss relationship of equation (8) yields a second boundary condition. A similar expansion of an equation for the density change at the entrance provides another boundary condition. Finally, for choked flow, the first-order perturbation in the exit Mach number is zero,

while for unchoked flow, the first-order perturbation in the exit pressure is zero.

Application of these boundary conditions and numerical integration of the ordinary differential equations provides the first-order solution. Integration of the first-order pressure solution along and around the seal periphery yields the direct and cross-coupled stiffness and damping coefficients, K , k , C , and c , respectively.

The input parameters which can be varied in Nelson's analysis include:

- 1) reservoir pressure and temperature,
- 2) sump pressure,
- 3) seal geometry (i.e. radius, length, clearances),
- 4) rotor rotational speed and precession rate,
- 5) entrance circumferential velocity of the fluid,
- 6) rotor and stator surface roughness,
- 7) empirical entrance-loss relationship,
- 8) fluid viscosity, gas constant, and ratio of specific heats.

An evaluation of Nelson's new model using Moody's equation can be accomplished using the Texas A & M University gas seal test apparatus described by Childs et al. [18]. The apparatus has previously been used in the evaluation of Nelson's Hirs-based model [11, 16], as well as Scharrer's Iwatsubo-based model for labyrinth seals [19]. This report includes an extensive comparison of the predictions of Nelson's new model to test results obtained using the

TAMU apparatus and one example comparing the predictions of Nelson's two analyses.

CHAPTER IV

TEST METHOD AND APPARATUS

Test Method. The test method used in this study for determining the rotordynamic coefficients of seals has been used previously by Iino and Kaneko [20]. An external hydraulic shaker is used to impart translatory harmonic motion to the rotating seal, and rotor motion relative to the stator and the reaction force components acting on the stator are measured.

Fig. 3 shows the manner in which the rotor could be positioned and oscillated in order to identify the dynamic coefficients of the seal for small motion about e_0 . If the added-mass terms are assumed negligible, equation (1) is rewritten

$$-\begin{Bmatrix} F_X \\ F_Y \end{Bmatrix} = \begin{bmatrix} K_{XX}(\epsilon_0) & K_{XY}(\epsilon_0) \\ K_{YX}(\epsilon_0) & K_{YY}(\epsilon_0) \end{bmatrix} \begin{Bmatrix} X \\ Y \end{Bmatrix} + \begin{bmatrix} C_{XX}(\epsilon_0) & C_{XY}(\epsilon_0) \\ C_{YX}(\epsilon_0) & C_{YY}(\epsilon_0) \end{bmatrix} \begin{Bmatrix} \dot{X} \\ \dot{Y} \end{Bmatrix} \quad (10)$$

First, harmonic horizontal motion of the rotor is assumed, where

$$X = e_0 + A \sin(\Omega t) + B \cos(\Omega t)$$

$$\dot{X} = A\Omega \cos(\Omega t) - B\Omega \sin(\Omega t)$$

$$Y = \dot{Y} = 0$$

This yields small motion parallel to the static eccentricity vector, where Ω is the shaking frequency. In a similar fashion, the X and Y-direction force components can be expressed

$$\begin{aligned} F_X &= F_{X0} + F_{XS} \sin(\Omega t) + F_{XC} \cos(\Omega t) \\ F_Y &= F_{Y0} + F_{YS} \sin(\Omega t) + F_{YC} \cos(\Omega t) \end{aligned} \quad (11)$$

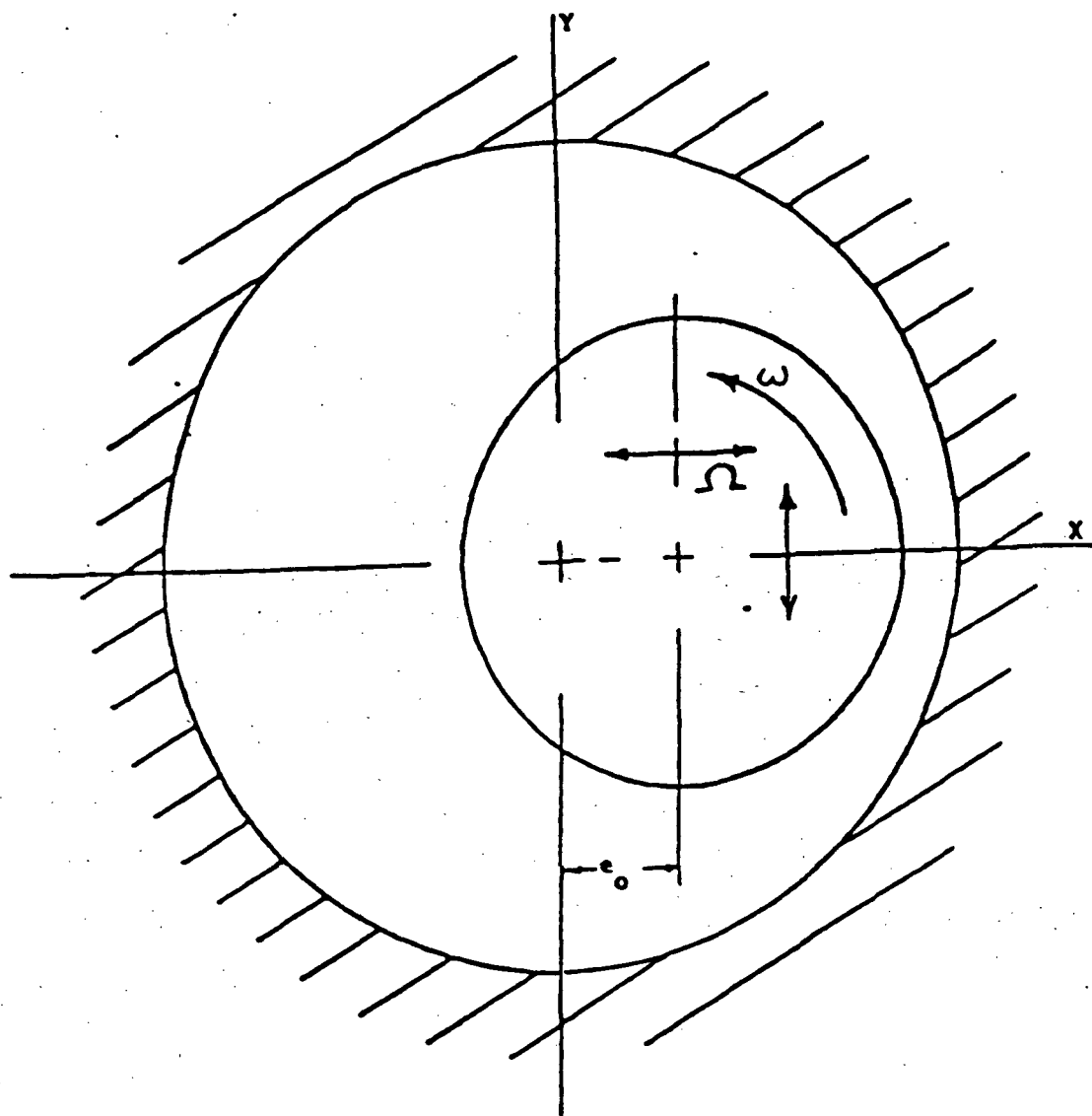


Fig. 3 External shaker method used for coefficient identification.

Substituting these expressions into equation (10) and equating coefficients of constant, sine, and cosine terms yields the following four equations for the dynamic coefficients

$$\begin{aligned}
 -F_{XS} &= K_{XX} A - C_{XX} B \Omega \\
 -F_{XC} &= K_{XX} B + C_{XX} A \Omega \\
 -F_{YS} &= K_{YX} A - C_{YX} B \Omega \\
 -F_{YC} &= K_{YX} B + C_{YX} A \Omega .
 \end{aligned}
 \tag{12}$$

Solving this system of four equations in four unknowns defines the dynamic coefficients as

$$\begin{aligned}
 K_{XX}(\epsilon_0) &= - (F_{XC} B + F_{XS} A) / (A^2 + B^2) \\
 K_{YX}(\epsilon_0) &= - (F_{YS} A + F_{YC} B) / (A^2 + B^2) \\
 C_{XX}(\epsilon_0) &= (F_{XS} B - F_{XC} A) / \Omega(A^2 + B^2) \\
 C_{YX}(\epsilon_0) &= (F_{YS} B - F_{YC} A) / \Omega(A^2 + B^2).
 \end{aligned}
 \tag{13}$$

Therefore, by measuring the reaction forces due to known rotor motion, determining the Fourier coefficients (A , B , F_{XS} , F_{XC} , F_{YS} , F_{YC}), and substituting into the above definitions, the indicated dynamic coefficients can be identified. If the rotor is shaken about a centered position ($e_0 = 0$), then the process is complete. Since the linearized model has skew-symmetric stiffness and damping matrices, all of the coefficients are identified. If, however, the rotor is shaken about an eccentric position, as initially postulated, then it must be shaken vertically about that same point in order to complete the identification process.

Assuming harmonic vertical motion of the rotor, as defined by

$$X = e_0, \dot{X} = 0,$$

$$Y = A \sin(\Omega t) + B \cos(\Omega t),$$

$$\dot{Y} = A\Omega \cos(\Omega t) - B\Omega \sin(\Omega t),$$

yields oscillatory motion that is perpendicular to the assumed static eccentricity vector. A similar process as before results in the coefficient definitions

$$\begin{aligned} K_{YY}(\epsilon_0) &= - (F_{YS} A + F_{YC} B) / (A^2 + B^2) \\ K_{XY}(\epsilon_0) &= - (F_{XS} A + F_{XC} B) / (A^2 + B^2) \\ C_{YY}(\epsilon_0) &= (F_{YS} B - F_{YC} A) / \Omega(A^2 + B^2) \\ C_{XY}(\epsilon_0) &= (F_{XS} B - F_{XC} A) / \Omega(A^2 + B^2) . \end{aligned} \tag{14}$$

All eight dynamic coefficients are thus determined by alternately shaking the rotor at one frequency Ω in directions which are parallel and perpendicular to the static eccentricity vector.

Test Apparatus. The test apparatus used for this study was the Texas A & M University gas seal apparatus described by Childs et al. [18] modified for rotor speeds up to 16,000 cpm. Fig. 4 shows the assembled rig. The test apparatus allows the following seal parameters to be controlled independently, providing insight into the influence these parameters have on seal behavior:

- 1) static position and dynamic motion of the rotor,
- 2) pressure ratio across the seal,
- 3) prerotation of the incoming fluid (air),
- 4) seal configuration, and
- 5) rotor rotational speed.

Previously, the maximum possible test speed was 8500 cpm. High

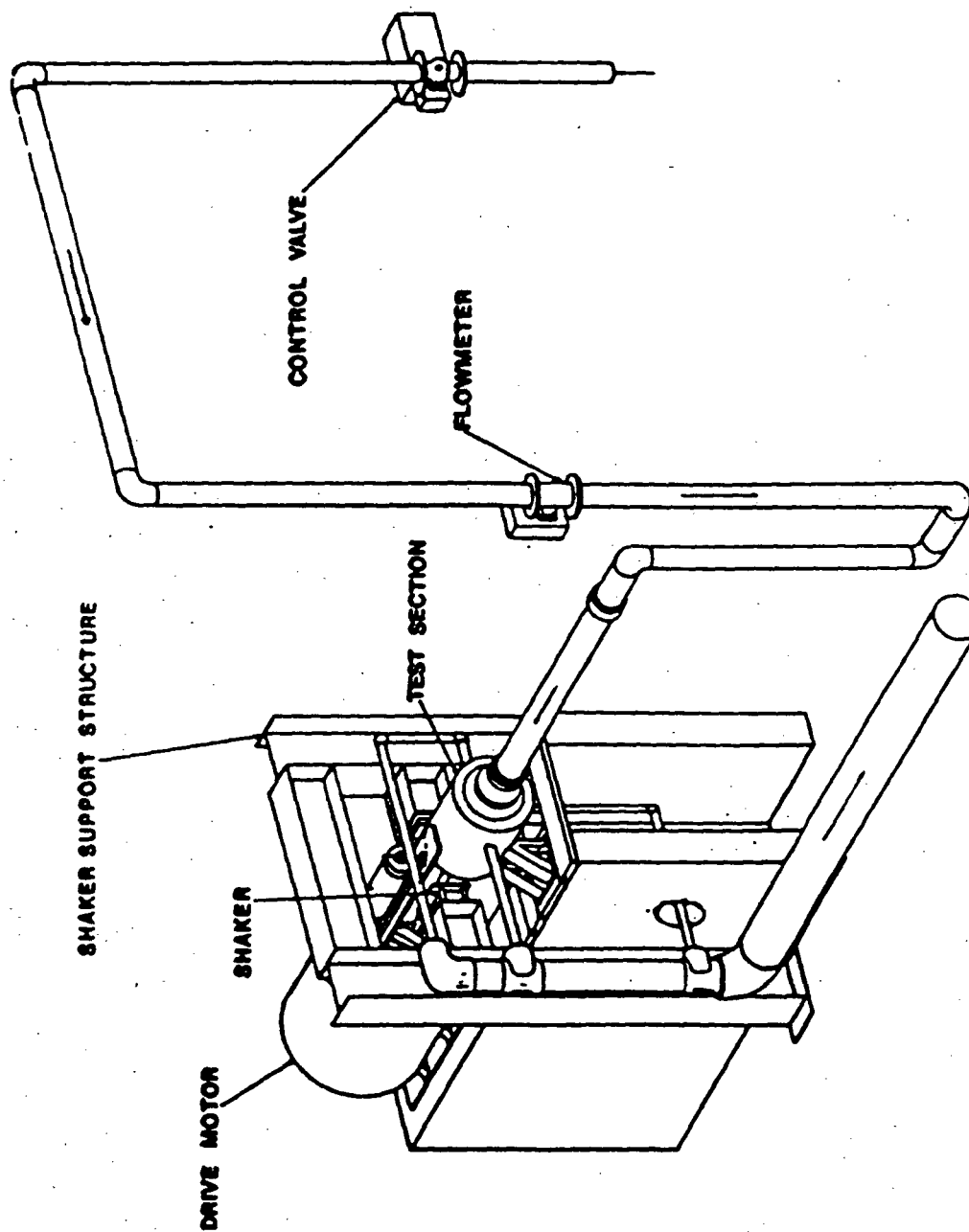


Fig. 4 Test apparatus assembly

bearing temperatures and the reduction of interference in the rotor-shaft fitment with increasing speed had served to limit shaft speed. These problems have been addressed by some specific design modifications which are discussed below.

In the past, the seal rotor was press-fitted and secured axially by a bolt circle to the rotor shaft. As the running speed is increased, however, the inertia-induced diametrical growth of the rotor exceeds the growth of the shaft. By increasing the interference in the stationary rotor-shaft fit, a greater allowance for this growth difference has been provided. Fig. 5 shows the present rotor-shaft design, a tapered rotor which is hydraulically expanded during installation. The rotor is inserted over the end of the tapered shaft and a large nut is used to pull the rotor onto the shaft. Fluid is pumped between the shaft and rotor, causing the rotor to expand. This separating force allows the rotor to be pulled onto the shaft until the desired interference fit is achieved.

The problem of high bearing temperatures has been eliminated by replacing a roller-type thrust bearing and modifying the lubricant flow. A Torrington Hydraflex thrust bearing, consisting of eight one-inch rubber-faced pads which are water lubricated, is now in place at the rear of the rotor. In addition, the lubricant for the Torrington hollow-roller bearings which support the shaft has been changed to light turbine oil with a maximum temperature of 270°F. The hollow-roller-bearing caps have been modified to direct the oil flow to the regions of heat buildup. These modifications are shown

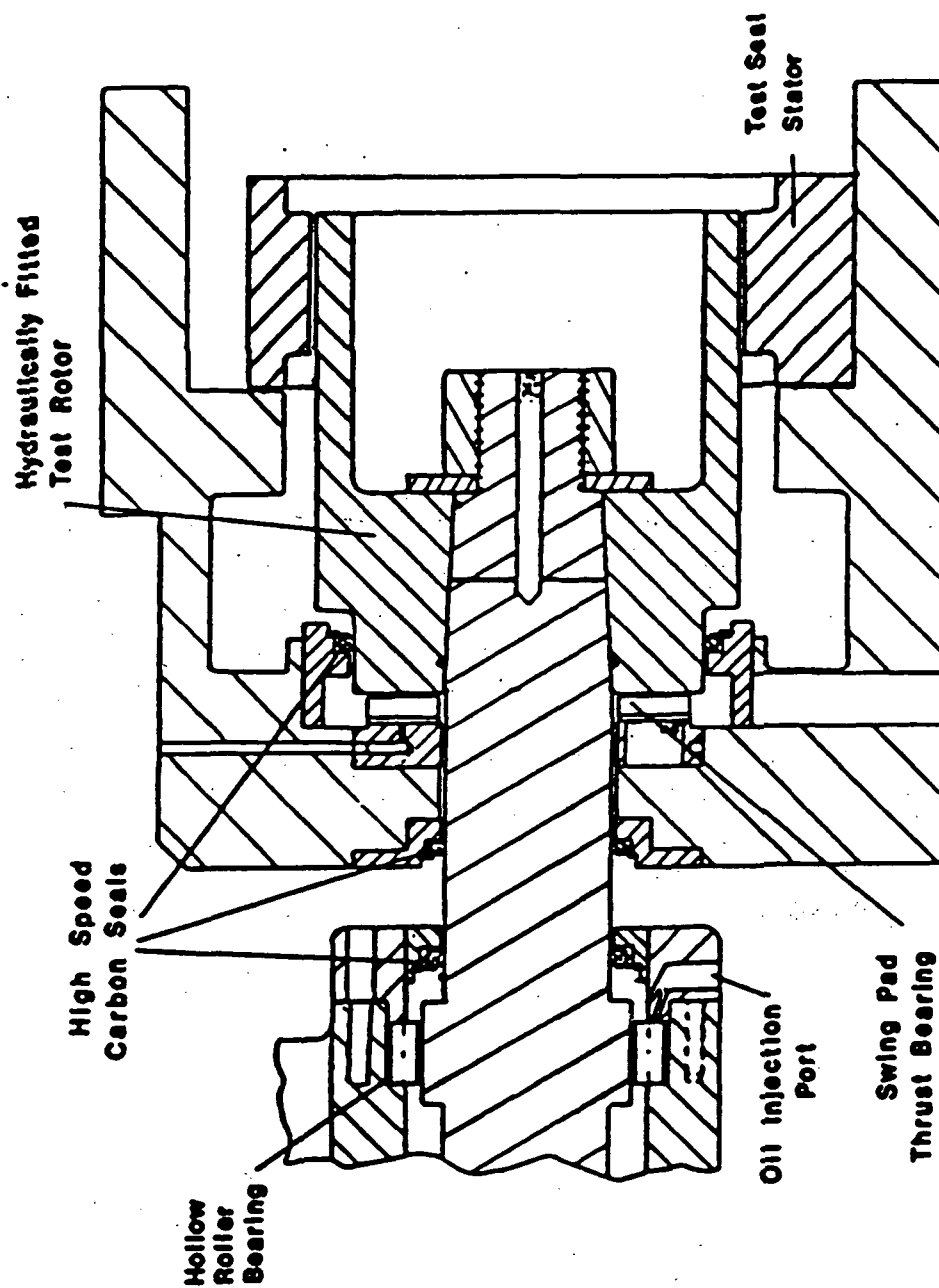


Fig. 5 Cross-sectional view of test section showing rotor-shaft assembly.

in Fig. 5.

The final modification to allow operation of the TAMU gas seal test apparatus at high speeds was the installation of Koppers circumferential seals for the hollow-roller and thrust bearing lubrication systems. At 16,000 rpm, the surface speeds of the shaft and rotor (170 and 350 ft/sec, respectively) exceed the limits of lip seals, which had been used on the TAMU apparatus. The Koppers seals in Fig. 5 were designed for gas applications. The sealing mechanism is a segmented carbon seal ring.

CHAPTER V

TEST RESULTS: INTRODUCTION

The results reported here are from tests of four smooth-rotor/smooth-stator seals with different ratios of inlet-to-exit clearance (i.e. different tapers): 1.0, 1.5, 2.0, and 2.5. For the remainder of this report, the seals will be referred to as seal 1.0, seal 1.5, seal 2.0, and seal 2.5. Fig. 6 shows a tapered stator. Tables 1 - 3 contain the dimensions and pertinent data for each seal tested.

The test program had the following objectives:

- 1) Acquire leakage, stiffness, and damping coefficients as a function of rotor speed, pressure drop, and inlet circumferential velocity for four smooth-rotor/smooth-stator seals with different tapers but equal exit clearances.
- 2) Compare the effect of varying the seal taper angle on the experimentally determined rotordynamic coefficients.
- 3) Compare test results to the predictions of Nelson's analysis which uses Moody's equation for a friction factor.

When shaking about the centered position, the test apparatus can be used to control the rotor speed, reservoir pressure (i.e. supply pressure), circumferential velocity of the inlet air, and the frequency and amplitude of translatory rotor motion. Two shake frequencies, 58.8 and 74.6 Hz, were used during testing with essentially the same results. The results plotted here were obtained

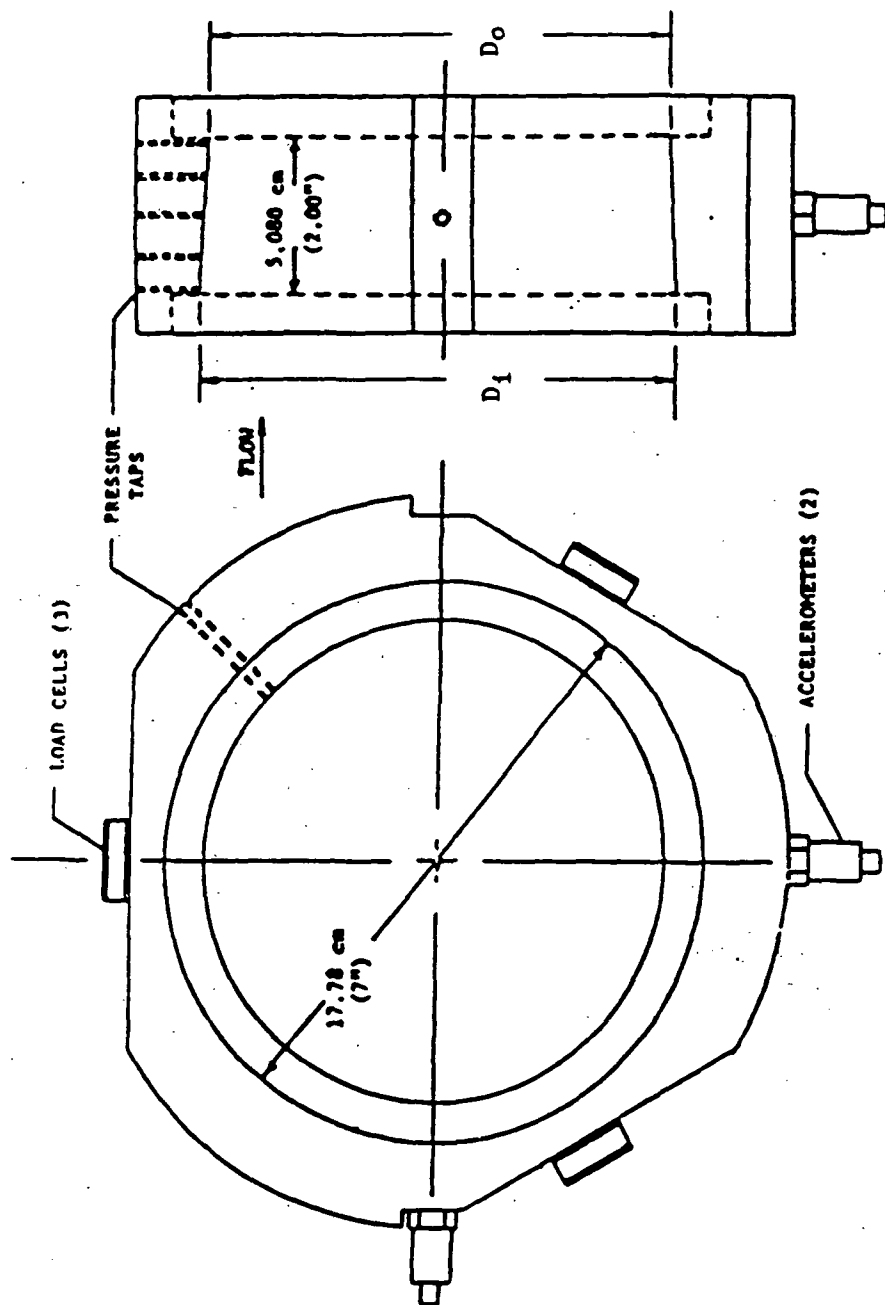


Fig. 6 Detail of tapered stator.

Table 1. Test stator specifications.

Stators

Seal:	1.0	1.5
Diameter:		
upstream	15.22 cm (5.991 in)	15.26 cm (6.008 in)
downstream	15.22 cm (5.991 in)	15.22 cm (5.992 in)
Material:	brass	brass
Surface roughness:	0.406 μm (16 μin)	0.660 μm (26 μin)
Seal:	2.0	2.5
Diameter:		
upstream	15.29 cm (6.020 in)	15.34 cm (6.040 in)
downstream	15.22 cm (5.990 in)	15.22 cm (5.992 in)
Material:	brass	brass
Surface roughness:	0.381 μm (15 μin)	0.559 μm (22 μin)

Table 2. Test rotor specifications.

Seal:	1.0, 1.5, 2.0, 2.5
Diameter:	
upstream	15.14 cm (5.959 in)
downstream	15.14 cm (5.959 in)
Material:	304 stainless steel
Surface roughness:	0.279 μm (11 μin)

Table 3. Test seal specifications.

<u>Seal</u>	<u>Seal length</u>	<u>Radial clearance</u>	<u>H_1/H_0</u>
1.0	5.080 cm (2.000 in)	$H_1 = 0.406 \text{ mm (0.016 in)}$ $H_0 = 0.406 \text{ mm (0.016 in)}$	1.0
1.5	5.080 cm (2.000 in)	$H_1 = 0.622 \text{ mm (0.0245 in)}$ $H_0 = 0.419 \text{ mm (0.0165 in)}$	1.48
2.0	5.080 cm (2.000 in)	$H_1 = 0.775 \text{ mm (0.0305 in)}$ $H_0 = 0.394 \text{ mm (0.0155 in)}$	1.97
2.5	5.080 cm (2.000 in)	$H_1 = 1.030 \text{ mm (0.0405 in)}$ $H_0 = 0.419 \text{ mm (0.0165 in)}$	2.45

Table 4. Definition of symbols used in figures.

<u>Pressures</u>	<u>Rotor speeds*</u>	<u>Inlet circumferential velocities</u>
1 - 3.08 bar	1 - 3000 cpm	1 - High velocity against rotation
2 - 4.46 bar	2 - 6000 cpm	2 - Low velocity against rotation
3 - 5.84 bar	3 - 9500 cpm	3 - Zero circumferential velocity
4 - 7.22 bar	4 - 13000 cpm	4 - Low velocity with rotation
5 - 8.25 bar	5 - 16000 cpm	5 - High velocity with rotation

The pressure for each test is set at the flowmeter of Fig. 7.

* For high inlet circumferential air velocity against rotation, seal 1.5 was tested at the following rotor speeds: 3000, 6000, 8000, 10000, 12000, 14000, and 16000 cpm.

by shaking at 74.6 Hz at an amplitude between 4 and 5 mils. The actual test points for each of the other three independent variables are shown in Table 4.

Fig. 7 - 10 show the inlet circumferential velocity values (U_θ) for the configurations described in Table 4 for the seals reported on here. The equation for U_θ is

$$U_\theta = \dot{m} \sin \phi / \rho A_v$$

where \dot{m} is the fluid mass flow rate, ρ is the fluid density, A_v is the exit area of the fluid turning vanes, and ϕ is the fluid swirl angle at the turning vanes exit measured from the axial direction. Negative circumferential velocities represent velocities opposed to the direction of rotor rotation. Positive velocities are in the direction of rotor rotation. Note that curve 3 (representing zero inlet circumferential velocity) lies on the horizontal axis in each figure. The inlet circumferential velocity ratio, the ratio of inlet circumferential velocity to rotor surface velocity, ranged from about -6 to about 8. When reviewing the following figures, Table 4 and Fig. 7 - 10 should be consulted for the definitions of symbols used.

Normalized Parameters. Before the tests described herein were performed, the TAMU gas seal test apparatus was modified as described in the TEST METHOD AND APPARATUS chapter to allow operation at running speeds up to 16,000 cpm. As expected, subsequent tests revealed a dependence of the rotor diameter on running speed due to inertia and thermal effects. The rotor growth data are shown in Table 5. Thus, as the rotor turns faster, the forces in the seal are

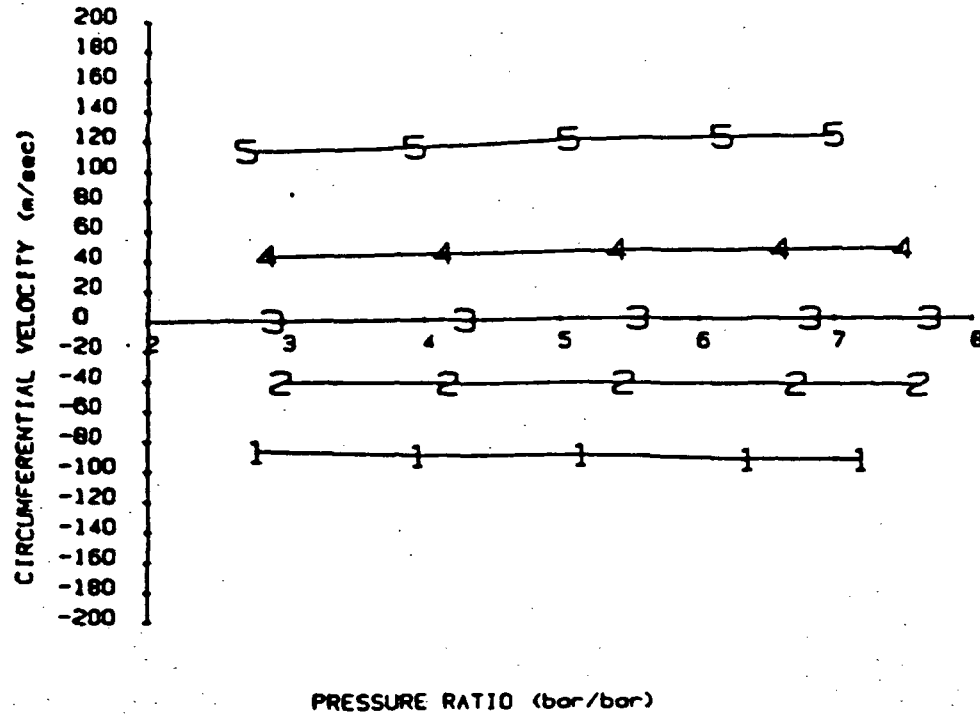


Fig. 7 Inlet circumferential velocity vs. pressure ratio for straight bore seal (seal 1.0)

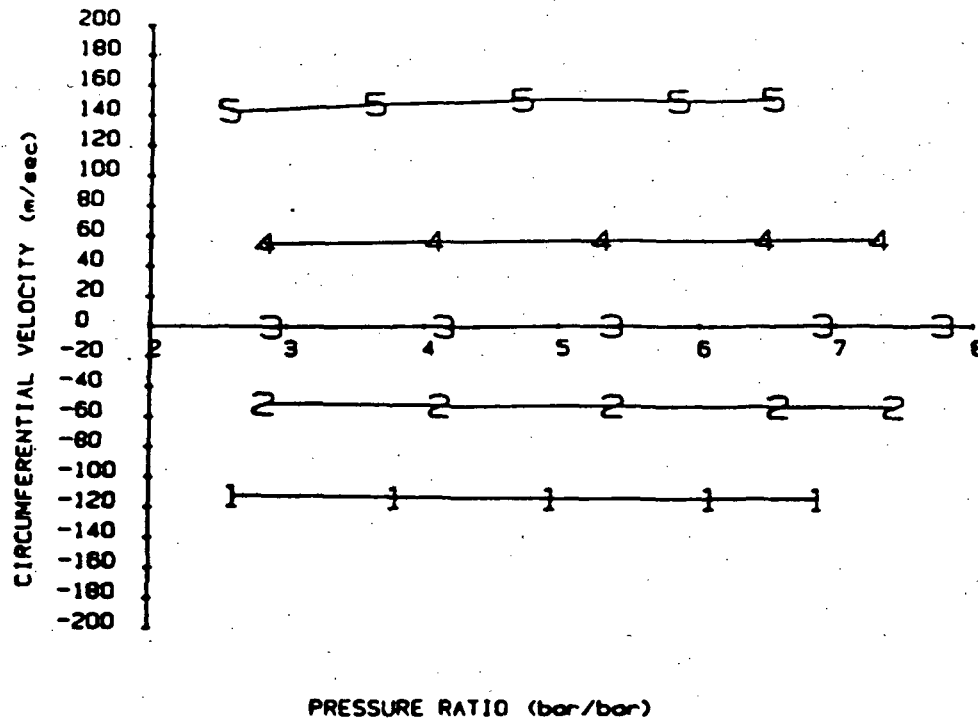


Fig. 8 Inlet circumferential velocity vs. pressure ratio for 1.5 taper seal.

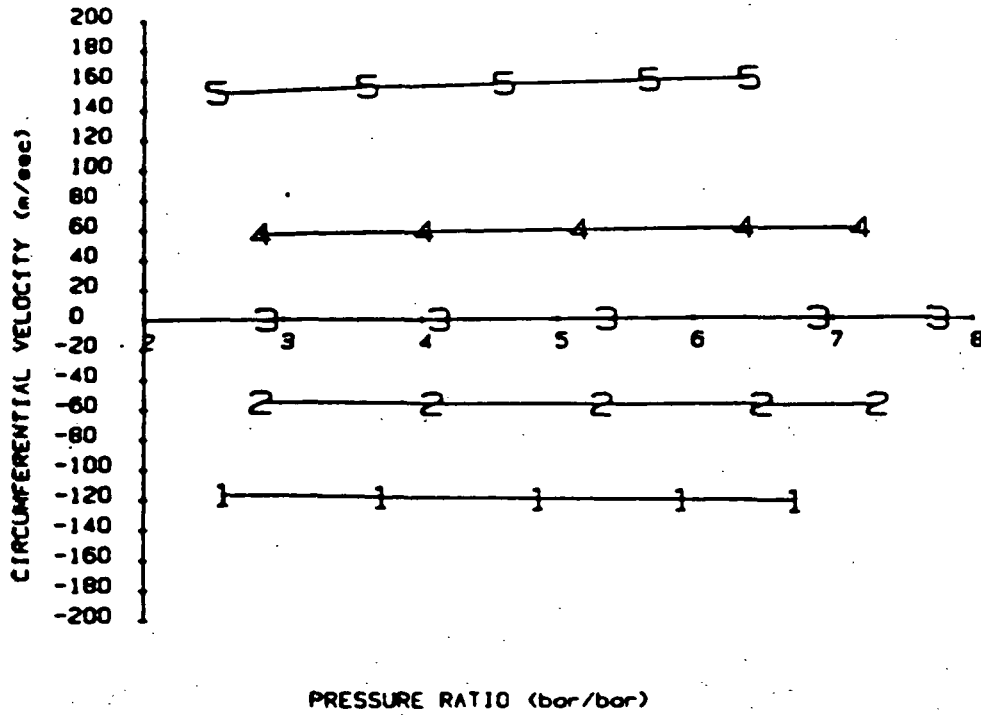


Fig. 9 Inlet circumferential velocity vs. pressure ratio for 2.0 taper seal.

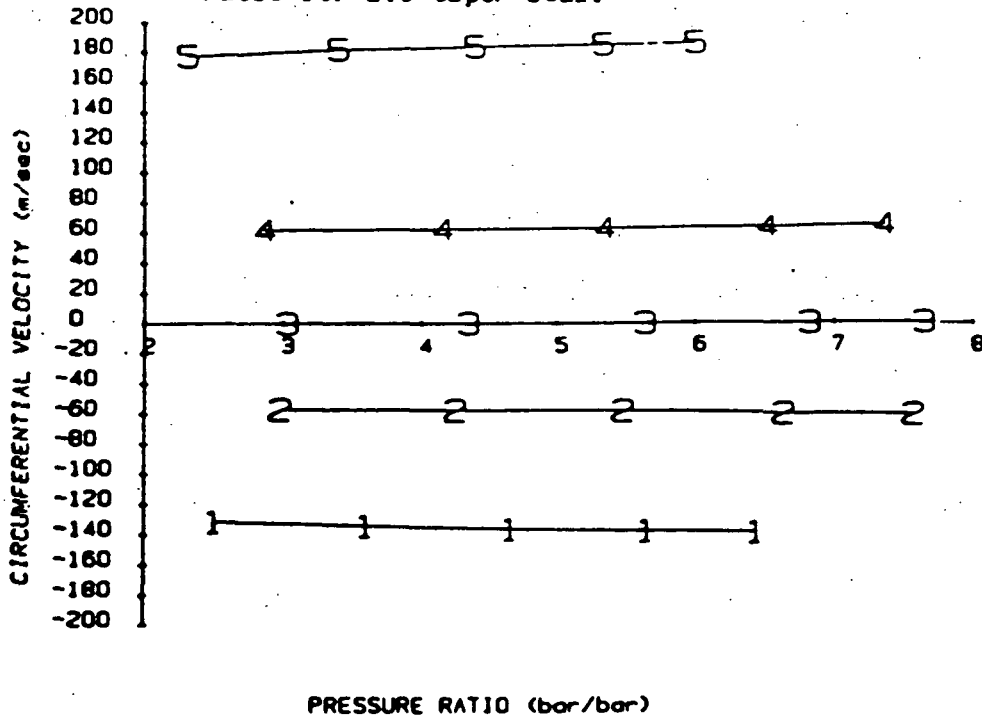


Fig. 10 Inlet circumferential velocity vs. pressure ratio for 2.5 taper seal.

Table 5. Growth of rotor with rotational speed.

Rotor speed (rpm)	Diametrical growth	
	(mm)	(inches x 1000)
3000	0.01	0.4
6000	0.02	0.7
9500	0.03	1.2
13000	0.05	1.9
16000	0.11	4.4

Table 6. Normalized coefficients.

$$\bar{K} = K \frac{H_0}{DL(\Delta P)} \quad (\text{nondim})$$

$$\bar{C} = C \frac{H_0}{DL(\Delta P)} \quad (\text{sec})$$

K = stiffness (N/mm)

C = damping (N sec/mm)

 H_0 = seal exit clearance (mm)

D = seal diameter (m)

L = seal length (m)

 ΔP = pressure drop across seal (N/m²)

affected not only by the increased surface speed of the rotor (drag) but also by a change in clearance (friction factor). The rotordynamic coefficients presented in this study have been normalized. See Table 6 for the definitions of the normalized parameters. Note that the effect on the physical rotordynamic coefficients of increasing the running speed is generally greater than on the normalized coefficients. Fig. 11 shows the dependence on running speed of the direct stiffness of the 1.0 taper seal before and after normalization. Note the smaller percentage increase of the dimensionless stiffness as the speed increases.

Relative uncertainty. Before the test results are given, a statement about the experimental uncertainty is needed. The method used is that described by Holman [21] for estimating the uncertainty in a calculated result based on the uncertainties in primary measurements. The uncertainty w_R in a result R which is a function of n primary measurements $x_1, x_2, x_3, \dots, x_n$ with uncertainties $w_1, w_2, w_3, \dots, w_n$ is

$$w_R = \left\{ \left(\frac{\partial R}{\partial x_1} w_1 \right)^2 + \left(\frac{\partial R}{\partial x_2} w_2 \right)^2 + \dots + \left(\frac{\partial R}{\partial x_n} w_n \right)^2 \right\}^{1/2} \quad (15)$$

In this case, the rotordynamic coefficients are calculated using equation (13). The primary measurements are forces, displacements, and frequency. The uncertainty in these measurements on the TAMU test apparatus are 0.89 N (0.2 lb), 0.0013 mm (0.05 mils), and 0.13 Hz, respectively. For the four seals tested, the estimated uncertainty in the four rotordynamic coefficients as a percentage of the coefficient values was generally less than 5% for the direct and

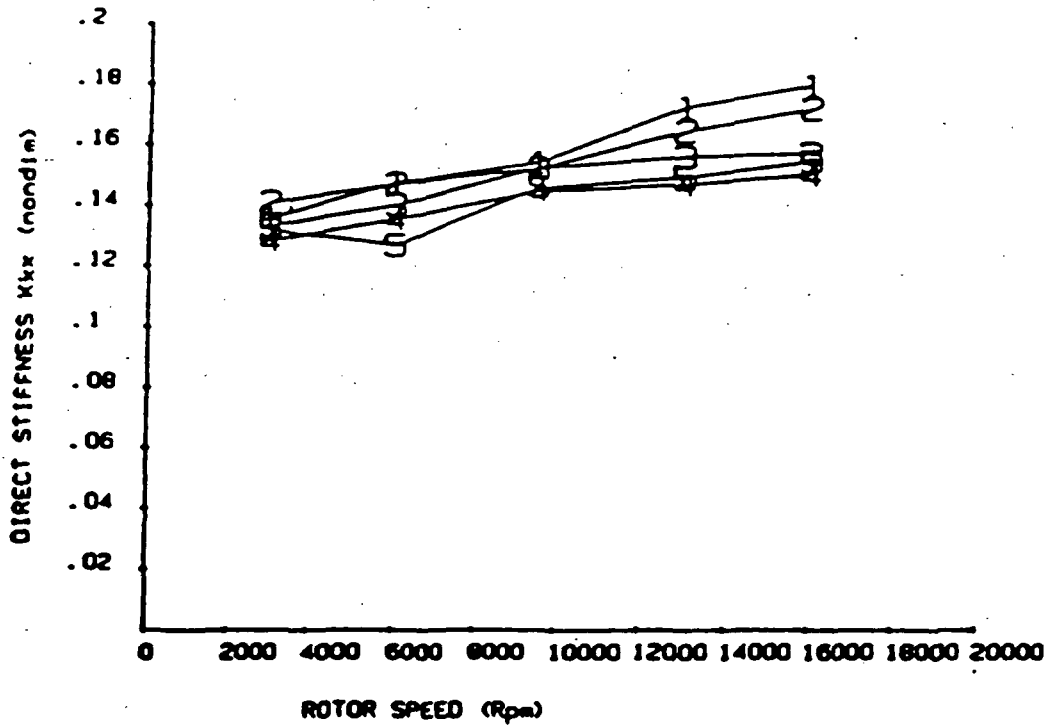
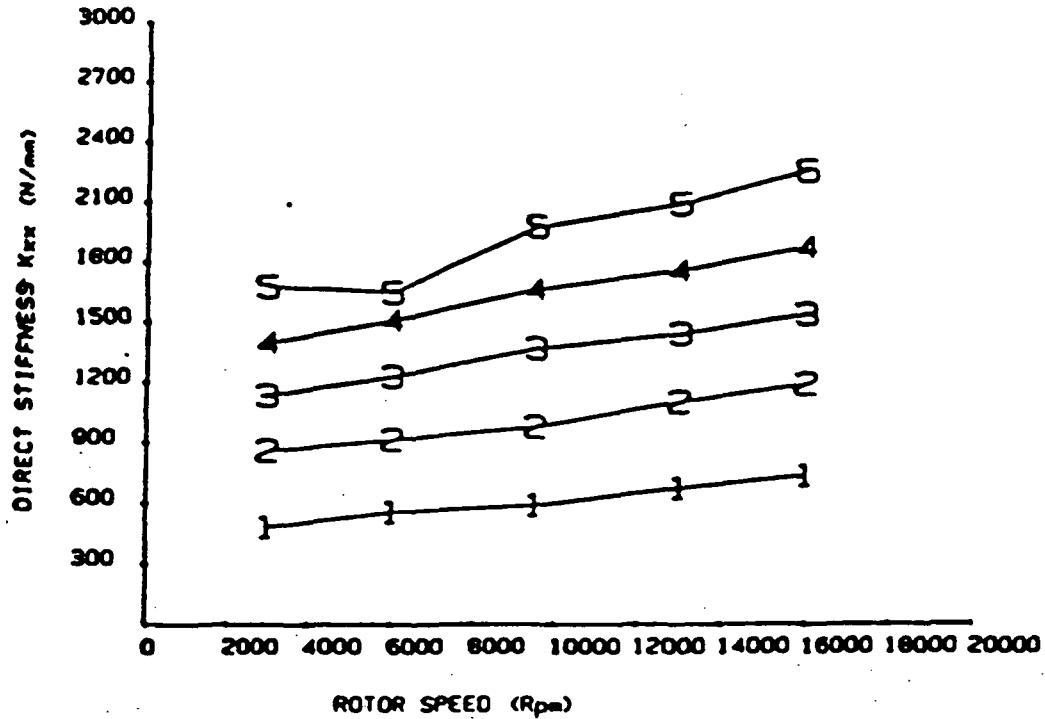


Fig. 11 Running speed dependence of direct stiffness of seal 1.0 at different pressure ratios before (above) and after (below) normalization (low inlet circumferential velocity in the direction of rotor rotation). See Table 4 and Fig. 7 for definitions of symbols.

cross-coupled stiffnesses, from 10 to 20% for the direct damping, and from 40% to several times the value of the cross-coupled damping. Since the uncertainties in the cross-coupled damping values were so high, and since the cross-coupled-damping forces are of minor significance compared to the other damping and stiffness forces, comparisons of the cross-coupled-damping coefficients have been omitted from this report.

Selection of report data. For each of the four seals tested, there were 125 test points for leakage, direct and cross-coupled stiffness, and direct damping at the 74.6 Hz shake frequency. Generally, a ranking of the three independent variables of the test apparatus in order of the relative effect on the normalized rotordynamic coefficients of a seal is: inlet circumferential velocity, pressure ratio, running speed. Figures in the next two chapters show the dependence of leakage and normalized rotordynamic coefficients on seal taper for inlet swirl conditions of Table 4. Fig. A1 - A16 in the Appendix show leakage and normalized coefficients at 3000 and 16000 rpm as a function of inlet circumferential velocity at the five applied pressure ratios. Generally, solid lines in a figure represent experimental results, and broken lines represent the predictions of Nelson's analysis. These figures will be used in a comparison of the effect of taper on seal performance, and in an evaluation of Nelson's analysis.

CHAPTER VI

TEST RESULTS: RELATIVE PERFORMANCE OF SEALS

This evaluation of the effect on seal performance of varying the seal taper angle requires frequent use of the information in Table 4 and Fig. 7 - 10. Comparisons of the leakage, direct stiffness, cross-coupled stiffness, direct damping, and stability of the four seals follow.

Leakage. The flow rate of air through each seal was measured with either a vortex flowmeter or a turbine flowmeter located in the piping upstream of the test section (see Fig. 4). The specifications on the two meters state ranges of 37 to 534 and 3 to 60 acfm, respectively. Unfortunately, the minimum capability of the vortex meter was understated and some erroneous data were recorded, predominantly for seal 2.5. Leakage data which were clearly in error (e.g. negative leakage) have been eliminated from the figures referred to below.

A comparison of the leakage of the four seals reveals, as expected, that for equal exit clearances, greater leakage occurs for greater inlet clearances. Data from tests at 3000 and 16000 rpm are shown in Fig. 12 and 13 and in Fig. A1 - A4 in the Appendix. Generally, the leakage of seals 1.5, 2.0, and 2.5 exceeded that of seal 1.0 by from 15 to 25%, 25 to 40%, and 45 to 60%, respectively.

Direct stiffness. An interesting comparison of the dimensionless

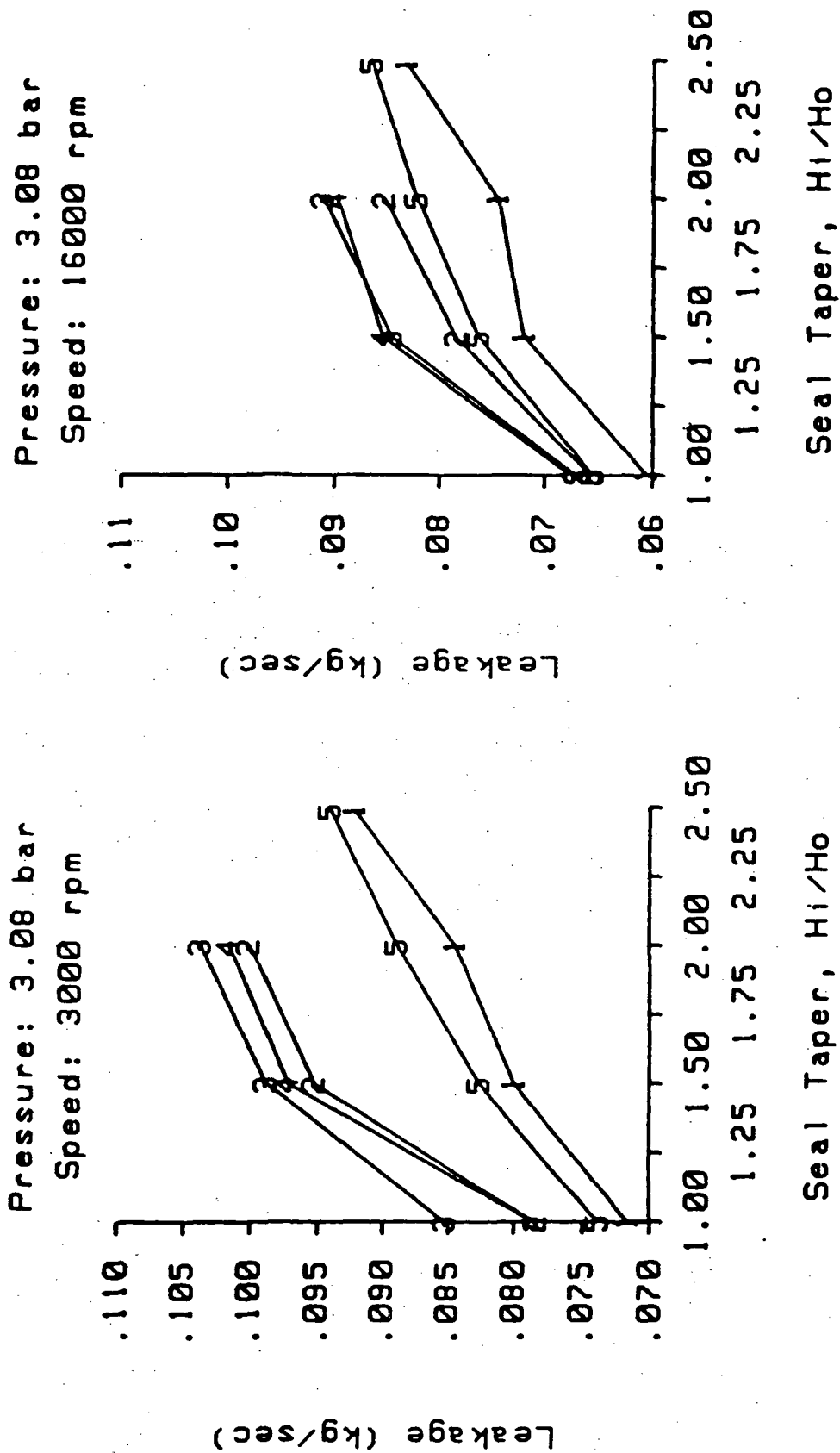


Fig. 12 Experimental mass flow rates through the test seals at 3.08 bar pressure.
See Table 4 for definitions of inlet circumferential velocity symbols.

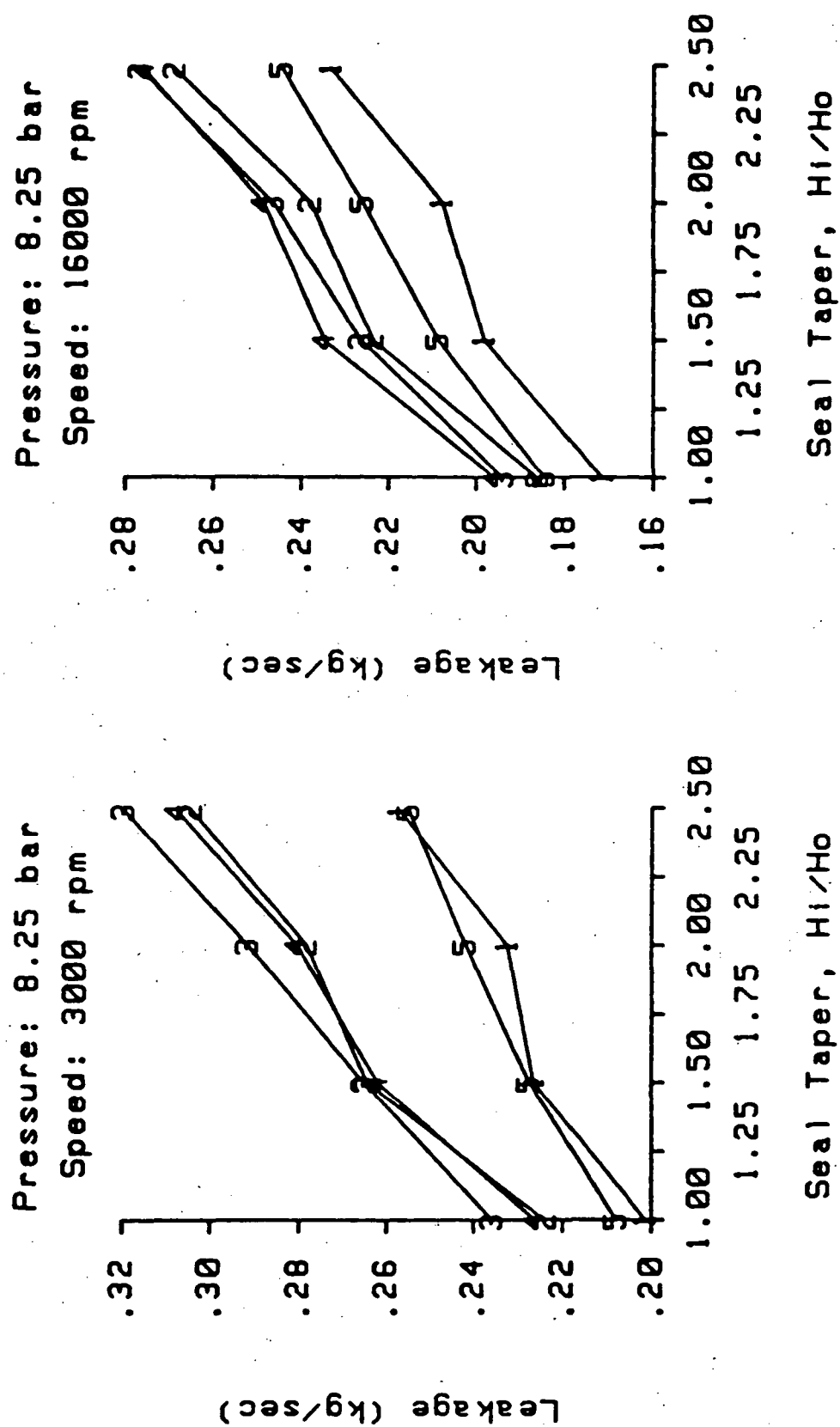


Fig. 13 Experimental mass flow rates through the test seals at 8.25 bar pressure.
See Table 4 for definitions of inlet circumferential velocity symbols.

direct stiffness of the four seals may be developed from Fig. 14 and 15 and Fig. A5 - A8 in the Appendix. The experimental stiffness values of seals 1.5 and 2.0 are close throughout the range of inlet circumferential velocities. Seal 2.0 appears stiffer at low pressure ratios, while seal 1.5 appears stiffer at higher pressure ratios. The stiffness of seal 2.5 is clearly less than that of both seals 1.5 and 2.0 throughout the range of velocities. Seal 2.5 is about 10 to 40% less stiff than seal 2.0. At a running speed of 3000 rpm, seals 1.5 and 2.0 are substantially stiffer than seal 1.0 for all circumferential velocities. The margin of difference decreases from two or three times stiffer to about 20% stiffer as the circumferential velocity increases from negative (opposing rotor rotation) to positive. However, at 16000 rpm, seals 1.5 and 2.0 are less than 5% stiffer than seal 1.0 for high pressure, high-circumferential-velocity tests. For zero and negative circumferential velocities, seals 1.5 and 2.0 are two to three times stiffer than seal 1.0 at 16000 rpm.

Cross-coupled stiffness. Fig. 16, 17, and A9 - A12 in the Appendix reveal that seal 1.0 had the greatest and seal 2.5 the lowest cross-coupled stiffness magnitudes throughout the range of inlet circumferential velocities tested at both 3000 and 16000 rpm running speeds. There was little difference in the cross-coupled stiffness of seals 1.5 and 2.0 throughout the tests. Furthermore, the cross-coupled stiffnesses at zero inlet circumferential velocity were positive for seals 1.0 and 2.0 and negative for seals 1.5 and 2.5.

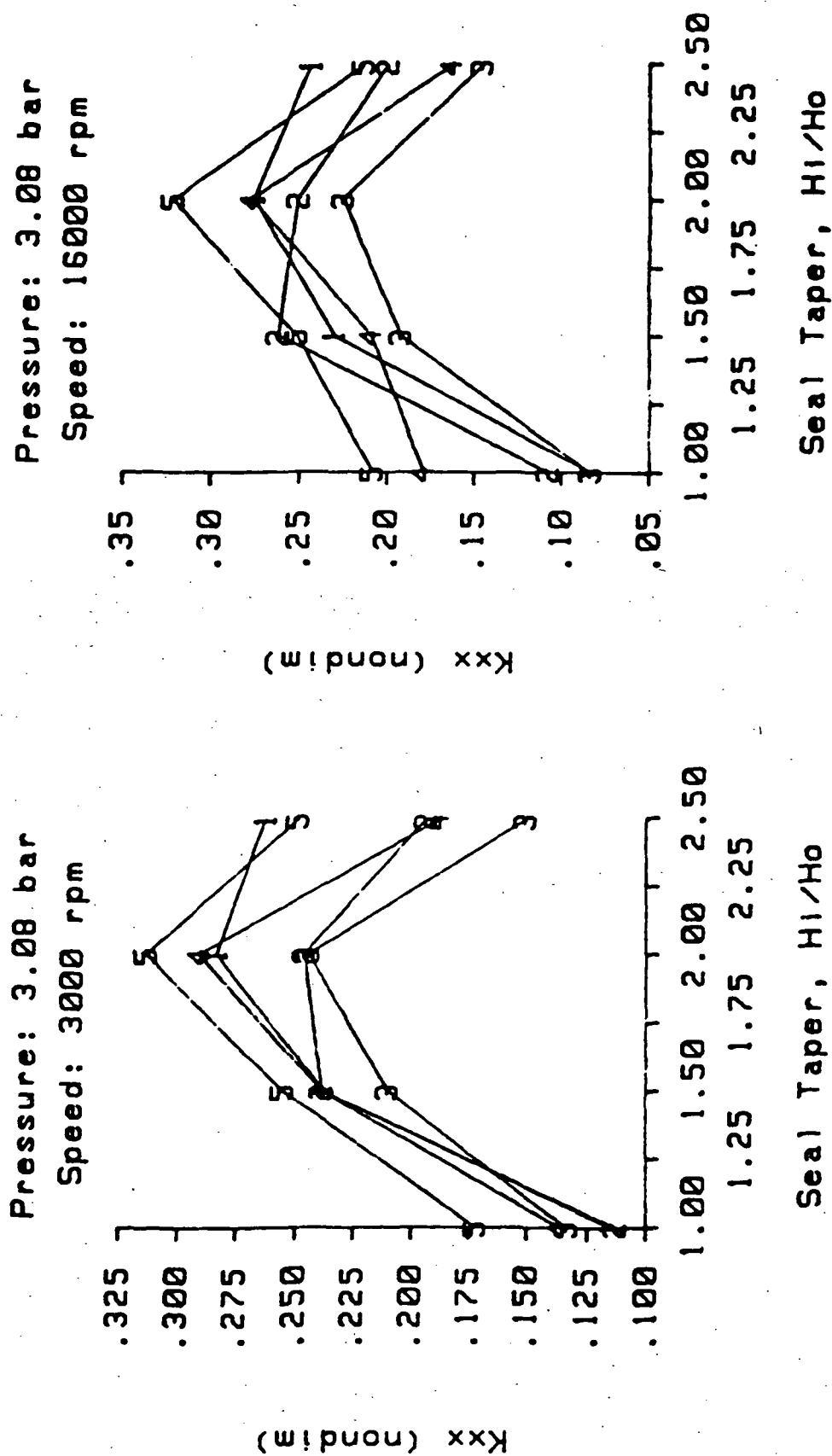


Fig. 14 Experimental normalized direct stiffnesses of the test seals at 3.08 bar pressure. See Table 4 for definitions of inlet circumferential velocity symbols.

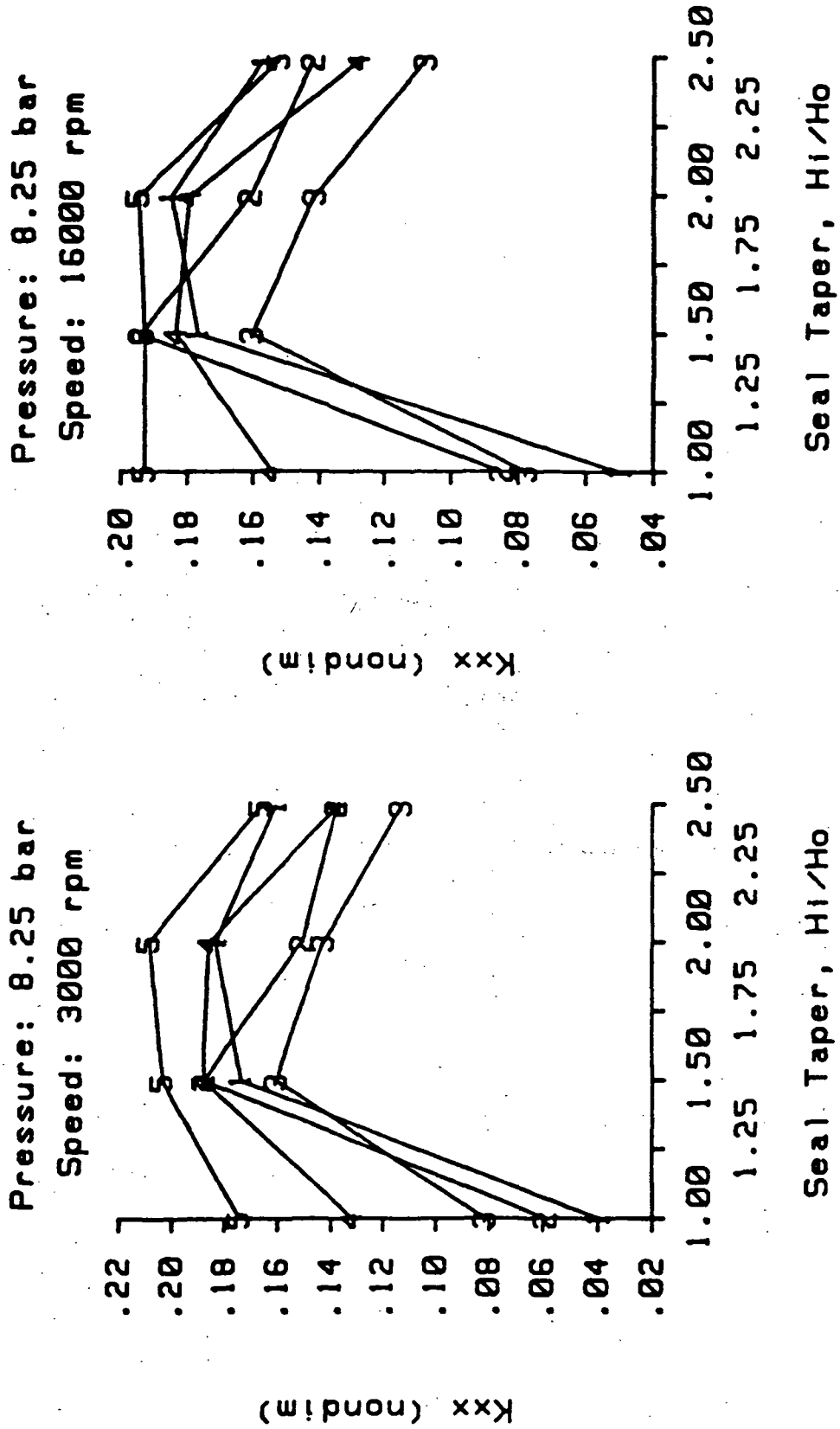


Fig. 15 Experimental normalized direct stiffnesses of the test seals at 8.25 bar pressure.
See Table 4 for definitions of inlet circumferential velocity symbols.

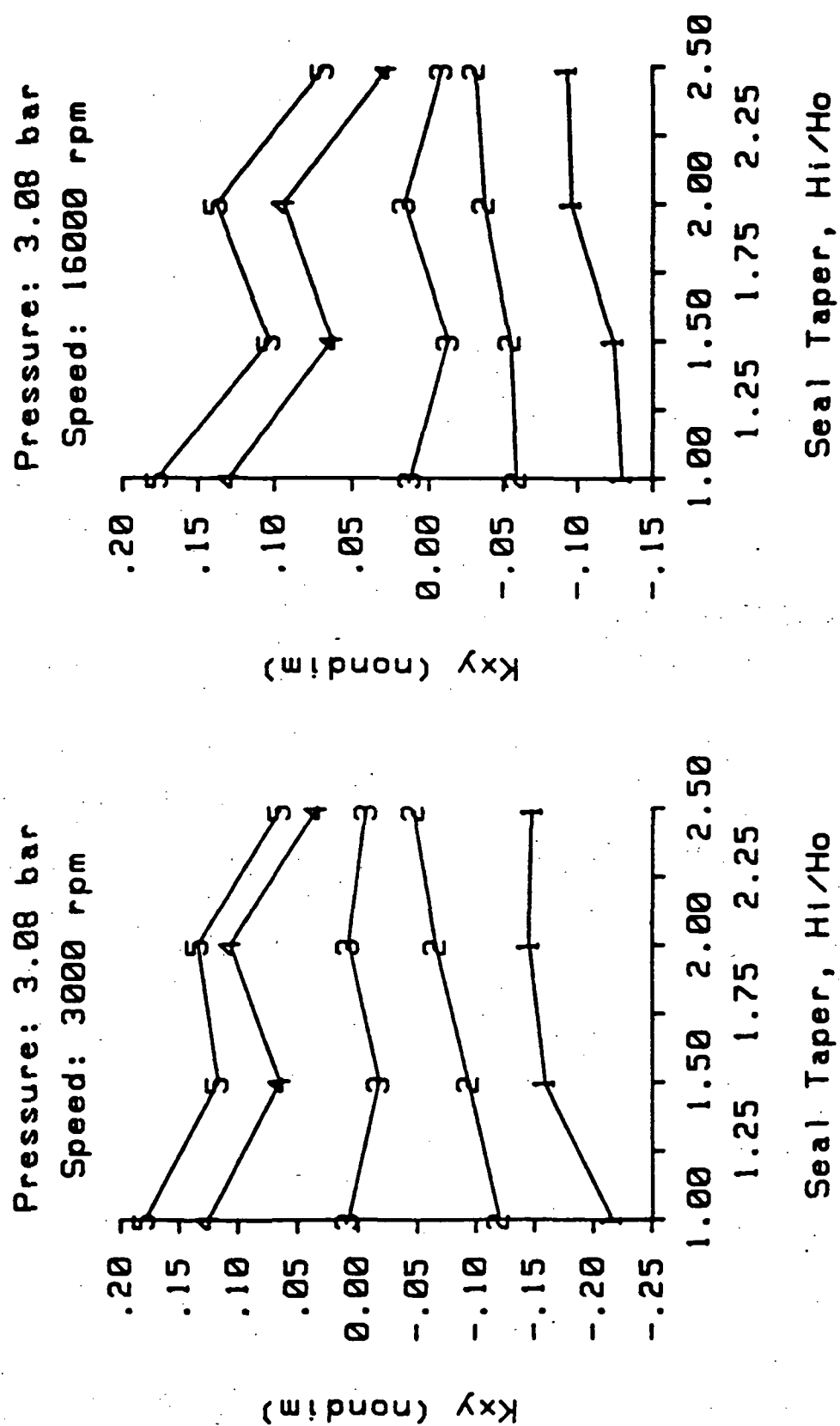
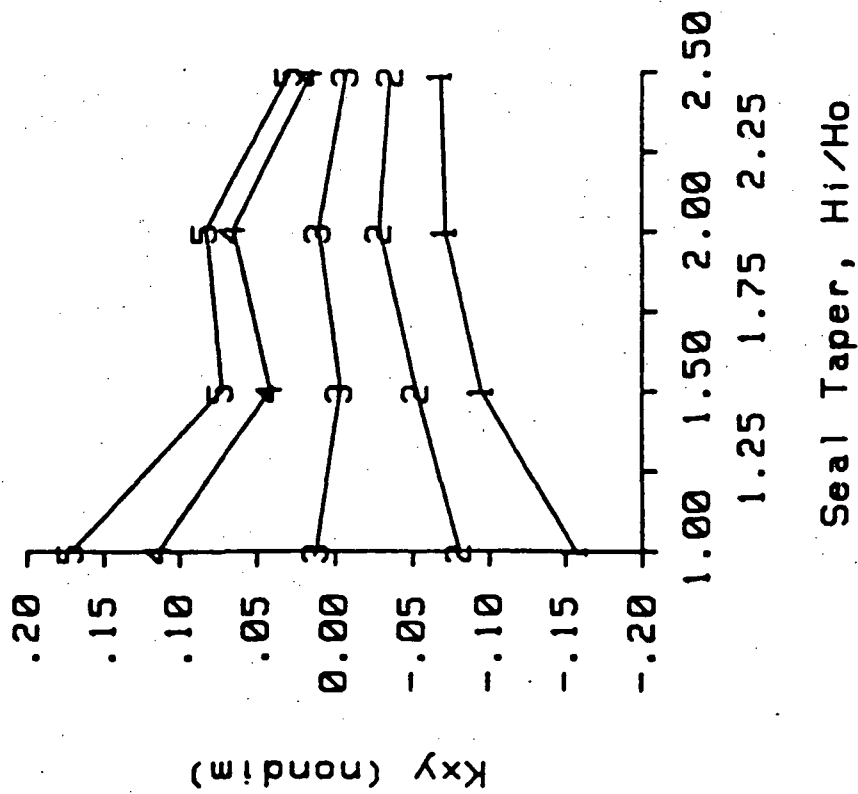


Fig. 16 Experimental normalized cross-coupled stiffnesses of the test seals at 3.08 bar pressure. See Table 4 for definitions of inlet circumferential velocity symbols.

Pressure: 8.25 bar
Speed: 3000 rpm



Pressure: 8.25 bar
Speed: 16000 rpm

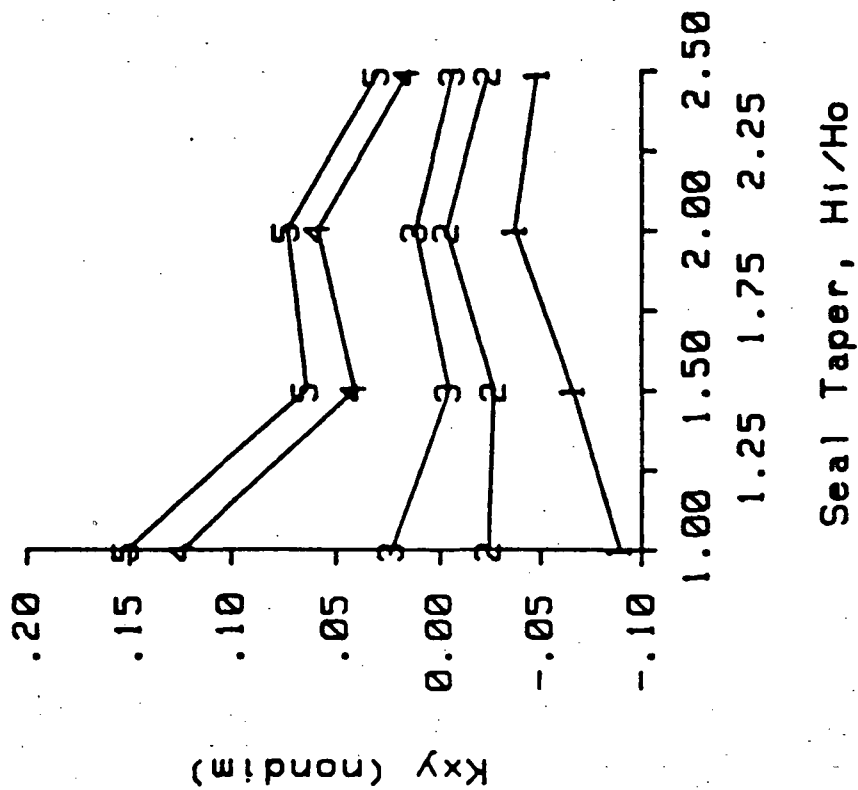


Fig. 17 Experimental normalized cross-coupled stiffnesses of the test seals at 8.25 bar pressure. See Table 4 for definitions of inlet circumferential velocity symbols.

This data will be discussed further in a stability analysis following the comparison of experimental data.

Direct damping. Fig. 18, 19, and A13 - A16 in the Appendix show a general decrease in the direct damping as the taper (ratio of inlet to exit clearance) increases for seals of equal exit clearance. The clearest downward shift occurs as the taper is increased from 1.0 to 1.5, while seals 1.5 and 2.0 again appear only marginally different. Noting that the difference between the damping of seals 1.0 and 1.5 is significantly less at 16000 rpm, high positive inlet circumferential velocity, and high pressures, remember that the estimated uncertainty in the experimental damping values was generally from 10 to 20% (see the section on relative uncertainty).

Stability analysis. One further parameter of comparison among the test seals is the dimensionless whirl frequency ratio. To understand the value of this parameter, consider a rotor in a circular orbit of amplitude A and frequency Ω (Fig. 20). The X and Y components of force in the seal model of equation (3) may be resolved into radial and tangential forces

$$F_r = F_x \cos \omega t + F_y \sin \omega t$$

$$F_t = -F_x \sin \omega t + F_y \cos \omega t$$

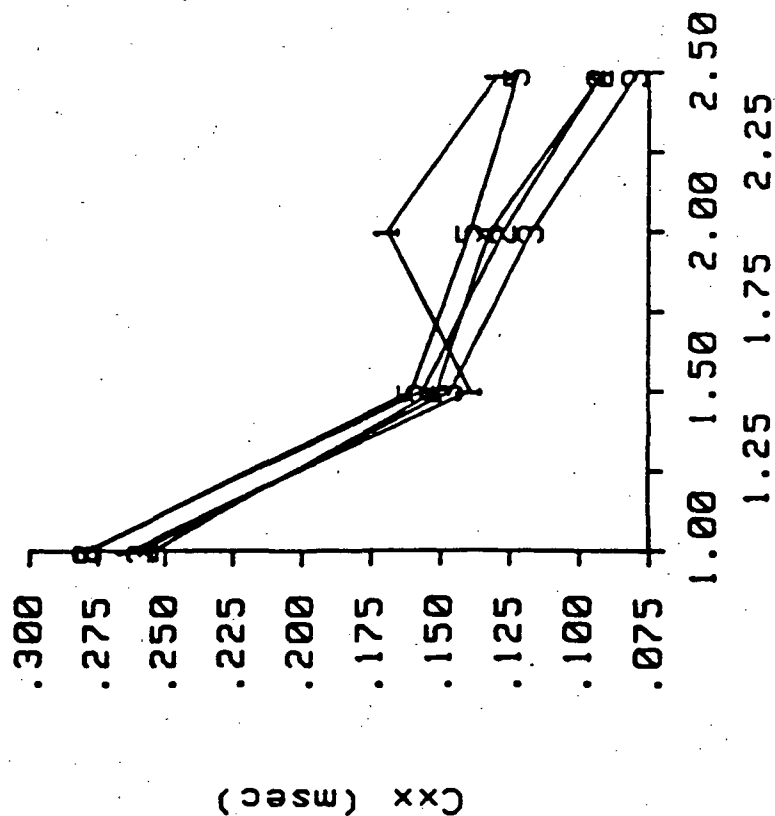
Expressing the rotor motion as

$$X = A \cos \omega t \quad \dot{X} = -A\omega \sin \omega t$$

$$Y = A \sin \omega t \quad \dot{Y} = A\omega \cos \omega t$$

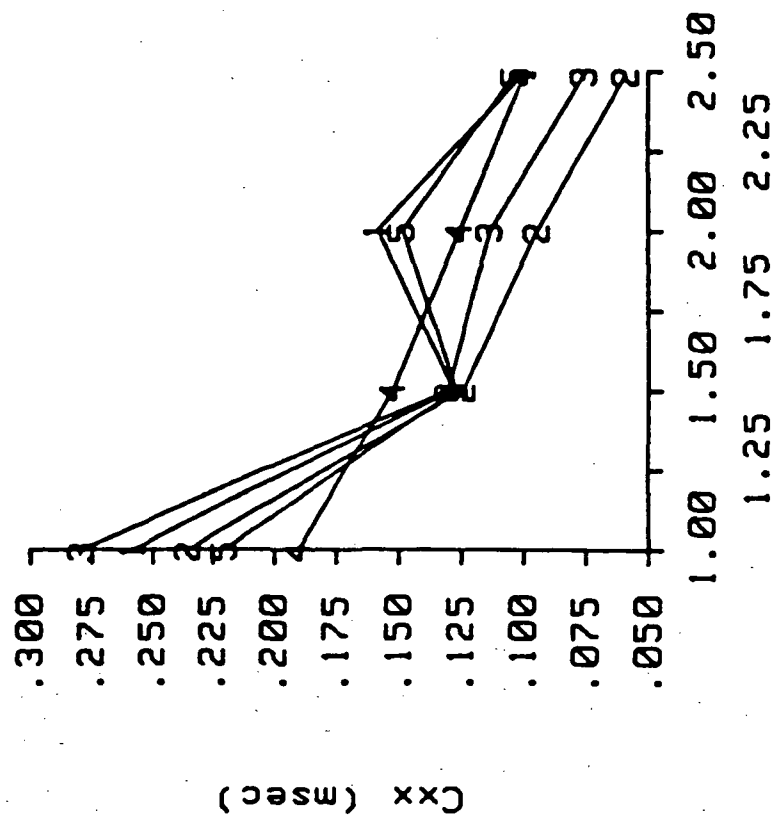
and using equation (3), the resultant radial and tangential forces are illustrated in the figure and are defined by

Pressure: 3.08 bar
Speed: 3000 rpm



Seal Taper, Hi/Ho

Pressure: 3.08 bar
Speed: 16000 rpm



Seal Taper, Hi/Ho

Fig. 18 Experimental normalized direct damping of the test seals at 3.08 bar pressure.
See Table 4 for definitions of inlet circumferential velocity symbols.

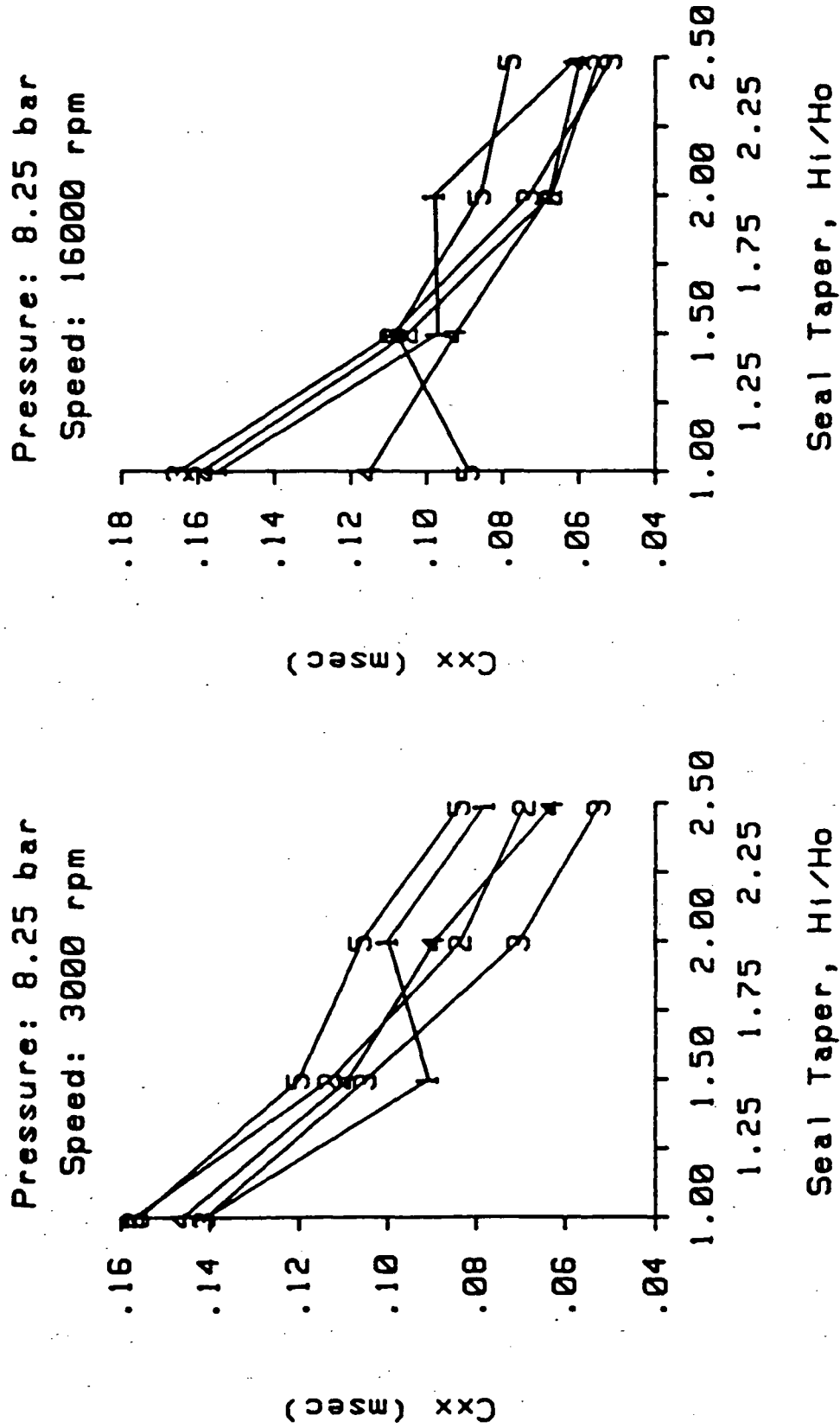


Fig. 19 Experimental normalized direct damping of the test seals at 8.25 bar pressure.
See Table 4 for definitions of inlet circumferential velocity symbols.

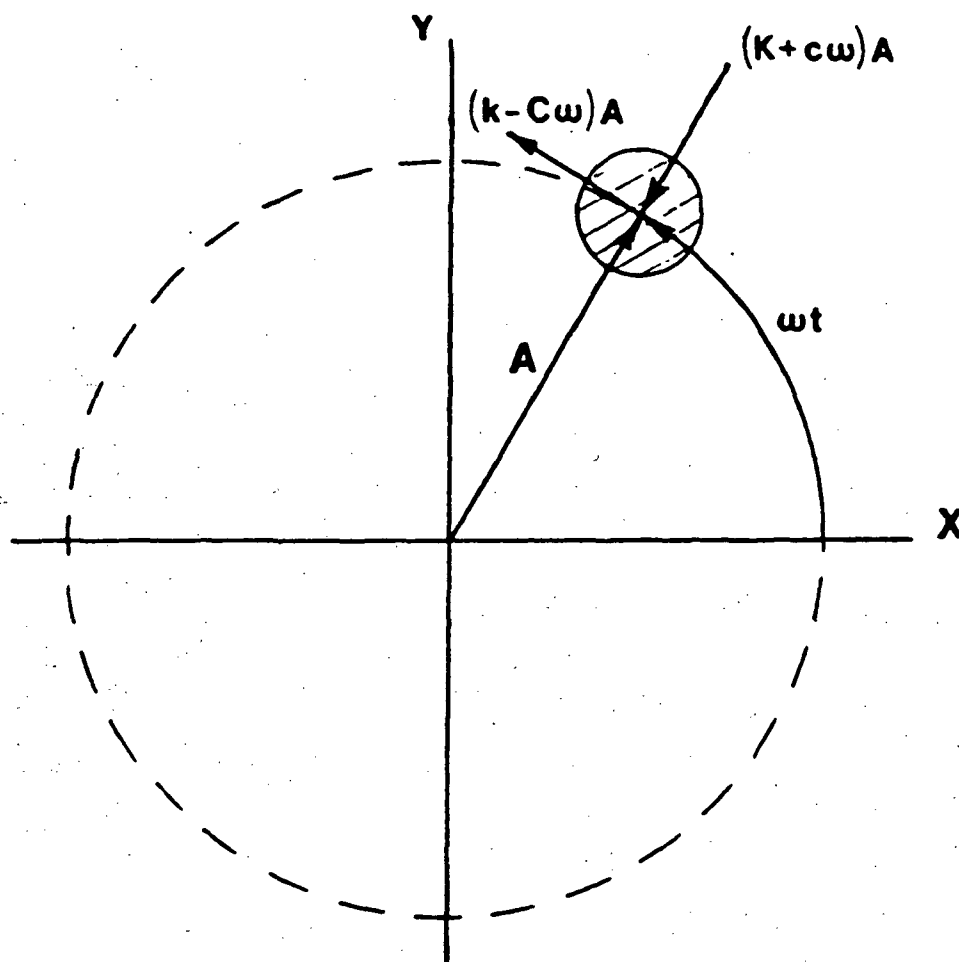


Fig. 20 Forces on a precessing seal rotor.

$$-F_r/A = K + c\Omega$$

$$F_t/A = k - C\Omega$$

If F_t/A is a positive quantity, the tangential force is destabilizing since it supports the whirling motion of the rotor. Conversely, if F_t/A is negative, it opposes the whirling motion of the rotor, and is therefore stabilizing. The whirl frequency ratio is defined by

$$\text{Whirl frequency ratio} = k / C\Omega$$

From the above discussion, if the whirl ratio is less than one, the tangential force on the rotor is stabilizing. A minimum value of the whirl frequency ratio is optimum for stability.

Fig. 21 - 24 show the whirl-frequency ratios at a running speed of 16000 rpm and a shake frequency of 74.6 Hz of the seals reported on here. From the lowest whirl frequency ratios to the highest, the seals rank as follows: seal 2.5, seal 1.5, seal 2.0, and seal 1.0.

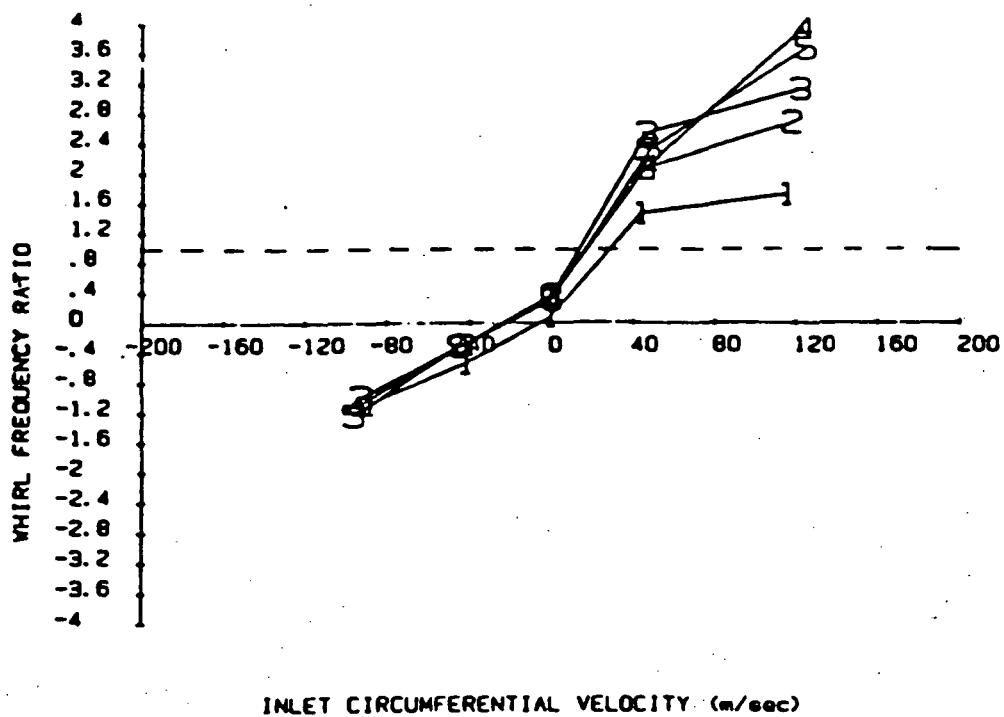


Fig. 21 Whirl frequency ratios of seal 1.0. Five pressure ratios, rotor speed = 16000 rpm, shake frequency = 74.6 Hz

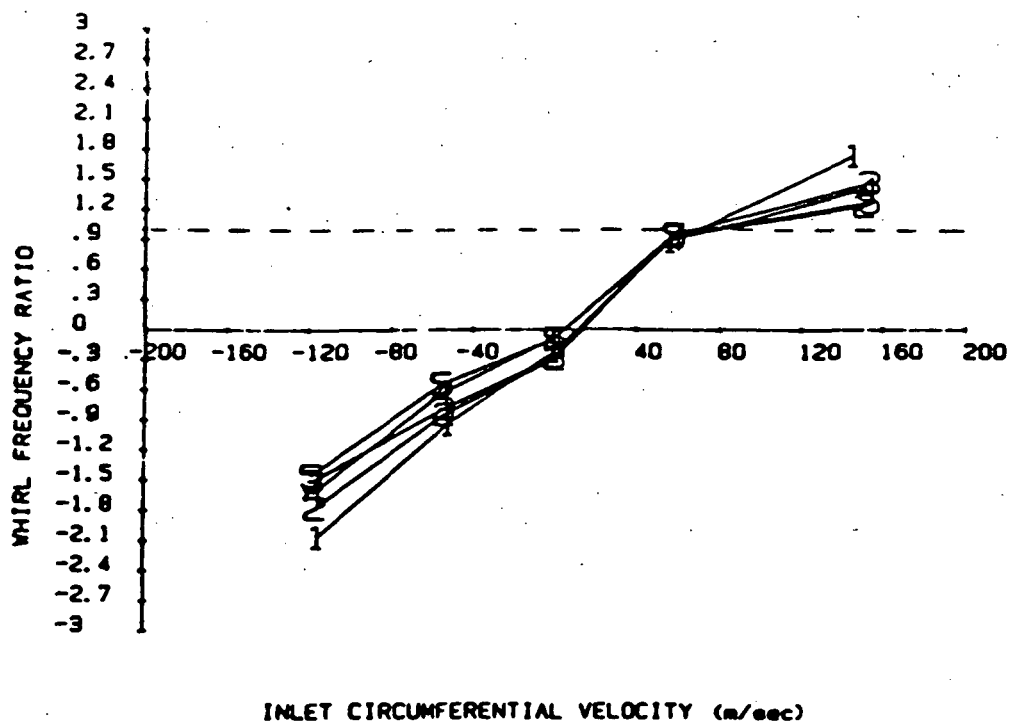


Fig. 22 Whirl frequency ratios of seal 1.5. Five pressure ratios, rotor speed = 16000 rpm, shake frequency = 74.6 Hz

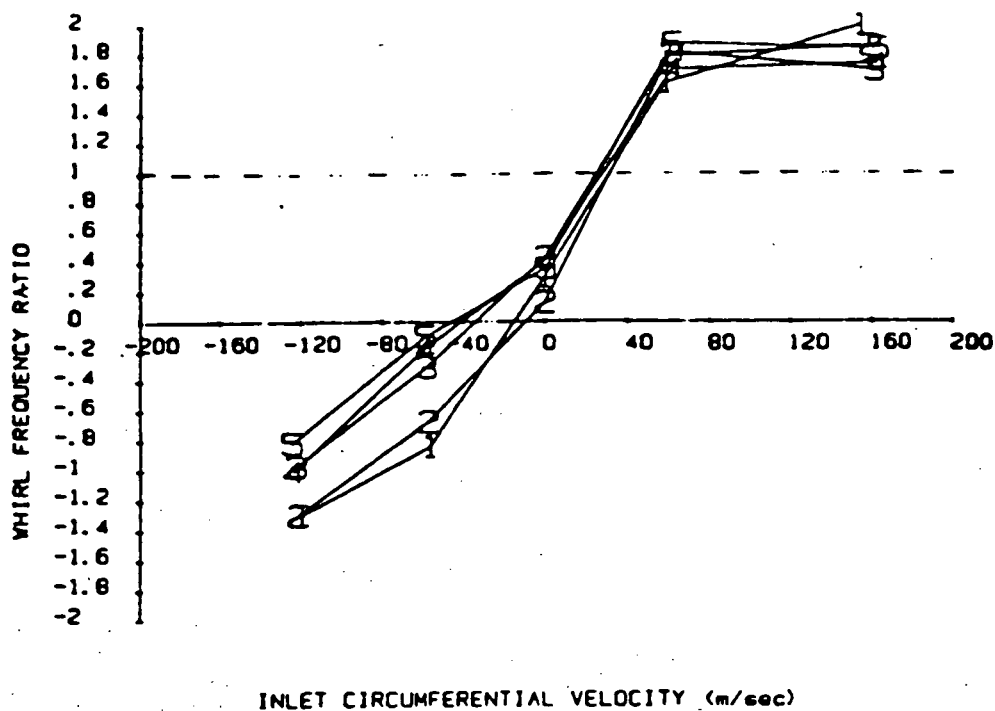


Fig. 23 Whirl frequency ratios of seal 2.0. Five pressure ratios, rotor speed = 16000 rpm, shake frequency = 74.6 Hz

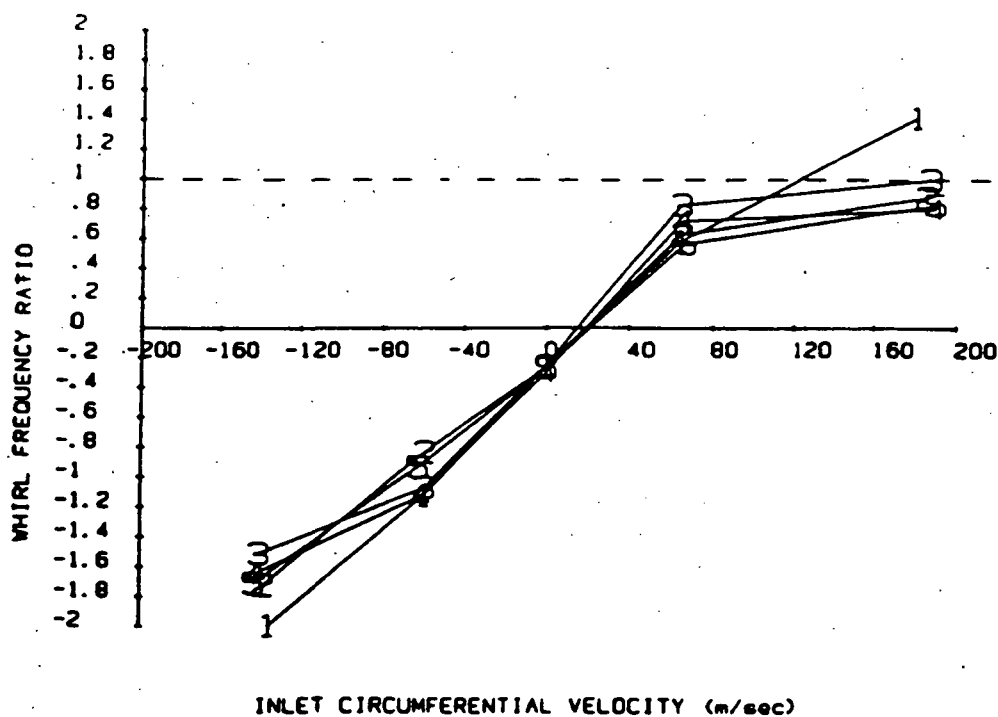


Fig. 24 Whirl frequency ratios of seal 2.5. Five pressure ratios, rotor speed = 16000 rpm, shake frequency = 74.6 Hz

CHAPTER VII

TEST RESULTS: COMPARISON TO THEORETICAL PREDICTIONS

In this chapter, the experimental results from the tests of four smooth-rotor, smooth-stator, tapered seals are compared to the predictions of an analysis developed by Nelson [10]. The seals tested are described in Tables 1 - 3. Table 4 and Fig. 7 - 10 define the symbols used in the figures.

Dependence on inlet loss coefficients. As noted previously, Nelson's analysis has underpredicted the direct stiffness of tested seals in previous comparisons. Nelson et al. [11] have suggested that inadequate modeling of the seal inlet losses could account for the underpredictions. Of the rotordynamic coefficients, direct stiffness is the most sensitive to changes in the entrance loss coefficient, \bar{k} , of equations (8) and (9). This statement is supported by the results of Fig. 25. In this figure, the broken lines represent the normalized rotordynamic coefficient values determined during a particular test of seal 1.0. The solid lines represent the values predicted by Nelson's Moody-based analysis [10] as the entrance loss varies from 0.1 to 0.9. Recall that in the entrance loss relationship of equation (8),

$$p_0(0) = \{1 + [(\gamma-1)(\bar{k}+1)M_0^2(0)] / 2\}^{\gamma/(1-\gamma)} \quad (8)$$

$p_0(0)$ is the seal entrance/reservoir pressure ratio and $M_0(0)$ is the entrance Mach number. In the past, these values, and therefore the

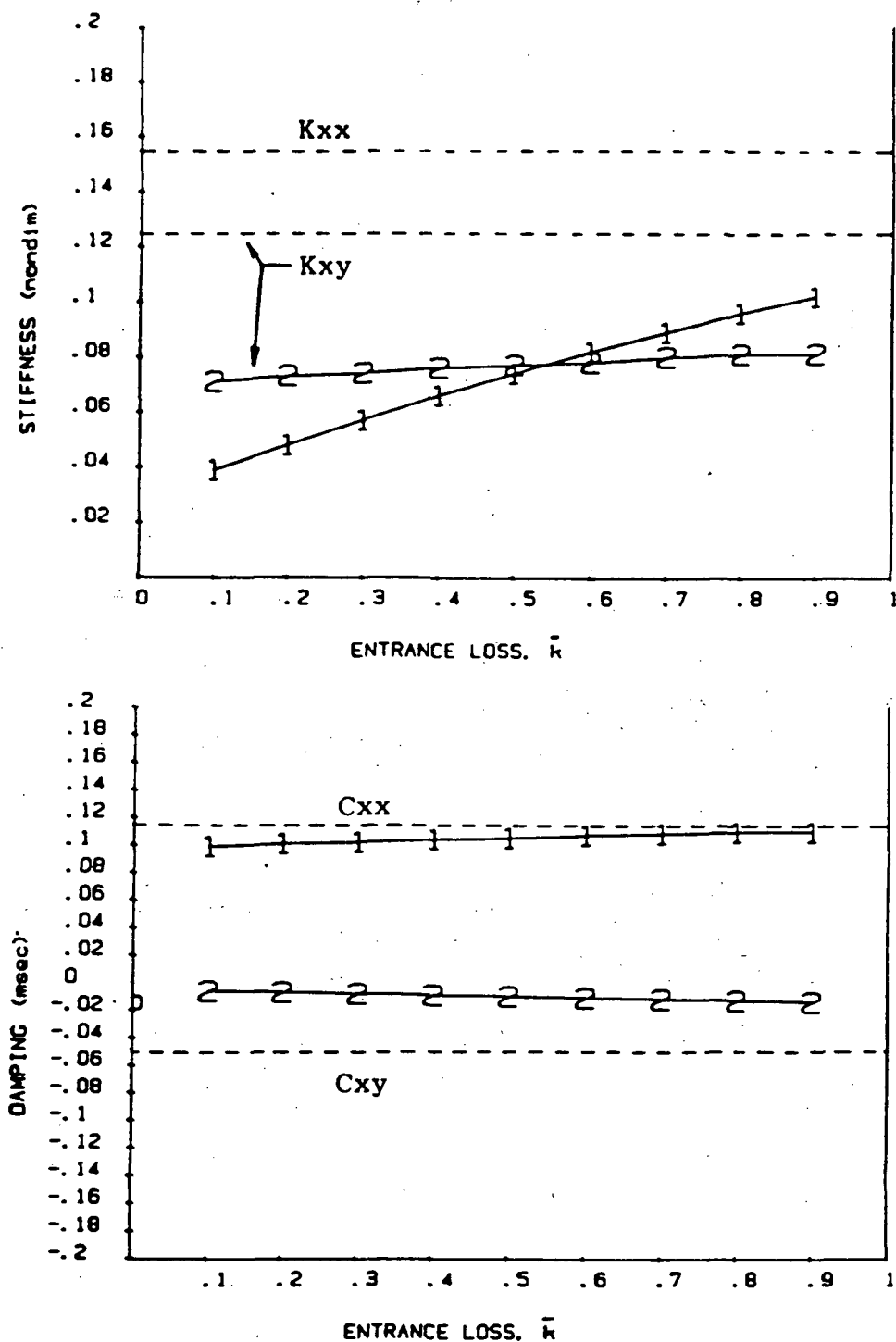


Fig. 25 Dependence of stiffness (above) and damping (below) on entrance loss coefficient. Curves 1: direct stiffness (K_{xx}) and damping (C_{xx}). Curves 2: cross coupled (K_{xy} and C_{xy}). Broken lines represent experimental data from a test of seal 1.0: rotor speed = 16000 rpm, inlet circumferential velocity = 45 m/sec, pressure = 8.25 bar.

value of \bar{k} , have been determined from pressure measurements at the first pressure tap in the inlet end of each seal. In Fig. 26, a pressure gradient plot is presented for the tests of seal 1.0 which is typical of all seals tested. The shape of the curves show that some of the entrance loss occurs after the initial sharp drop in pressure at the seal inlet. The first two data points on the curves represent the reservoir pressure for the tests. The remaining points represent the pressures measured at taps along the seal. Nelson's analysis assumes that the entrance loss occurs at the entrance. In an attempt to represent the entrance losses which actually occur in the first centimeter of the seal, a curve fit of the form

$$p(x) = P(\alpha - x)^\beta \quad (16)$$

was applied on the data points which follow the inlet loss. In equation (16), x is the axial location of the absolute pressure $p(x)$, and P , α , and β are obtained by a least squares curve fit. The value of $p(0)$ is then used as the seal entrance pressure in $p_o(0)$ of equation (8) to determine the entrance loss \bar{k} . Fig. 27 shows an example of the entrance losses thus obtained. The remaining entrance loss figures may be found in the Appendix, Fig. A17 - A26. Before leaving Fig. 26, it should be noted that five curves are plotted, one for each test rotor speed. This figure illustrates the typically negligible effect of rotor speed on the pressure distribution in the seal. Subsequent pressure plots in this report will include data from one test speed only.

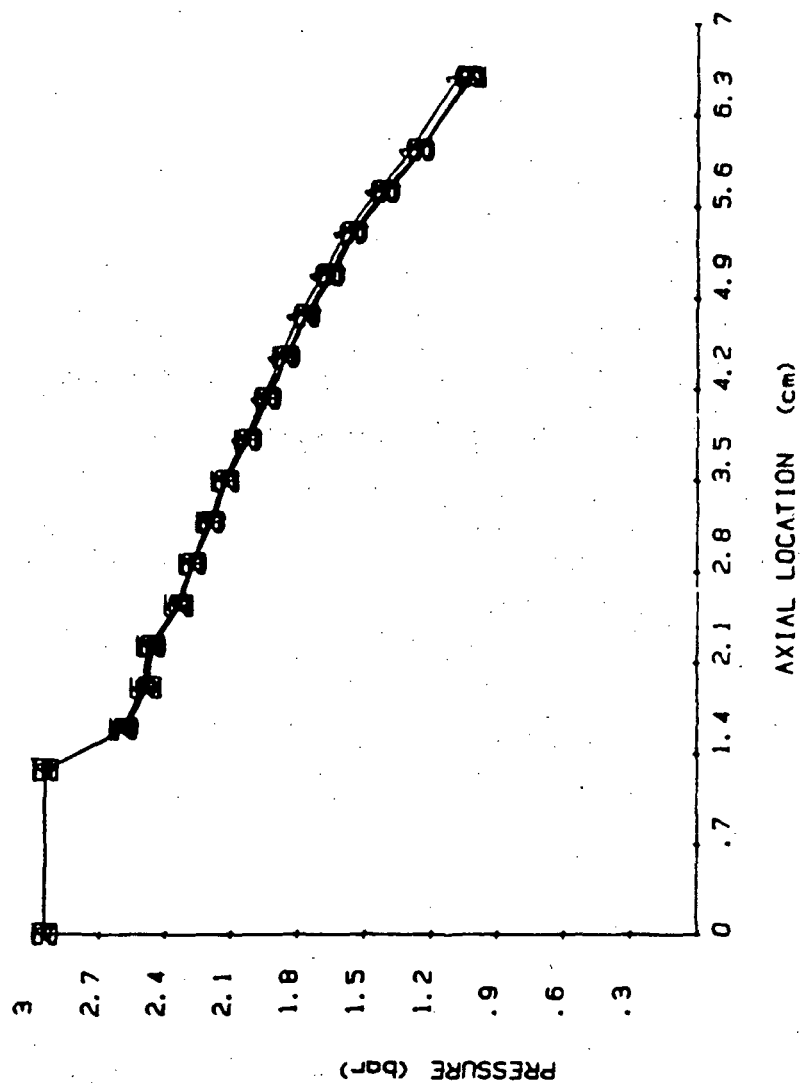


Fig. 26 Pressure gradient in seal 1.0, pressure 1, inlet swirl 4 of Table 4.

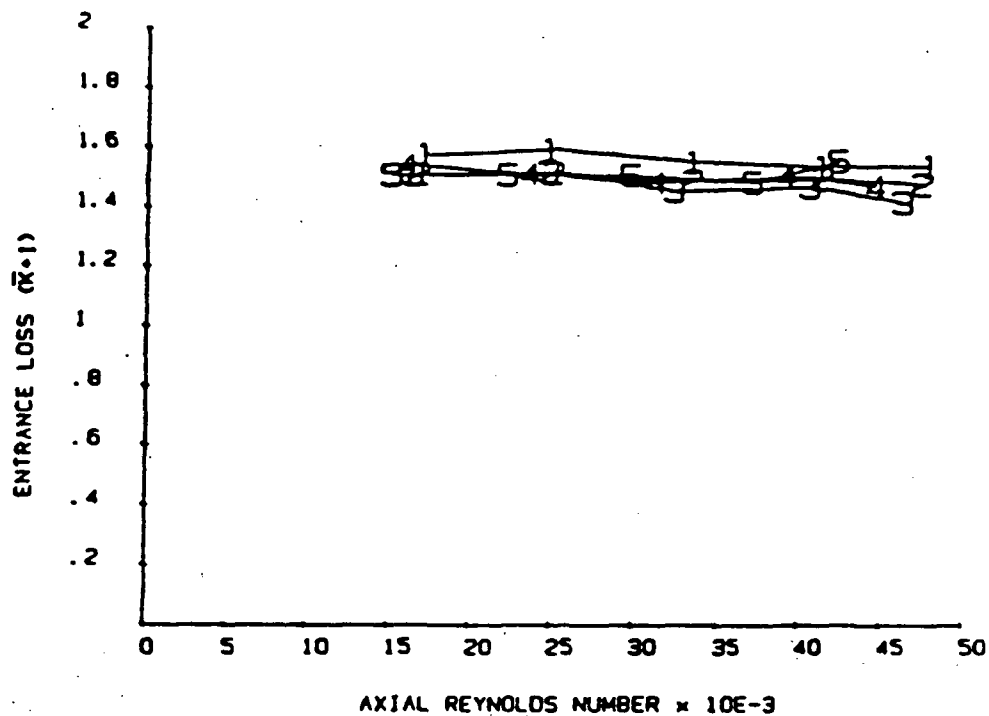


Fig. 27 Entrance loss for seal 1.0, high velocity swirl in the direction of rotor rotation.

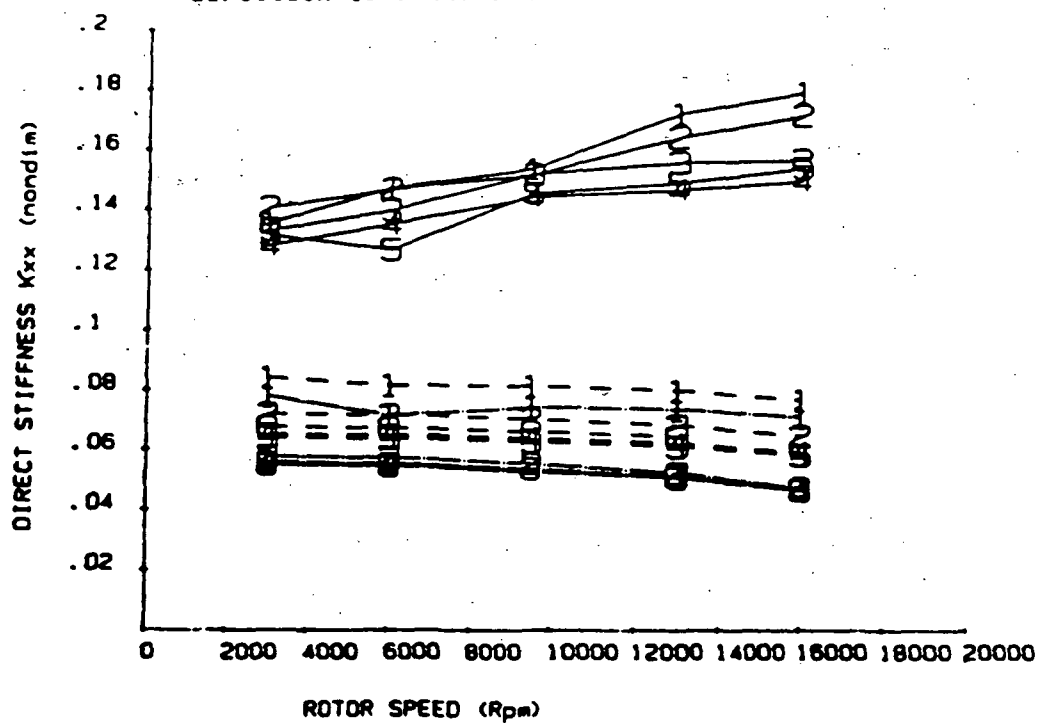


Fig. 28 Direct stiffness, comparison of Nelson's analyses (low velocity swirl in the direction of rotor rotation). Solid - experimental; dash - Moody; dash-dot-dash - Hirs

Comparison of Nelson's analyses. In the comparison of his Hirs-based and Moody-based analyses, Nelson [10] used a water seal for input parameters. He found that the use of Moody's equation resulted in higher direct and cross-coupled stiffness predictions for "rough" seals ($e/2H_0 = 0.05$), but that the differences were small for relative roughness near zero. There was little difference in the direct damping predictions of the two analyses.

Fig. 28 - 30 show a comparison of the predictions of Nelson's analyses using input data from the tests of seal 1.0. In these figures, solid lines represent experimental data, dash lines are the predictions of Nelson's Moody-based analysis, and dash-dot-dash lines are the predictions of Nelson's Hirs-based analysis. Though the measured relative roughnesses of the rotor and stator of seal 1.0 were only 0.00034 and 0.00050, respectively, the direct stiffness predicted by Nelson's Moody-based analysis was from 10 to 25% higher than predicted by the Hirs-based analysis. The cross-coupled stiffness and direct damping predictions differed by less than 10%.

Static results comparison. Fig. 31 - 38 and Fig. A1 - A16 in the Appendix are useful in the evaluation of Nelson's analysis which uses Moody's equation. In the comparison plots, the theoretical predictions and experimental results are represented by broken and solid lines, respectively. The numbers on the plotted lines refer to the inlet conditions listed in Table 4. Comparisons of leakage predictions to experimental results may be found in Fig. 31, 32, and A1 - A4. Predictions of increasing leakage with increasing inlet

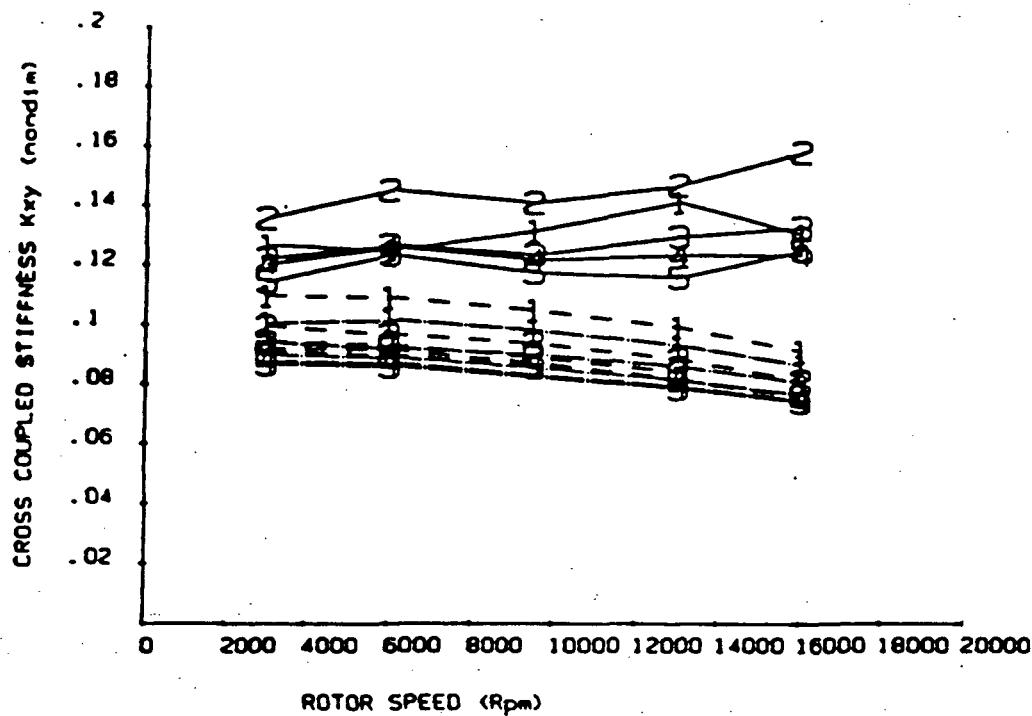


Fig. 29 Cross-coupled stiffness, comparison of Nelson's analyses (see Fig. 28 for explanation of curves).

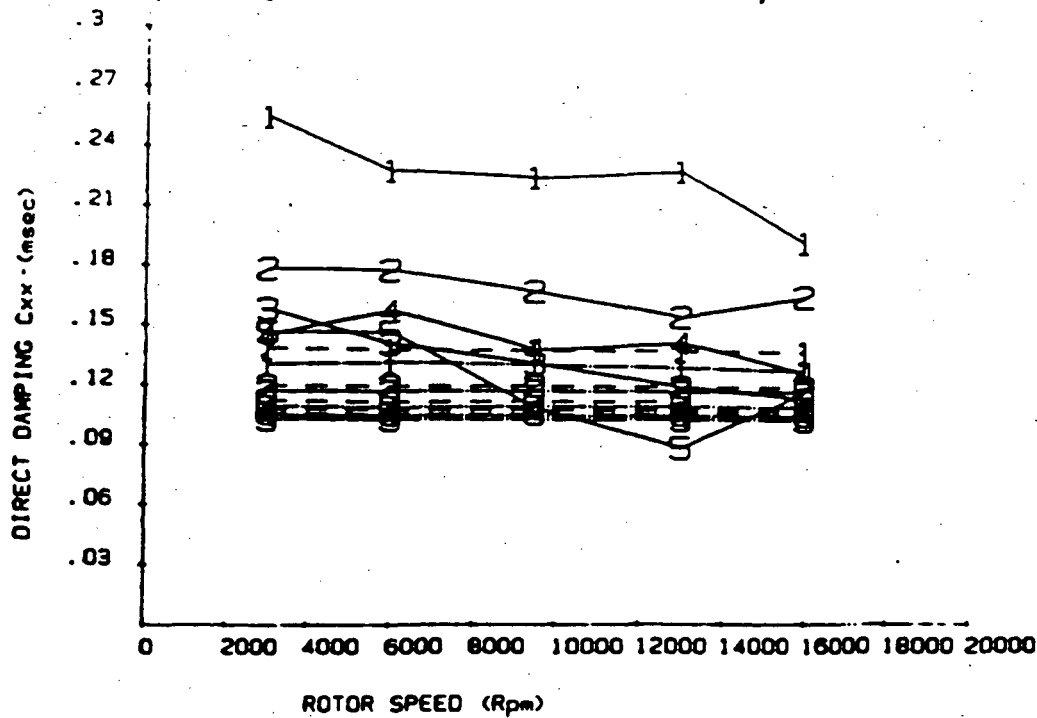


Fig. 30 Direct damping, comparison of Nelson's analyses (see Fig. 28 for explanation of curves).

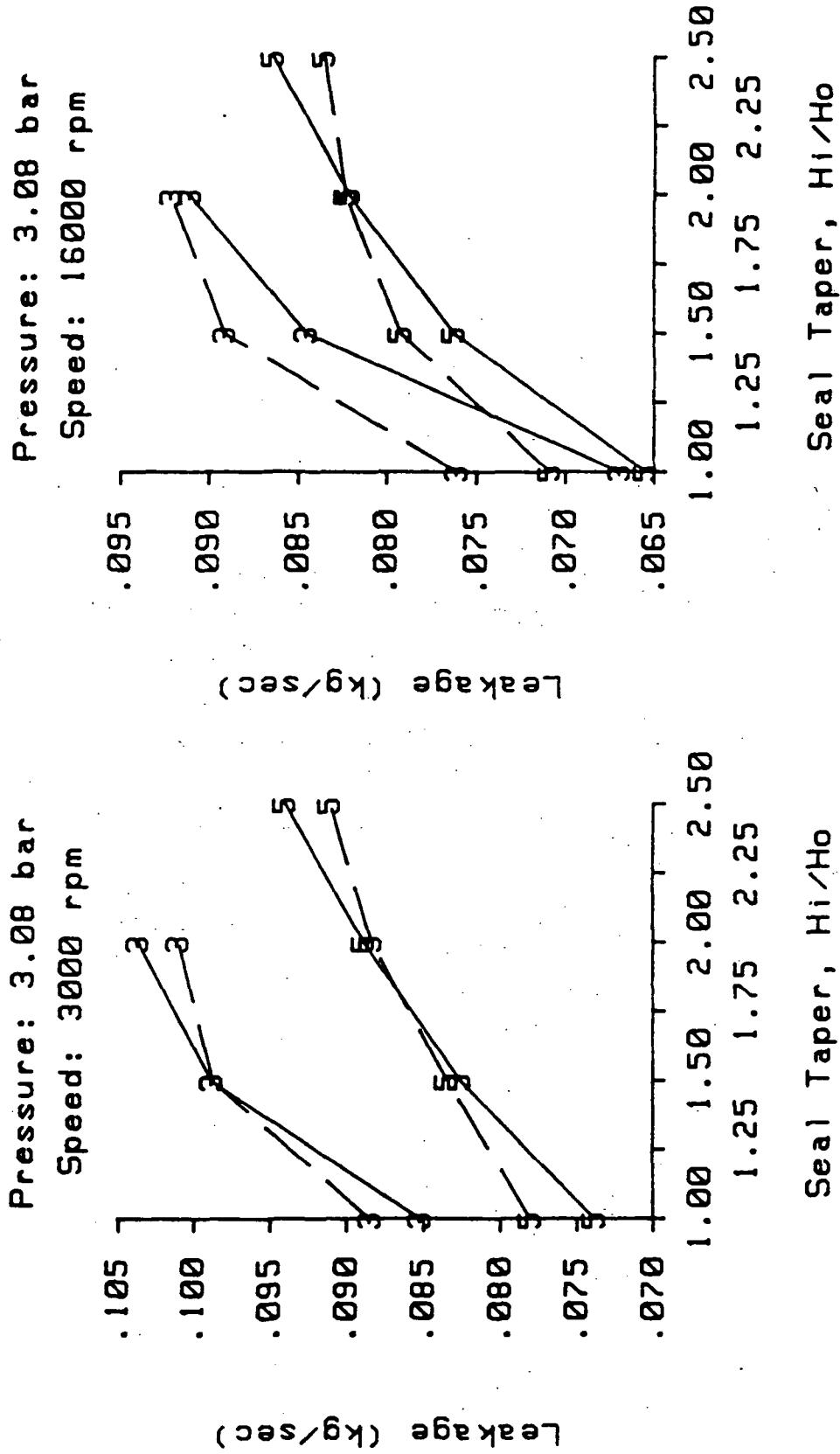


Fig. 31 Experimental and theoretical mass flow rates of air through the test seals at 3.08 bar pressure. See Table 4 for definitions of circumferential velocity symbols. Solid lines - experiment; broken lines - theory.

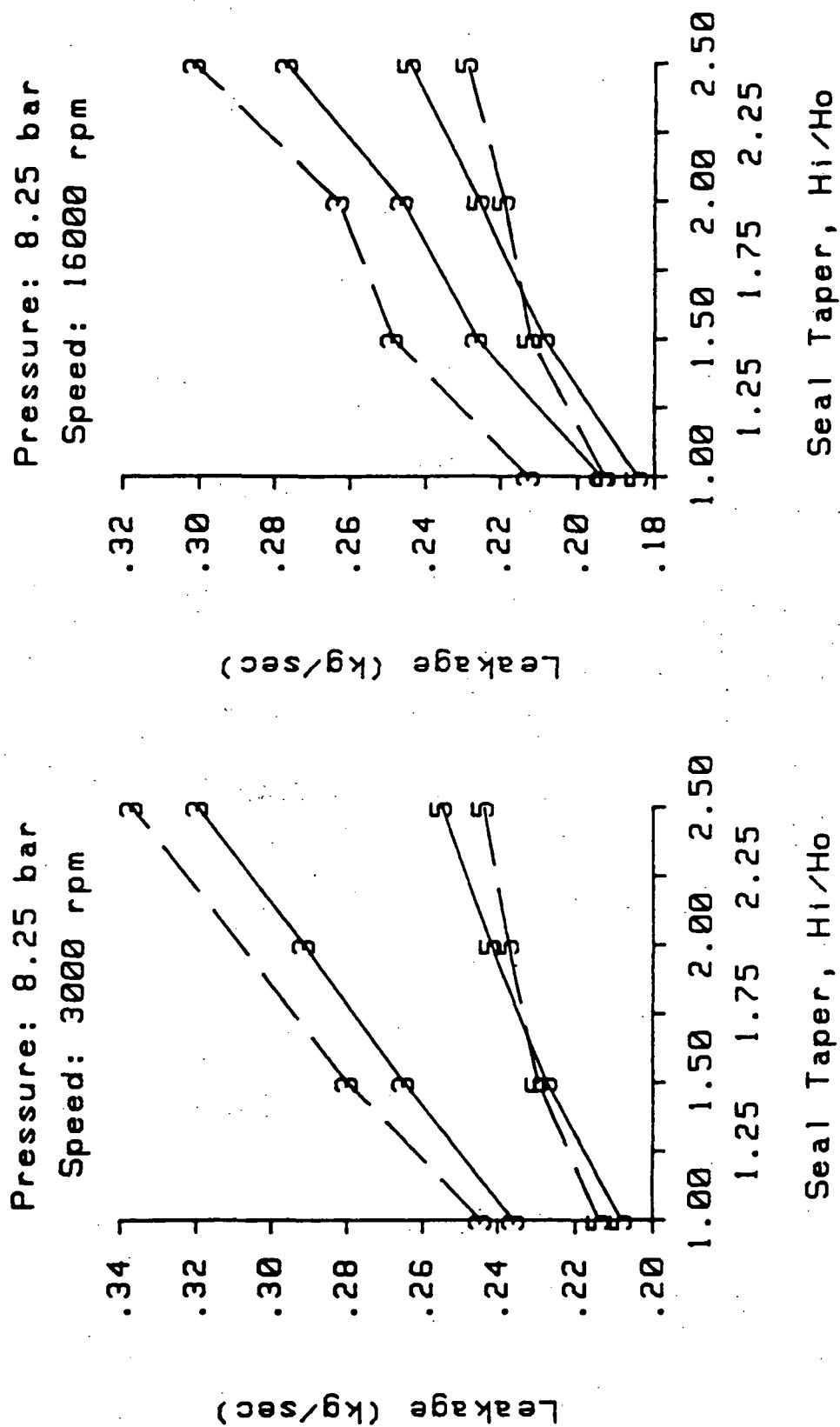


Fig. 32 Experimental and theoretical mass flow rates of air through the test seals at 8.25 bar pressure. See Table 4 for definitions of circumferential velocity symbols. Solid lines - experiment; broken lines - theory.

clearance agree with experimental results. The predictions were within 5% of the measured mass flow rate in some cases, and always within 15%.

Plots of the theoretical and experimental pressure gradient in each seal are in Fig. A27 - A37 in the Appendix. The plots show good agreement between theory and experiment. Most of the predicted pressure gradients for the seals have larger pressure drops at the inlet than do the experimental gradients because the entrance loss in Nelson's model takes place at the inlet, while experimentally it appears to take place in the first centimeter of the seal. Also, the slopes of the experimental gradients are steeper than the predicted gradient slopes. One explanation is that the experimental gradients were measured along the stator, which was rougher than the rotor in all cases, while the theoretical gradients are developed from the combined effect of the rotor and stator roughnesses. A final observation may be made concerning the erratic shape of the experimental pressure gradients of seals 1.5 and 2.0. While the sixteen pressure taps of seals 1.0 and 2.5 were aligned, as in Fig. 6, the arrangement was different for seals 1.5 and 2.0. In these seals, which were fabricated first, the first eight pressure taps were aligned as in Fig. 6, and the last eight were aligned 90° counter-clockwise from the first eight. The sharp drop in pressure after the eighth pressure tap in the experimental pressure gradients of seal 1.5 and the similar shape for seal 2.0 are thought to be a result of this arrangement. The selection of data used in the

pressure curve fits described in the section on entrance losses was made more difficult by these phenomena.

Dynamic results comparison. The dynamic results compared include the normalized experimental and theoretical direct and cross-coupled stiffness and direct damping coefficients. A cross-coupled damping comparison has been omitted because of the uncertainty present in the experimental values (see the Relative uncertainty section). Of the remaining three coefficients, the direct stiffness comparison will be presented first, and the cross-coupled stiffness comparison will be last.

Direct stiffness. Fig. 33, 34, and A5 - A8 in the Appendix show the theoretical and experimental direct stiffnesses of the four seals tested. Fig. 33 and 34 show the theoretical and experimental dependence of direct stiffness on seal taper. The data plotted are for inlet swirl configurations 3 and 5 of Table 4. Nelson's analysis predicts significantly higher direct stiffnesses for seals 1.5, 2.0, and 2.5 than it predicts for seal 1.0. Furthermore, the analysis predicts that seal 1.5 is the stiffest seal and does not predict that seal 2.0 is stiffer than seal 2.5 for high-speed inlet swirl in the direction of rotor rotation. Experimentally, little difference was present in the stiffness of seals 1.0 and 1.5 at 16000 rpm, seal 2.0 was generally the stiffest seal, and seals 1.5 and 2.0 were always stiffer than seal 2.5.

The greatest difference between theoretical and experimental direct stiffness coefficients for a seal is seen in Fig. A5, where

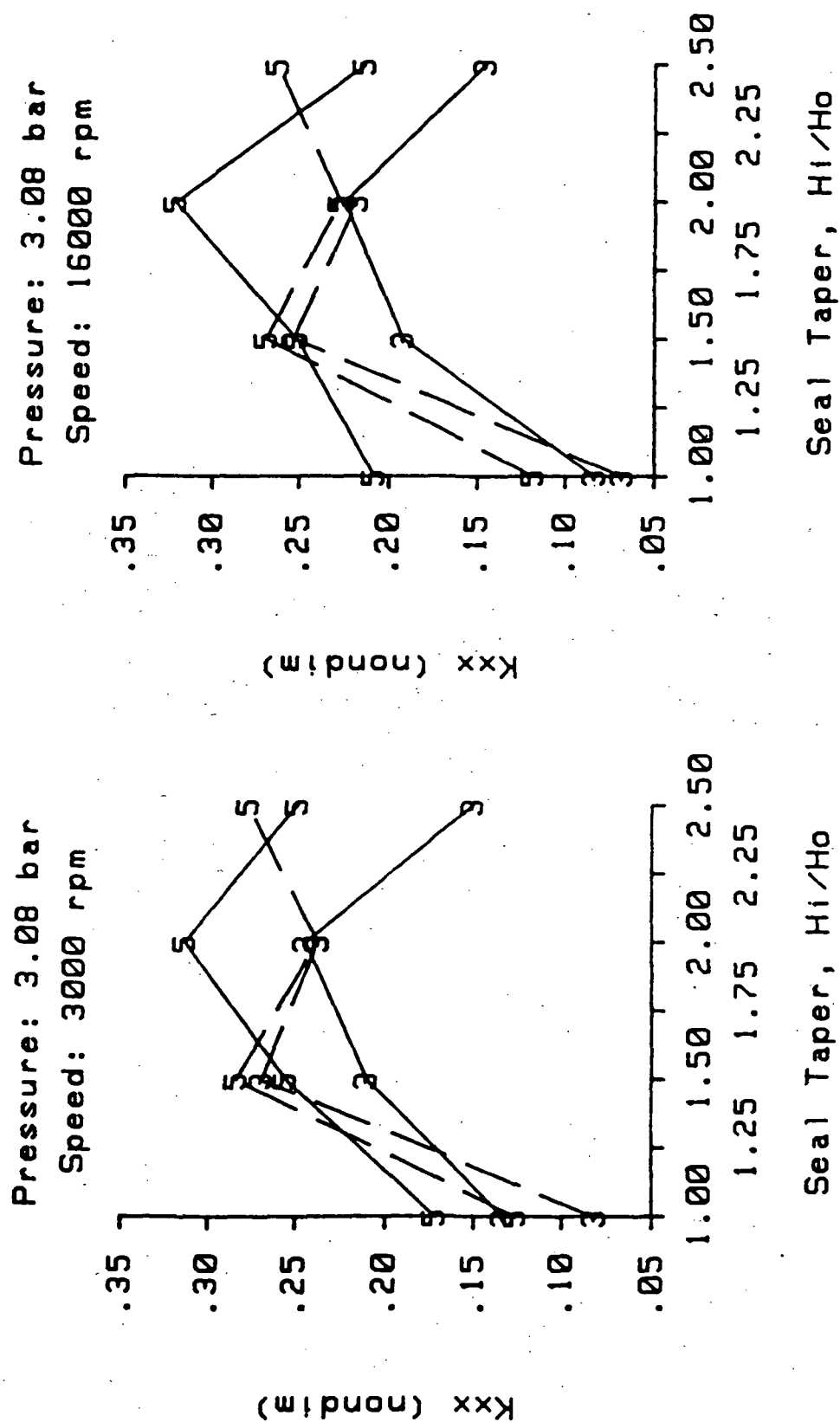


Fig. 33 Experimental and theoretical normalized direct stiffnesses of the test seals at 3.08 bar pressure. See Table 4 for definitions of circumferential velocity symbols. Solid lines - experiment; broken lines - theory.

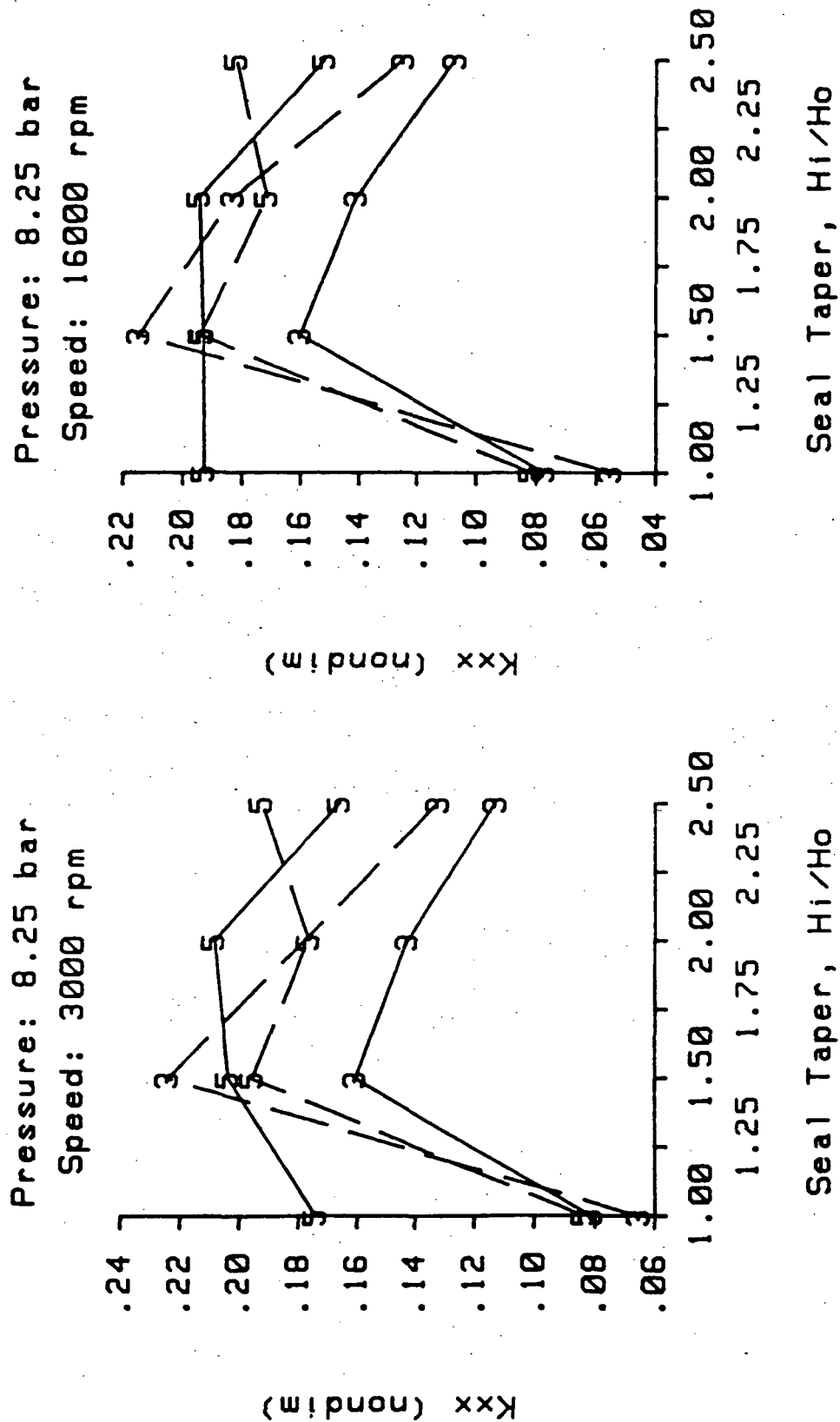


Fig. 34 Experimental and theoretical normalized direct stiffnesses of the test seals at 8.25 bar pressure. See Table 4 for definitions of circumferential velocity symbols. Solid lines - experiment; broken lines - theory.

agreement for seal 1.0 is best for inlet air swirl opposing the rotor rotation direction. The experimental direct stiffness was more speed- and swirl-velocity dependent than predicted. For swirl in the direction of rotor rotation, theory underpredicts the experimental values by 30 to 60% at the 16000 rpm rotor speed. The direct stiffness predictions for the remaining seals were generally within 30% of the experimental values, with a number of predictions within 10%. The greatest disagreement is in the non-prerotated case for each seal. Experimentally, the direct stiffness for a given inlet pressure was lowest for this case, while theory predicts a higher value for the non-prerotated case than for the two low speed swirl cases.

Direct damping. In the comparison of the normalized theoretical and experimental direct damping data (Fig. 35, 36, and A13 - A16 in the Appendix), recall that the estimated uncertainty was generally from 10 to 20% of the experimental direct damping. The predictions of Nelson's analysis were generally within 30% of the experimentally determined direct damping of seals 1.5, 2.0, and 2.5. The same is true of seal 1.0 at the three higher inlet pressures of Table 4. However, at the two lower pressures, theory underpredicts experiment by up to 60%. A general trend of decreasing damping with increasing taper is present in both experimental and theoretical results.

Cross-coupled stiffness. Fig. 37 and 38 show that the experimental cross-coupled stiffness of seal 1.5 was 30 to 50% less than that of seal 1.0 for inlet swirl configuration 5 of Table 4. Nelson's

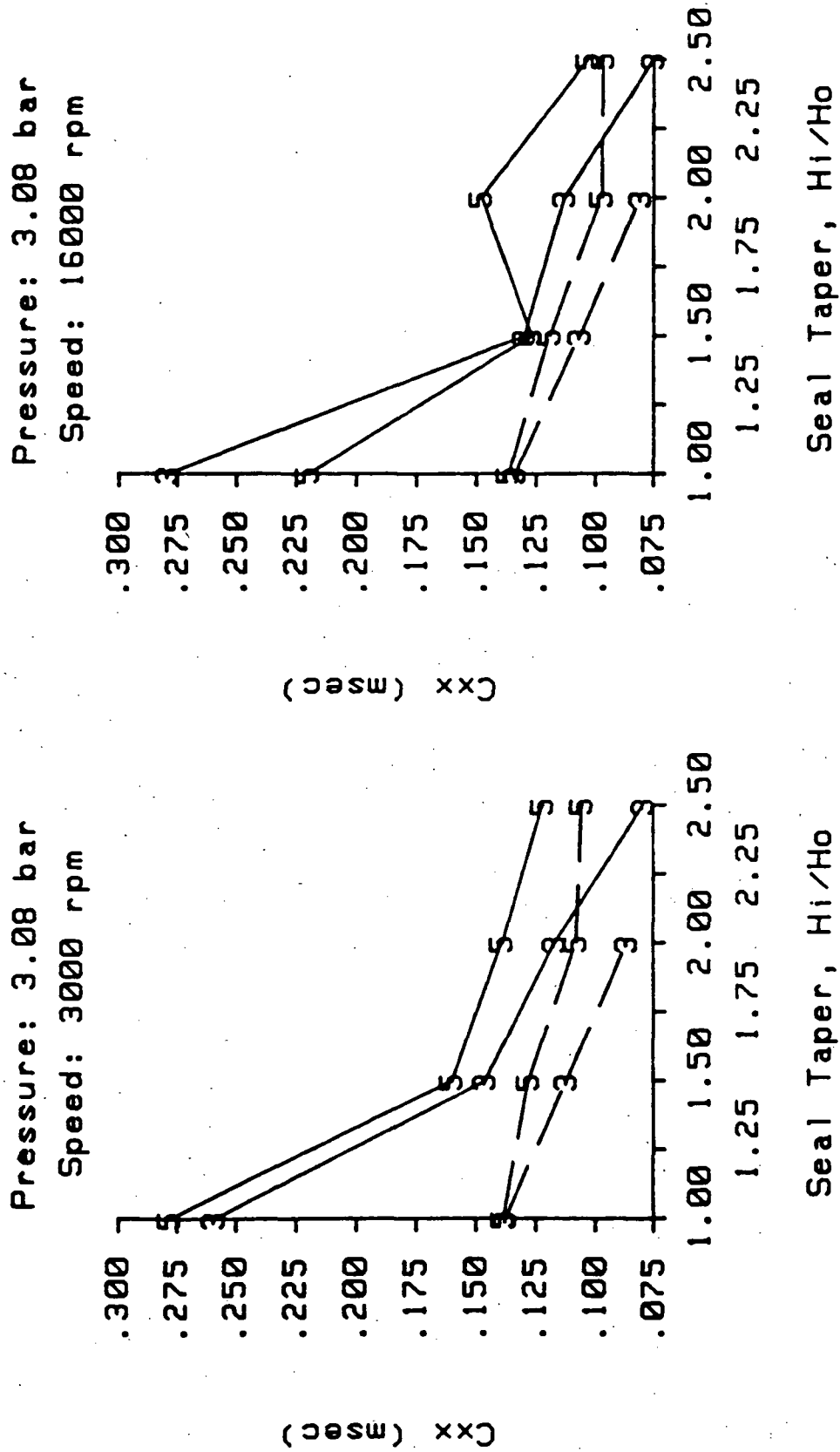


Fig. 35 Experimental and theoretical normalized direct damping of the test seals at 3.08 bar pressure. See Table 4 for definitions of circumferential velocity symbols. Solid lines - experiment; broken lines - theory.

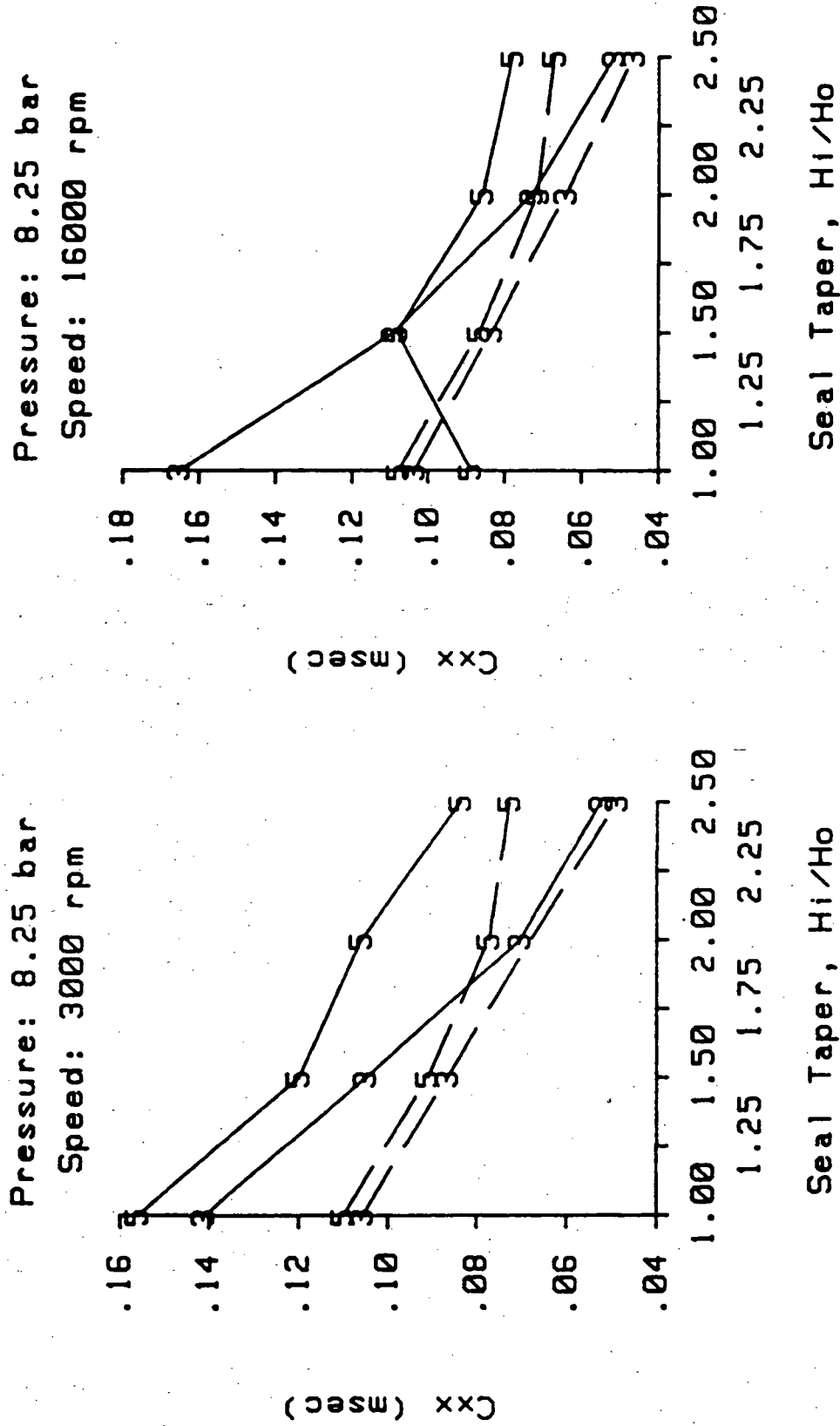


Fig. 36 Experimental and theoretical normalized direct damping of the test seals at 8.25 bar pressure. See Table 4 for definitions of circumferential velocity symbols. Solid lines - experiment; broken lines - theory.

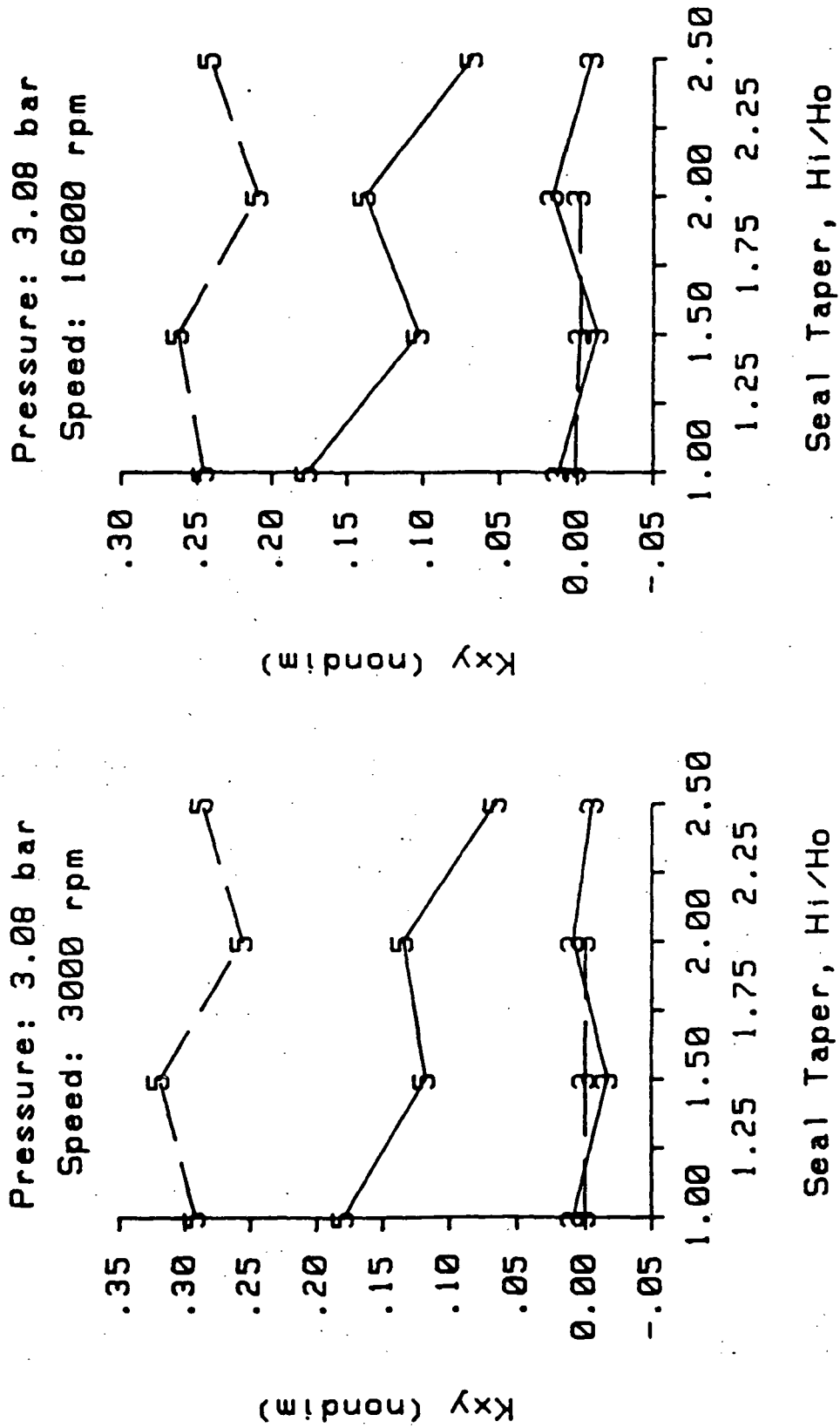


Fig. 37 Experimental and theoretical normalized cross-coupled stiffnesses of the test seals at 3.08 bar pressure. See Table 4 for definitions of circumferential velocity symbols. Solid lines - experiment; broken lines - theory.

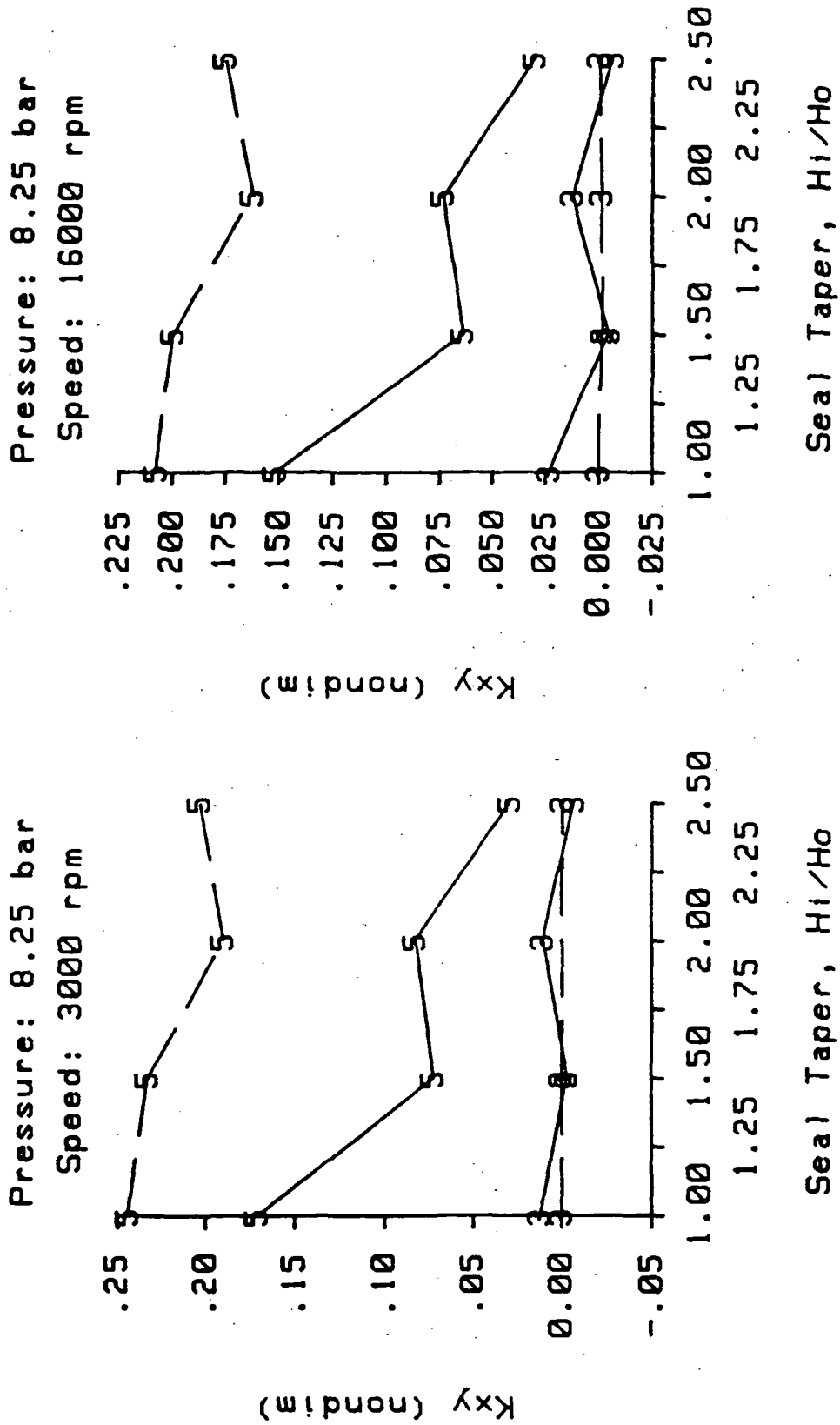


Fig. 38 Experimental and theoretical normalized cross-coupled stiffnesses of the test seals at 8.25 bar pressure. See Table 4 for definitions of circumferential velocity symbols. Solid lines - experiment; broken lines - theory.

analysis predicts little difference between the cross-coupled stiffnesses of seals 1.0 and 1.5. In addition, the experimental cross-coupled stiffness values of seal 2.0 were higher than those of seals 1.5 and 2.5, but Nelson's analysis predicts that seal 2.0 has lower values than seals 1.5 and 2.5.

For a given seal, Nelson's analysis predicts an almost linear relationship between cross-coupled stiffness and the circumferential velocity of the inlet air (Fig. A9 - A12 in the Appendix). Experimentally, the relationship is near linear through the low speed swirl in the direction of rotor rotation. The linearity is not present when the inlet swirl speed is further increased. As a result, the normalized cross-coupled stiffness predictions are as much as seven times (seal 2.5) greater than the experimental values at the highest circumferential velocity of the inlet air. Agreement is best when the magnitude of the inlet swirl velocity is less than eighty meters per second.

Stability analysis. The whirl frequency ratio, a measure of seal stability, was defined in an earlier section. Fig's. 39 - 42 present the whirl ratios predicted by Nelson's analysis for the seals at the 16000 rpm rotor speed. Five curves are present in each figure, one for each inlet pressure applied (see Table 4). Fig's. 21 - 24 provide the corresponding plots of experimental whirl ratios. For inlet swirl in the direction of rotor rotation (positive circumferential velocity of the inlet air), the most frequent situation in practice, Nelson predicts less stability for each seal

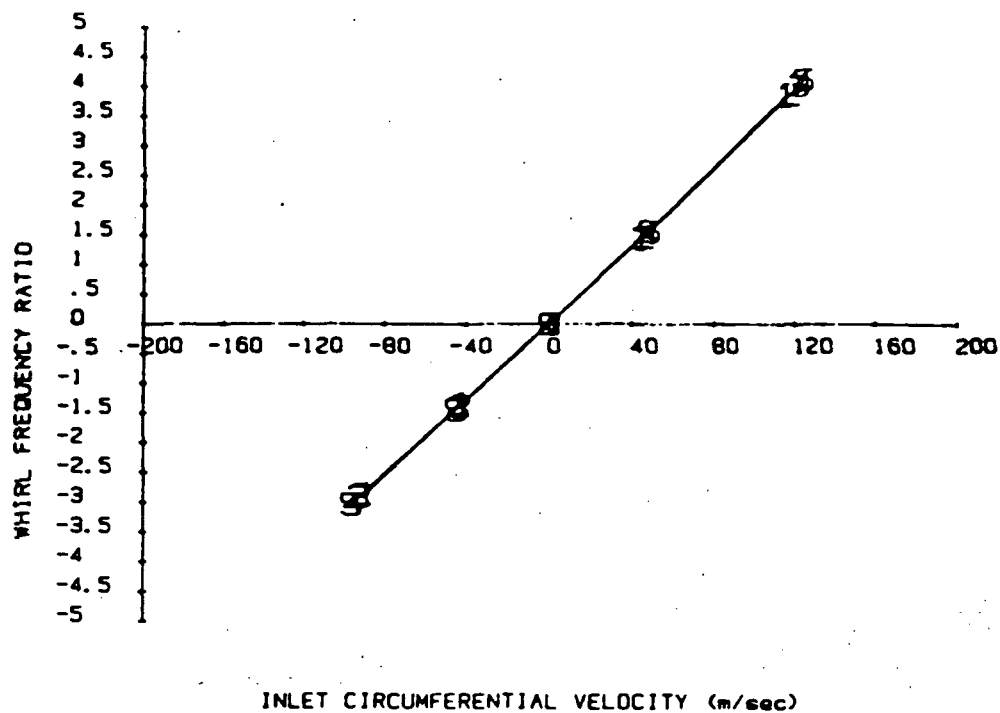


Fig. 39 Theoretical whirl frequency ratios of seal 1.0 at 16000 rpm.

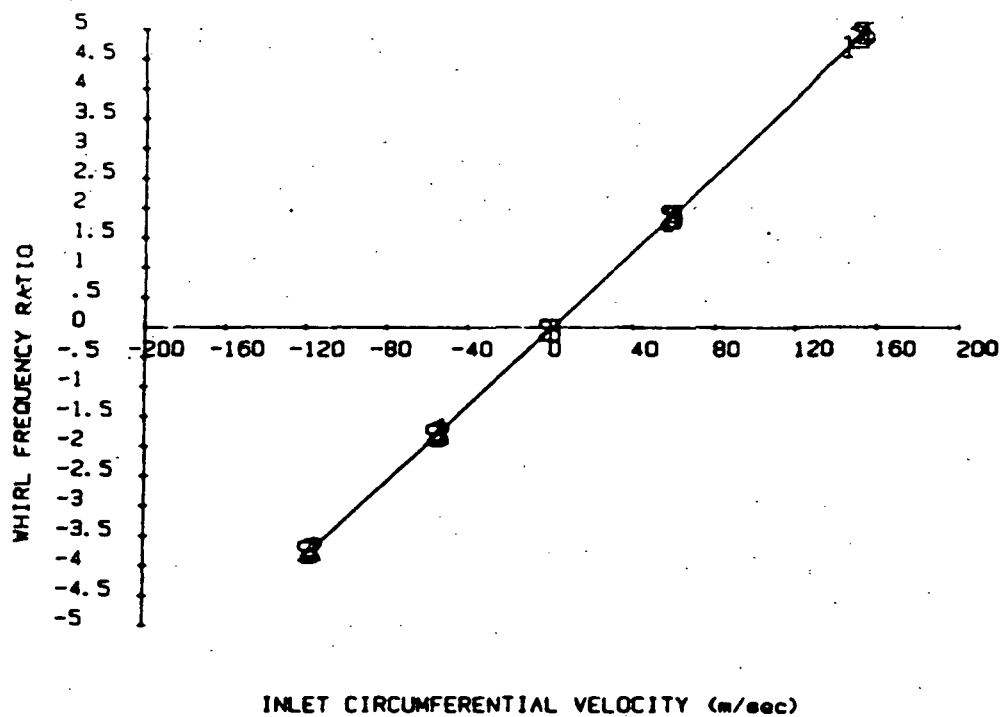


Fig. 40 Theoretical whirl frequency ratios of seal 1.5 at 16000 rpm.

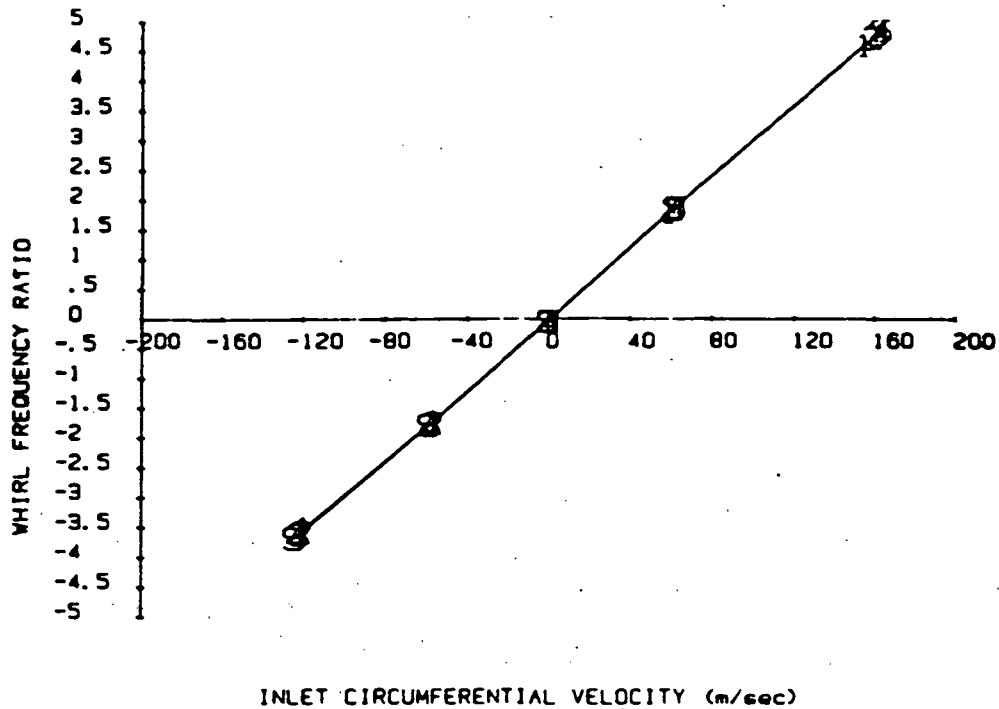


Fig. 41 Theoretical whirl frequency ratios of seal 2.0 at 16000 rpm.

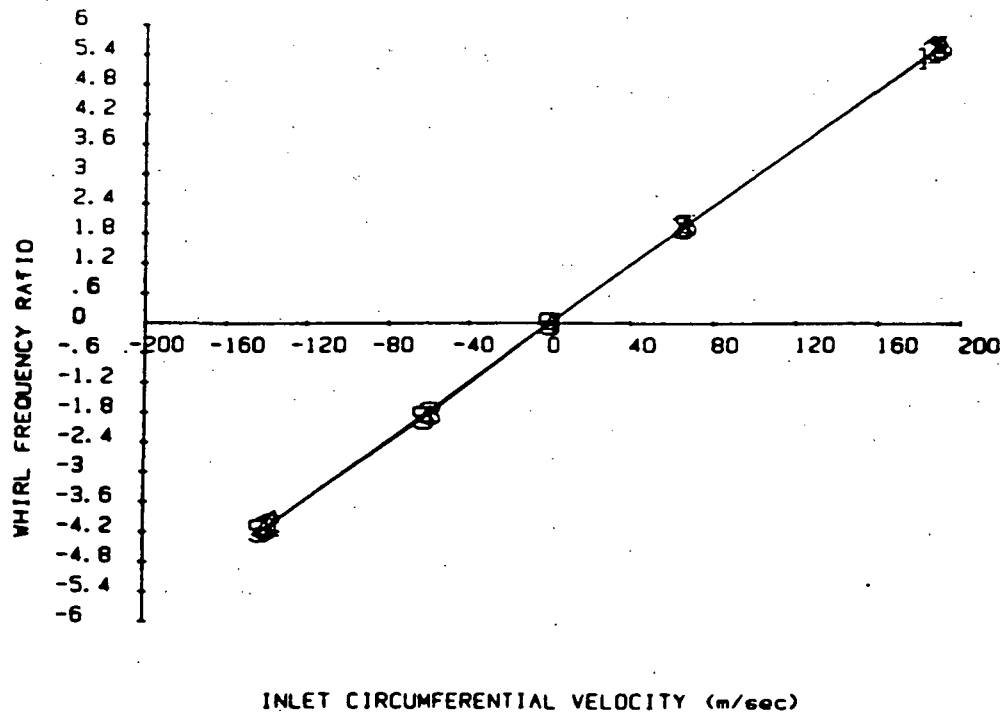


Fig. 42 Theoretical whirl frequency ratios of seal 2.5 at 16000 rpm.

than was found experimentally. This is a result of cross-coupled stiffness overpredictions and direct damping underpredictions. The difference in predicted whirl frequency ratios among the seals are so small at a given inlet circumferential velocity that stability comparisons are inconclusive.

CHAPTER VIII

CONCLUSIONS

An air seal test apparatus at Texas A & M University has been modified to enable tests at rotor speeds up to 16000 rpm. A previously established method of determining seal rotordynamic coefficients has been used to obtain consistent, repeatable stiffness and direct damping results.

The experimental and theoretical results of the preceding section support the following conclusions:

(a) Four smooth-rotor/smooth-stator seals with equal exit clearances were tested. The inlet to exit clearance ratios (tapers) of the seals were 1.0, 1.5, 2.0, and 2.5. The leakage through seals 1.5, 2.0, and 2.5 were greater than through seal 1.0 by 15 to 25%, 25 to 40%, and 45 to 60%, respectively.

(b) Throughout the tests, the differences in the rotordynamic behavior of seals 1.5 and 2.0 were small.

(c) Generally, seals 1.5 and 2.0 had clearly higher normalized experimental direct stiffness coefficients than seals 1.0 and 2.5. At a rotor speed of 16000 rpm, seal 1.0 was sometimes stiffer than seal 2.5.

(d) The direct stiffness of seal 1.0 is speed dependent for inlet air swirl in the direction of rotor rotation. At rotor speeds in excess of 16000 rpm, seal 1.0 might prove stiffer than seals 1.5 and 2.0 for inlet swirl in the direction of rotor rotation.

(e) A comparison of the experimental cross-coupled stiffness and direct damping of the seals through the whirl frequency ratio (a nondimensional stability indicator) leads to the following seal ranking, in order of decreasing stability: seal 2.5, seal 1.5, seal 2.0, and seal 1.0.

(f) For rotor speeds up to 16000 rpm, the effects of speed increases on the rotordynamic coefficients of the smooth-rotor/smooth-stator seals tested are mainly due to the seal clearance reduction as the rotor grows.

(g) The evaluation of seal entrance losses is critical when using Nelson's analysis to predict seal performance. Aside from direct test data, no readily available source of information in this area is known.

(h) Although the experimental direct stiffness of seal 1.0 was always lower than that of seals 1.5 and 2.0, the uncommon speed dependence of seal 1.0 made the difference modest for inlet air swirl in the direction of rotor rotation at a rotor speed of 16000 rpm. Nelson's analysis indicates that seals 1.5 and 2.0 are significantly stiffer than seal 1.0 at all speeds and inlet swirls tested. In addition, Nelson's analysis predicts the normalized direct stiffness of seal 2.5 to be slightly higher than that of seal 2.0 for high speed inlet air swirl in the direction of rotor rotation, but seal 2.0 was always clearly stiffer than seal 2.5 experimentally.

(i) The normalized direct damping predictions of Nelson's analysis are generally within 30% of the experimental results. A

trend of decreasing damping with increasing taper is present in both experimental and theoretical results.

(j) Nelson's analysis predicts little difference between the cross-coupled stiffnesses of seals 1.0 and 1.5. Experimentally, the normalized cross-coupled stiffness of seal 1.5 was 30 to 50% less than that of seal 1.0. Furthermore, Nelson's analysis predicts a linear relationship between cross-coupled stiffness and the circumferential velocity of the inlet air, which is not present experimentally. Cross-coupled stiffness predictions are as much as seven times greater than experimental values for high inlet circumferential air velocities.

REFERENCES

1 Black, H.F., and Jenssen, D.N., "Dynamic Hybrid Properties of Annular Pressure Seals," Proc. J. Mech. Engin., Vol. 184, pp. 92-100, 1970.

2 Jenssen, D.N., "Dynamics of Rotor Systems Embodying High-Pressure Ring Seals," Ph.D. dissertation, Herriot-Watt Univ., Edinburgh, Scotland, July 1970.

3 Black, H.F., and Jenssen, D.N., "Effects of High-Pressure Ring Seals on Pump Rotor Vibrations," ASME Paper No. 71-WA/FF-38, 1971.

4 Childs, D.W., "The Space Shuttle Main Engine High-Pressure Fuel Turbopump Rotordynamic Instability Problem," ASME Trans. J. of Engineering for Power, pp 48-57, Jan. 1978.

5 Childs, D.W., and Moyer, D.S., "Vibration Characteristics of the HPOTP (High-Pressure Oxygen Turbopump) of the SSME (Space Shuttle Main Engine)," ASME Paper No. 84-GT-31, 29th International Gas Turbine Conference and Exhibit, Amsterdam, 1984.

6 Fleming, D.P., "Stiffness of Straight and Tapered Annular Gas Path Seals," ASME Journal of Lubrication Technology, Vol.101, pp. 349-355, July 1979.

7 Fleming, D.P., "Damping in Ring Seals for Compressible Fluids," NASA CP 2133, Rotordynamic Instability Problems in High-Performance Turbomachinery, proceedings of a workshop held at Texas A&M University, 12-14 May 1980, pp. 169-188.

8 Nelson, C.C., "Rotordynamic Coefficients for Compressible Flow in Tapered Annular Seals," ASME Journal of Tribology, Vol. 107, No. 3, July 1985, pp 318-325.

9 Nelson, C.C., "Analysis for Leakage and Rotordynamic Coefficients of Surface-Roughened Tapered Annular Gas Seals," ASME Journal of Engineering for Power, Vol. 106, No. 4, Oct. 1984, pp 927-934.

10 Nelson, C.C., Nguyen, D.T., "Comparison of Hirs' Equation with Moody's Equation for Determining Rotordynamic Coefficients of Annular Pressure Seals," accepted for publication in ASME J. of Tribology.

11 Nelson, C.C., Childs, D.W., "Theory Versus Experiment for the Rotordynamic Coefficients of Annular Gas Seals: Part 2, Constant-Clearance and Convergent-Tapered Geometry," accepted for publication in ASME J. of Tribology.

12 Black, H.F., Allaire, P.E., and Barrett, L.E., "The Effect of Inlet Flow Swirl on the Dynamic Coefficients of High-Pressure Annular Clearance Seals," Ninth International Conference in Fluid Sealing, BHRA Fluid Engineering, Leeuwarden, The Netherlands, Apr. 1981.

13 Childs, D.W., "Finite-Length Solutions for Rotordynamic Coefficients of Turbulent Annular Seals," ASME J. of Lubrication Technology, Vol. 105, pp. 437-444, July 1983.

14 Hirs, G.G., "A Bulk-Flow Theory for Turbulence in Lubricant Films," ASME Journal of Lubrication Technology, Vol. 95, pp. 137-146, April 1973.

15 Massey, B.S., Mechanics of Fluids, 4th Ed., Van Nostrand Reinhold Co., New York, 1979.

16 Elrod, D., Nicks, C., Childs, D.W., and Nelson, C.C., "A Comparison of Experimental and Theoretical Results for Rotordynamic Coefficients of Four Annular Gas Seals," Progress Report for NASA Lewis Research Center Contract NAS8-33716 prepared by Texas A&M University, #TRC-Seals-5-85.

17 von Pragenau, G.L., "Damping Seals for Turbomachinery," NASA Technical Paper 1987, Marshall Space Flight Center, Alabama.

18 Childs, D.W., Nelson, C.C., Nicks, C., Scharrer, J., Elrod, D., Hale, R., "Theory Versus Experiment for the Rotordynamic Coefficients of Annular Gas Seals: Part 1, Test Facility and Apparatus," accepted for publication in ASME J. of Tribology.

19 Scharrer, J.K., "A Comparison of Experimental and Theoretical Results for Rotordynamic Coefficients for Labyrinth Gas Seals," M.S. Thesis, 1985.

20 Iino, T., and Kaneko, H., "Hydraulic Forces Caused by Annular Pressure Seals in Centrifugal Pumps," NASA CP 2133, Rotordynamic Instability Problems in High-Performance Turbomachinery, proceedings of a workshop held at Texas A&M University, 12-14 May 1980.

21 Holman, J.P., Experimental Methods for Engineers, McGraw Hill, New York, 1978, pg. 45.

APPENDIX

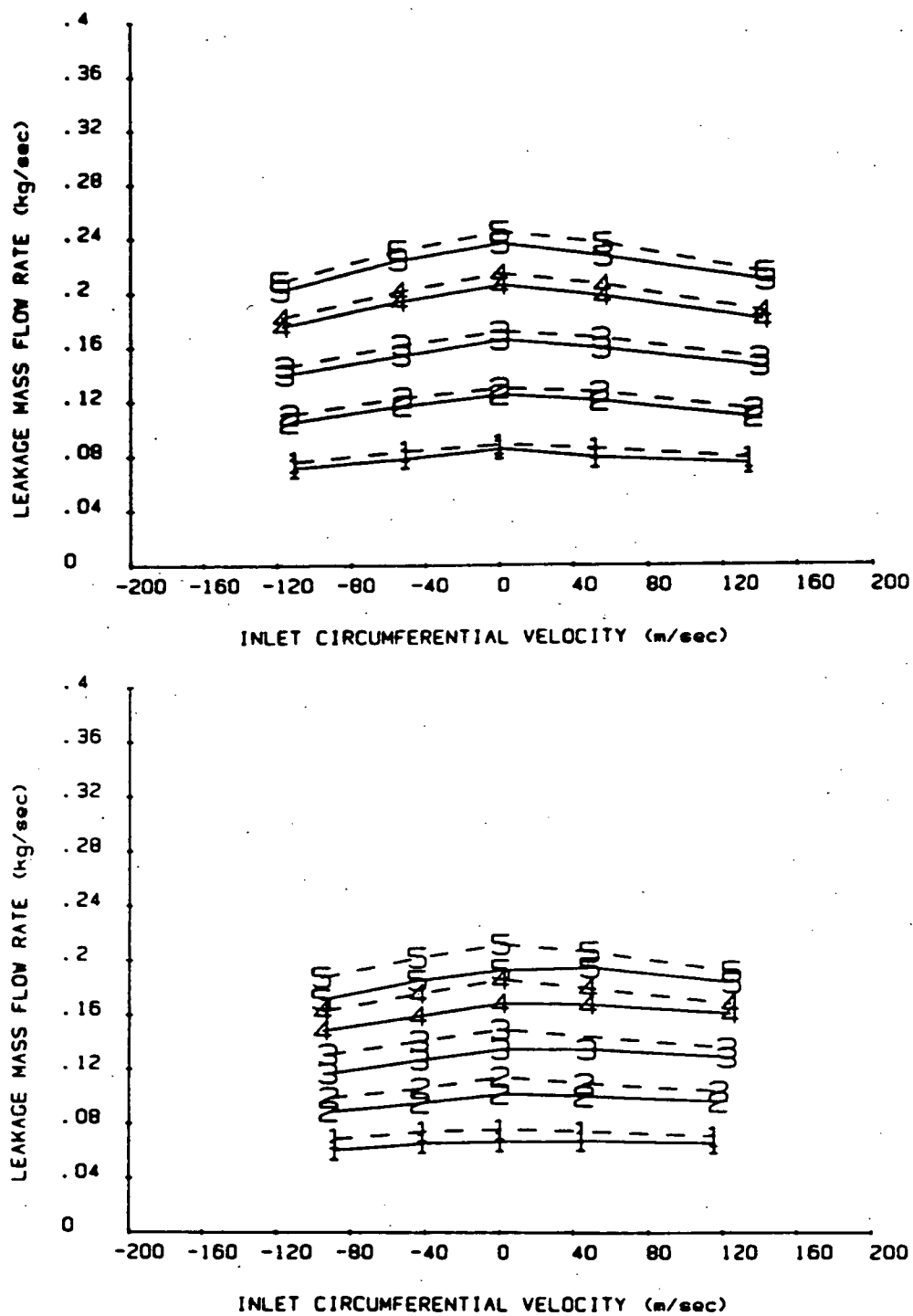


Fig. A1 Mass flow rate of air through seal 1.0 at 3000 rpm (above) and 16000 rpm (below). See Table 4 for pressure symbol definitions.

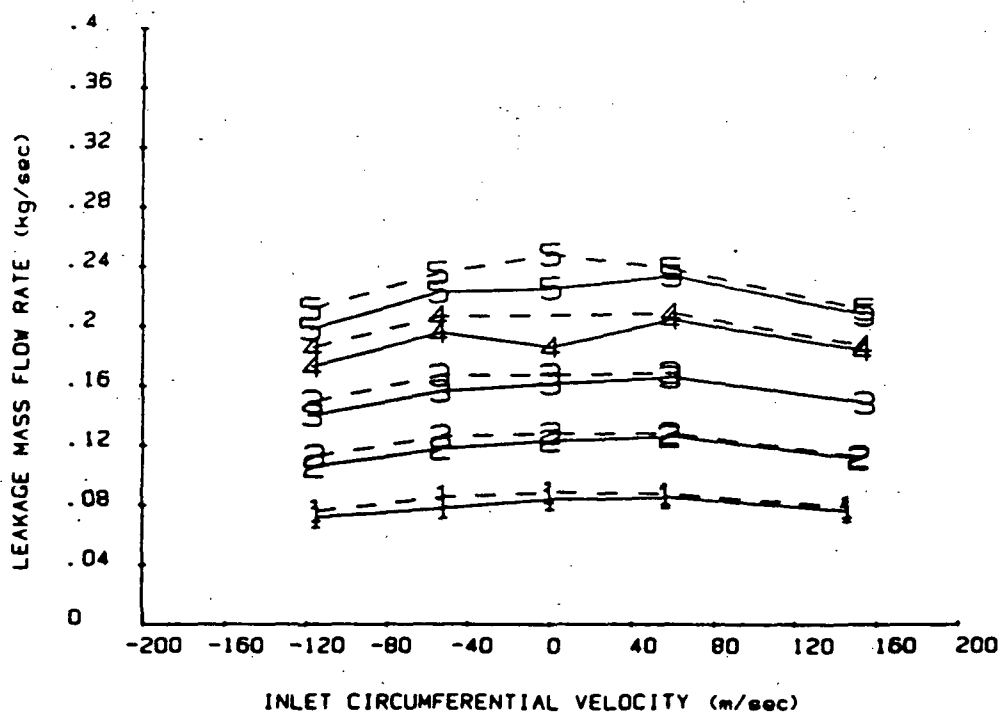
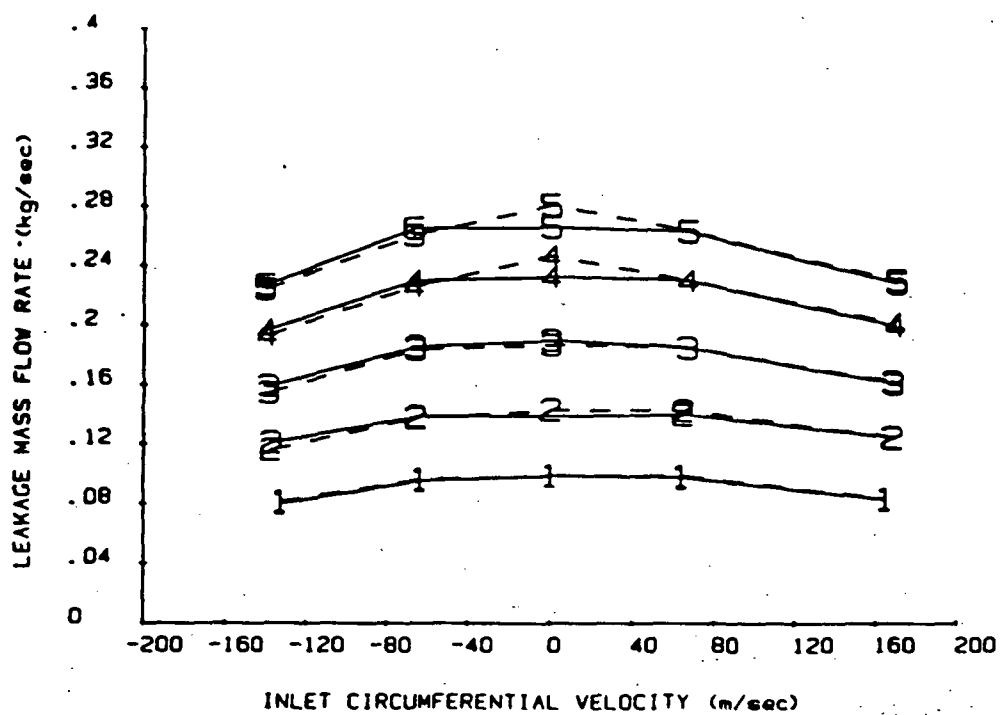


Fig. A2 Mass flow rate of air through seal 1.5 at 3000 rpm (above) and 16000 rpm (below). See Table 4 for pressure symbol definitions.

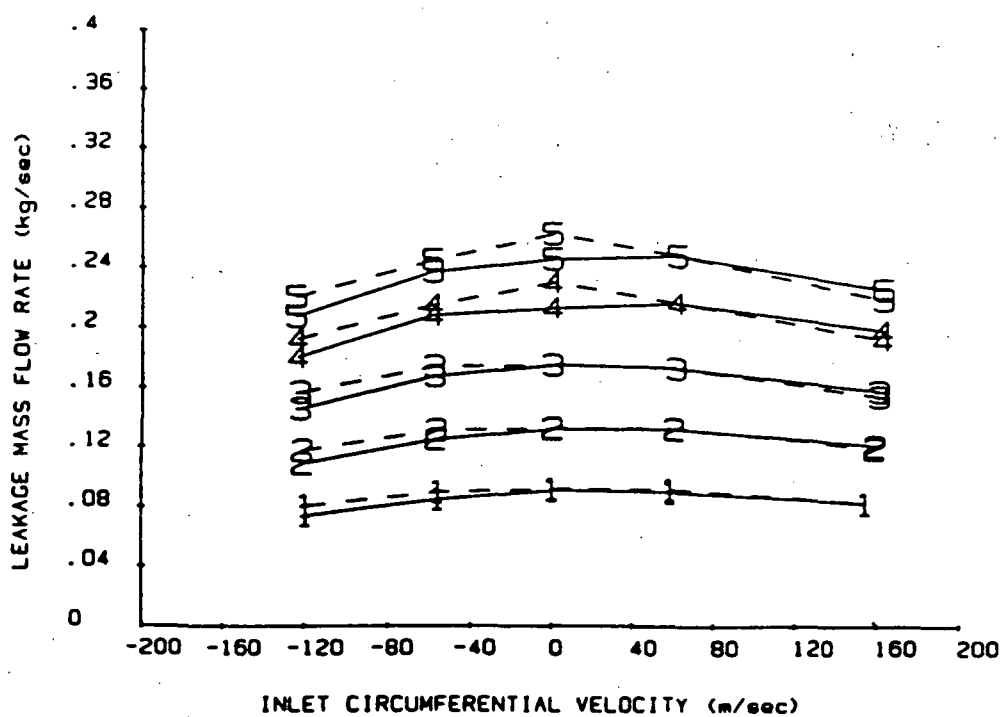
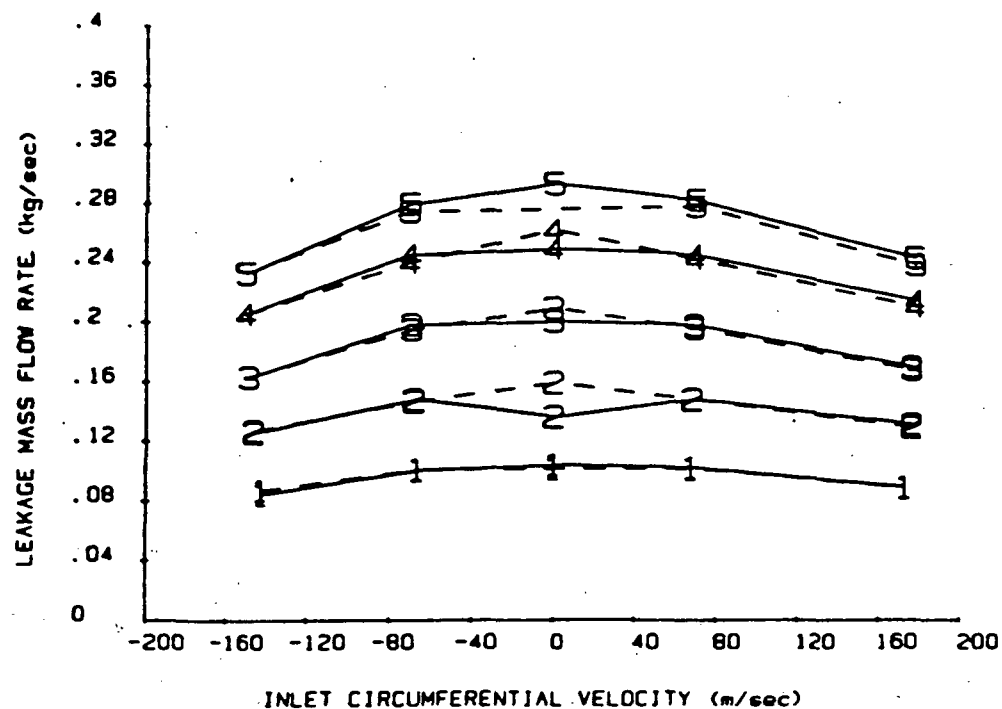


Fig. A3 Mass flow rate of air through seal 2.0 at 3000 rpm (above) and 16000 rpm (below). See Table 4 for pressure symbol definitions.

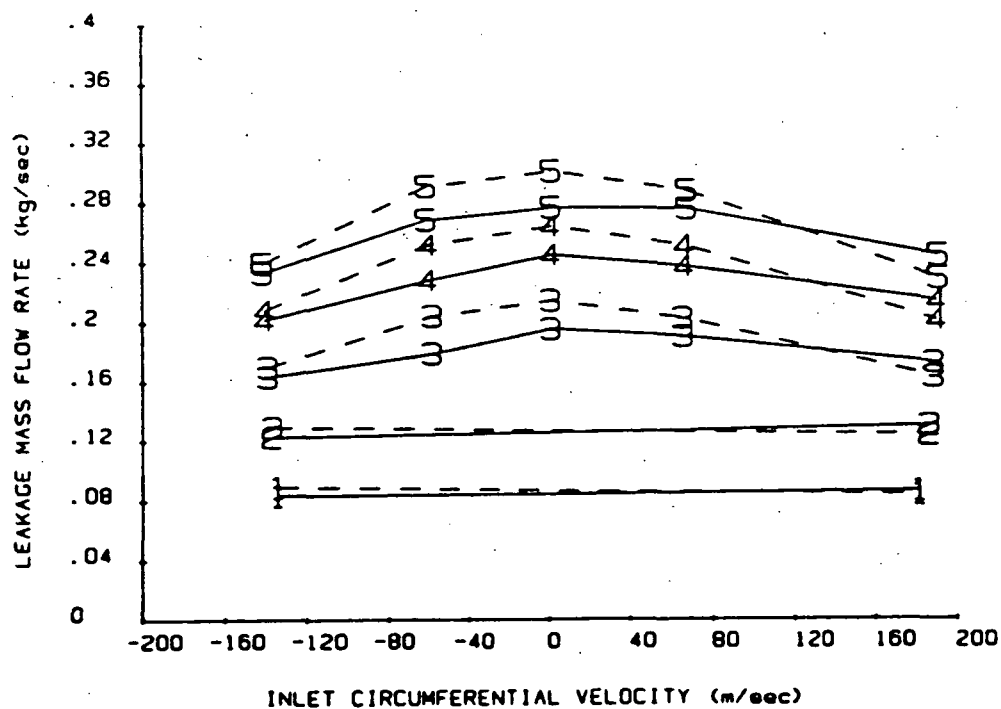
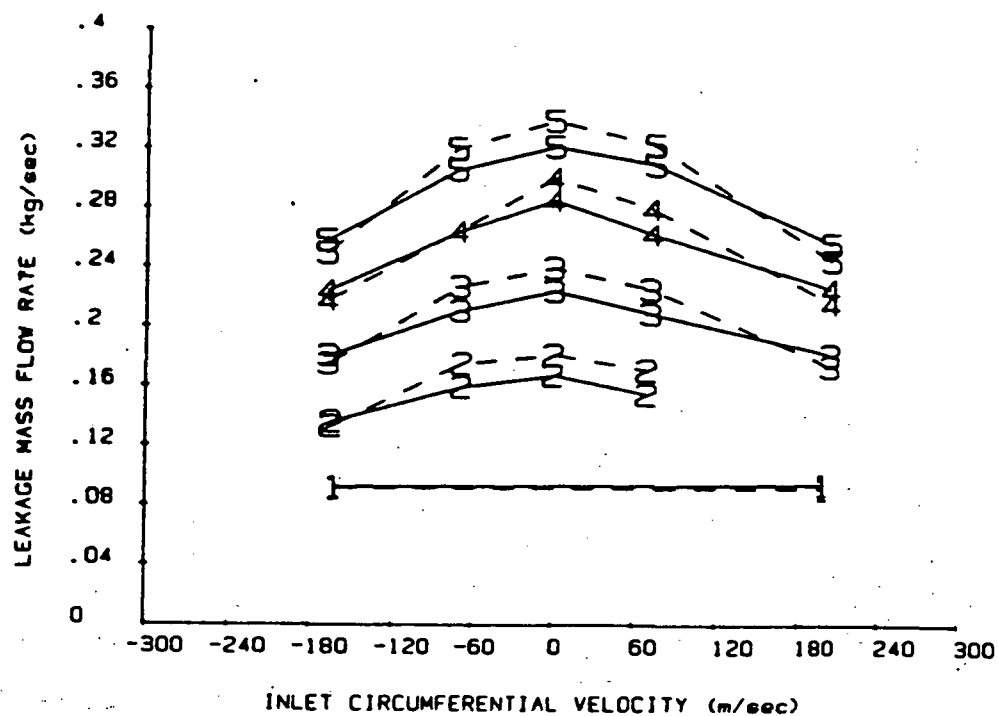


Fig. A4 Mass flow rate of air through seal 2.5 at 3000 rpm (above) and 16000 rpm (below). See Table 4 for pressure symbol definitions.

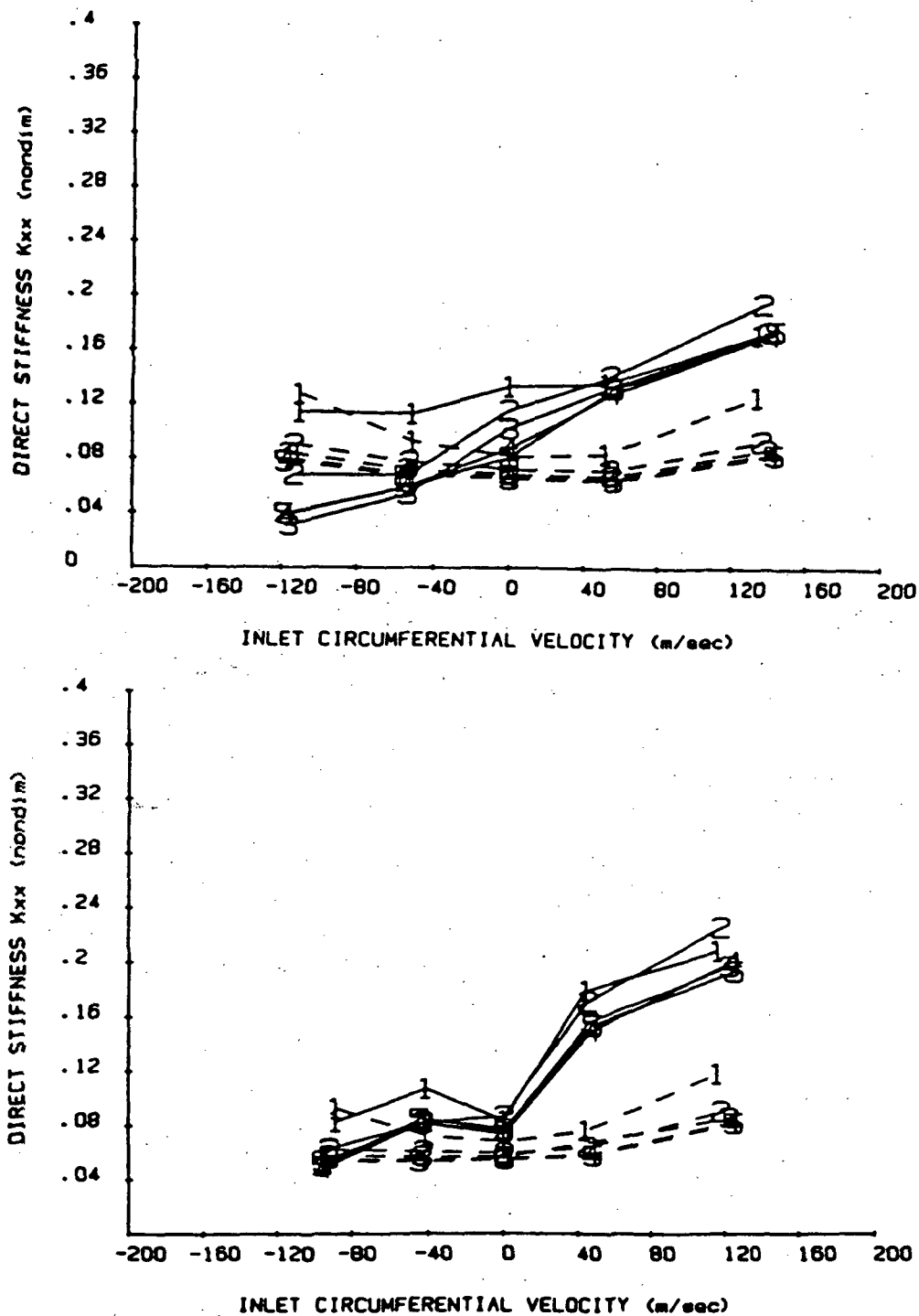


Fig. A5 Normalized direct stiffness of seal 1.0 at 3000 rpm (above) and 16000 rpm (below). See Table 4 for pressure symbol definitions.

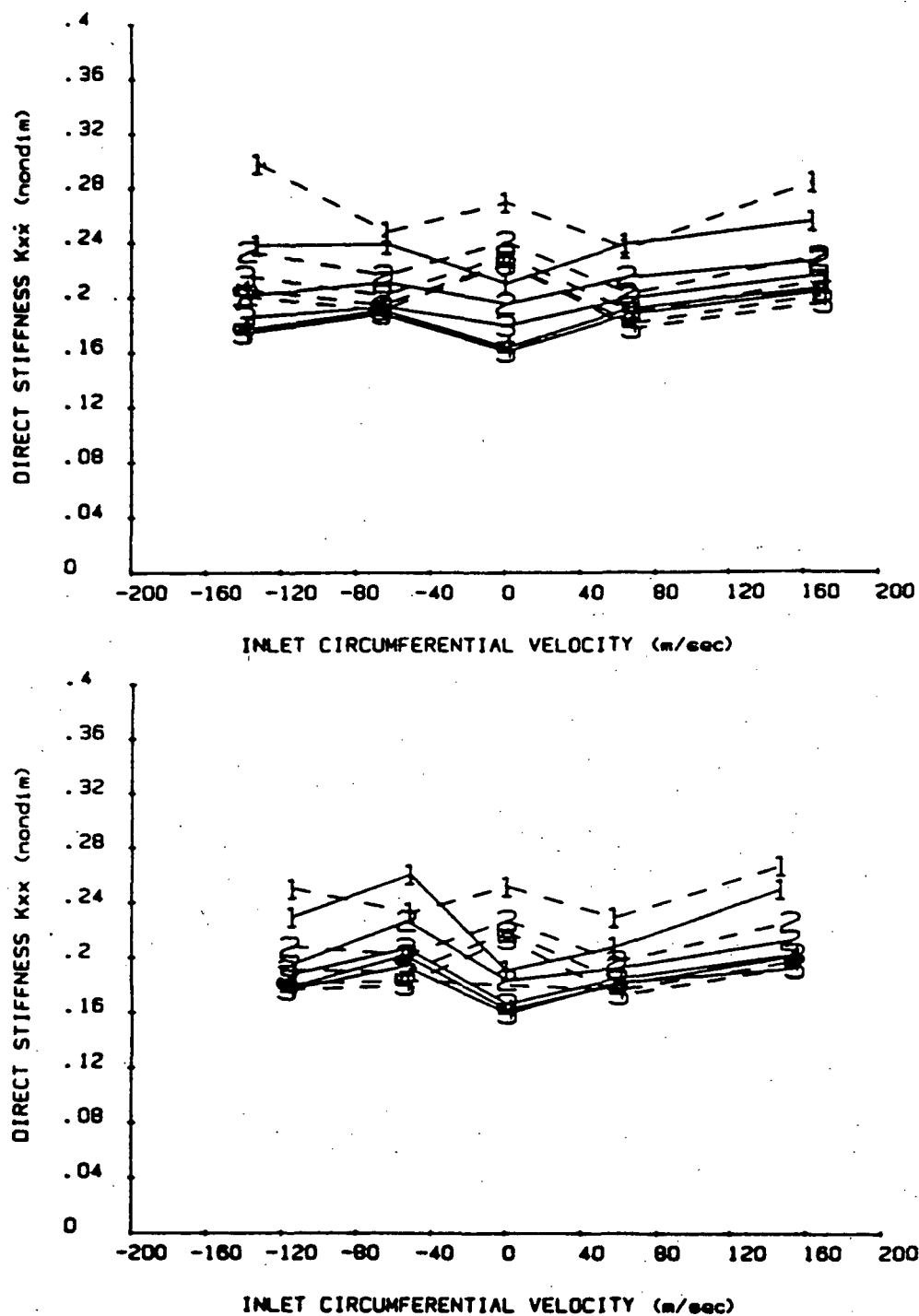


Fig. A6 Normalized direct stiffness of seal 1.5 at 3000 rpm (above) and 16000 rpm (below). See Table 4 for pressure symbol definitions.

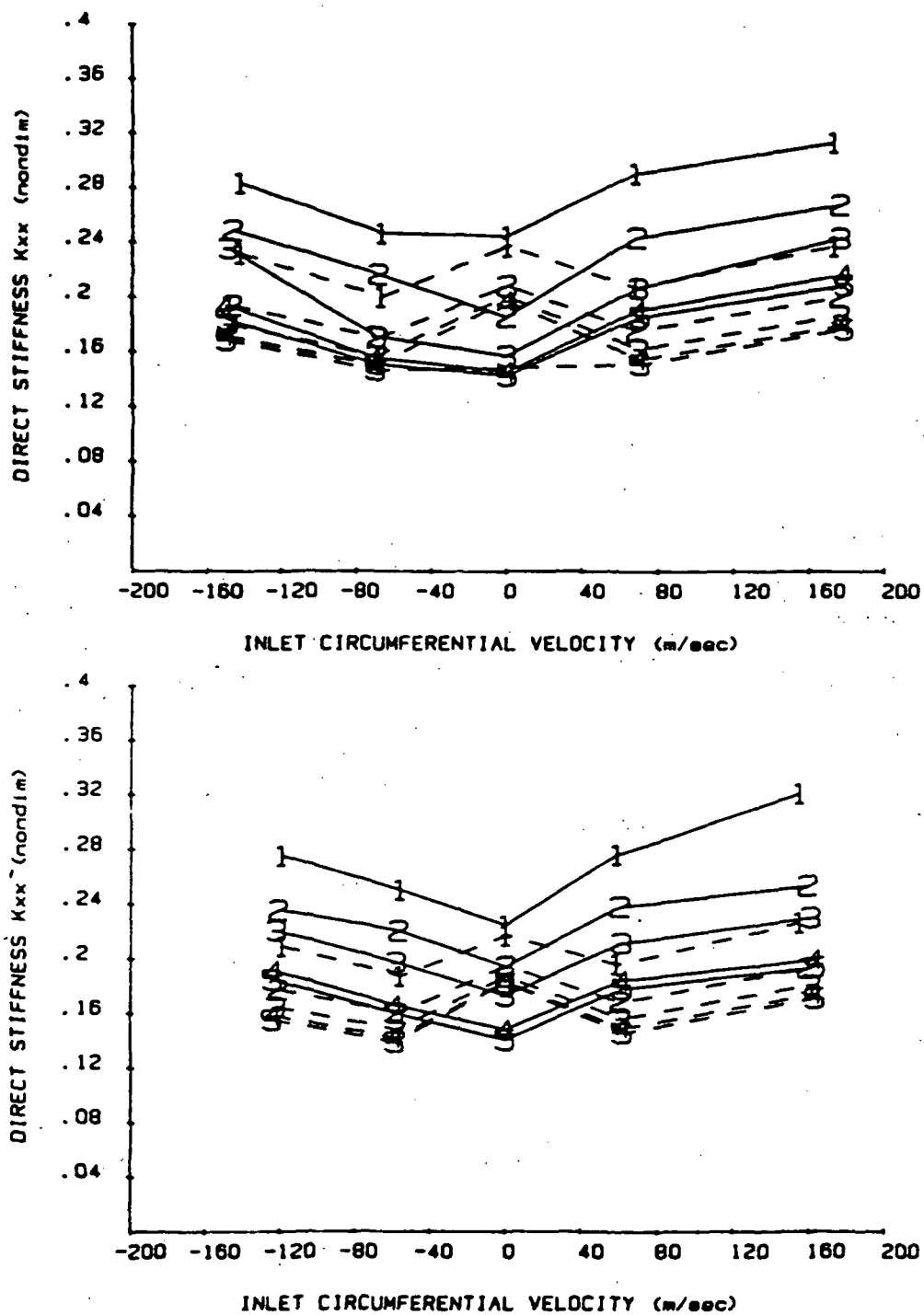


Fig. A7 Normalized direct stiffness of seal 2.0 at 3000 rpm (above) and 16000 rpm (below). See Table 4 for pressure symbol definitions.

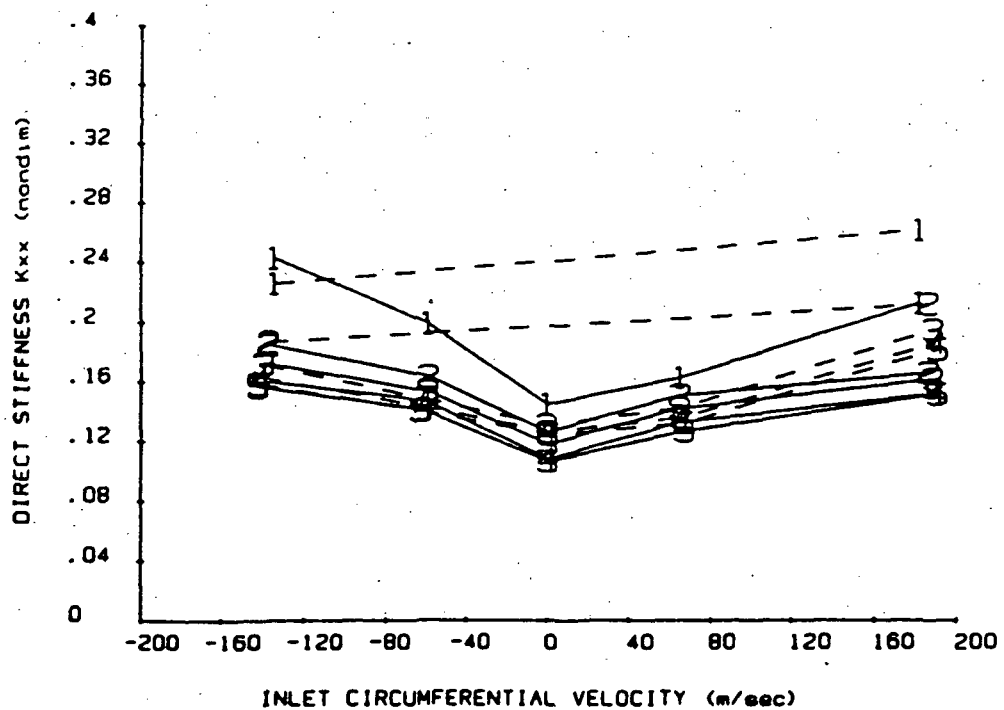
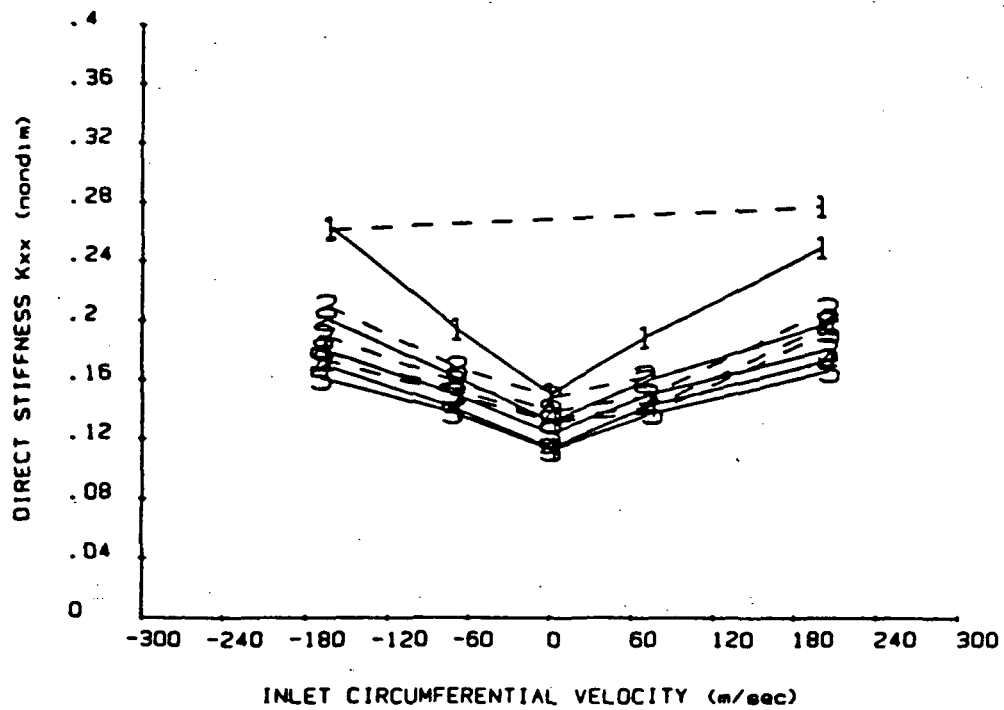


Fig. A8 Normalized direct stiffness of seal 2.5 at 3000 rpm (above) and 16000 rpm (below). See Table 4 for pressure symbol definitions.

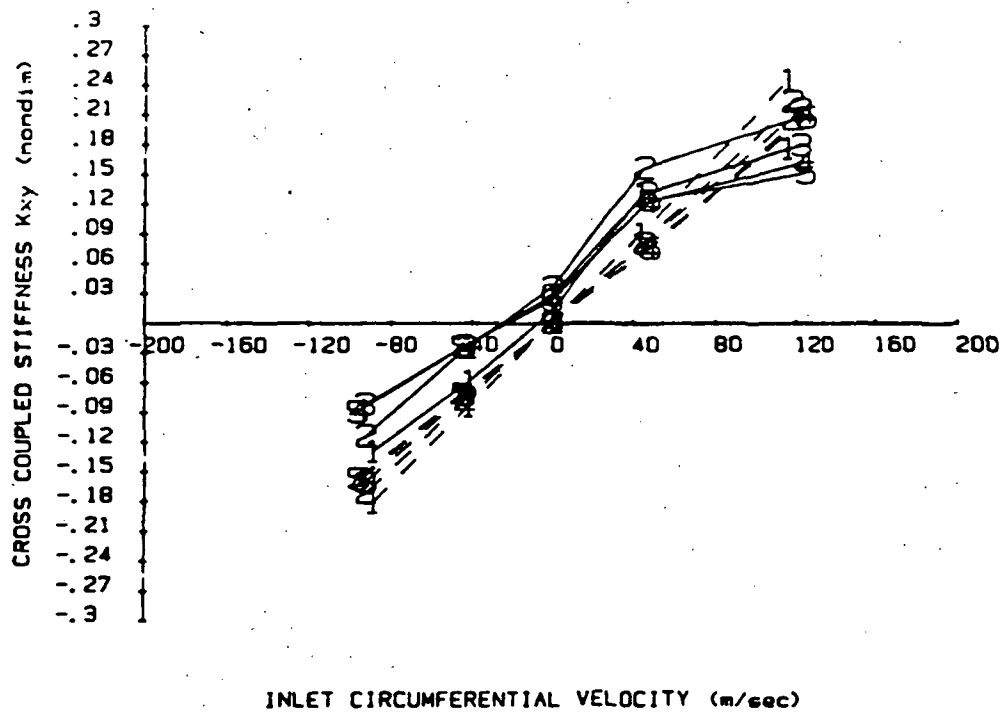
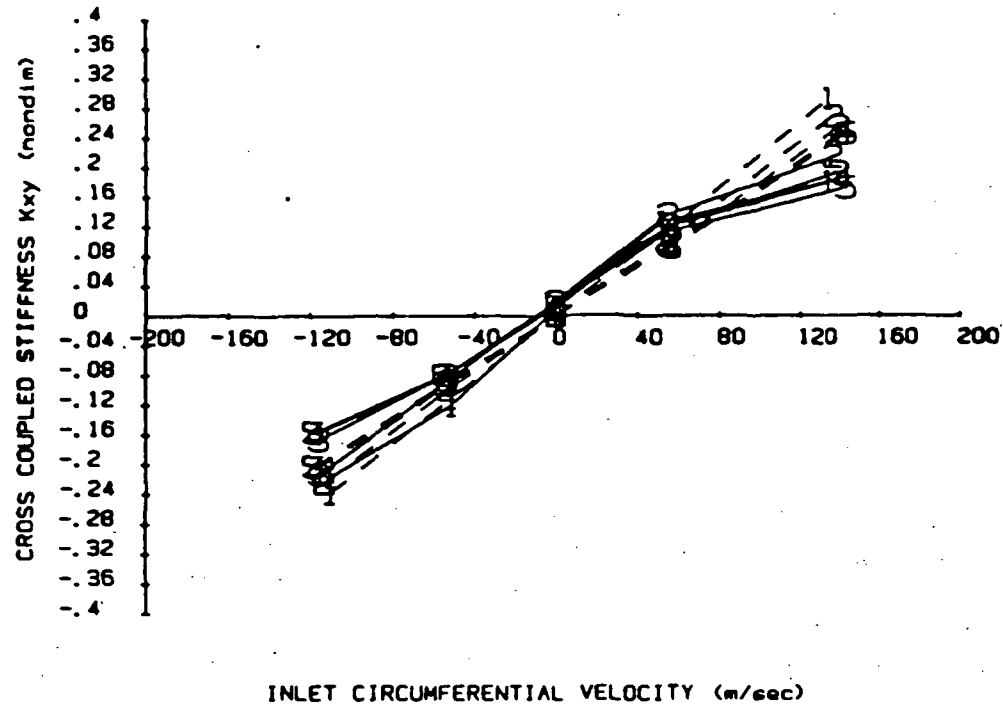


Fig. A9 Normalized cross-coupled stiffness of seal 1.0 at 3000 rpm (above) and 16000 rpm (below). See Table 4 for pressure symbol definitions.

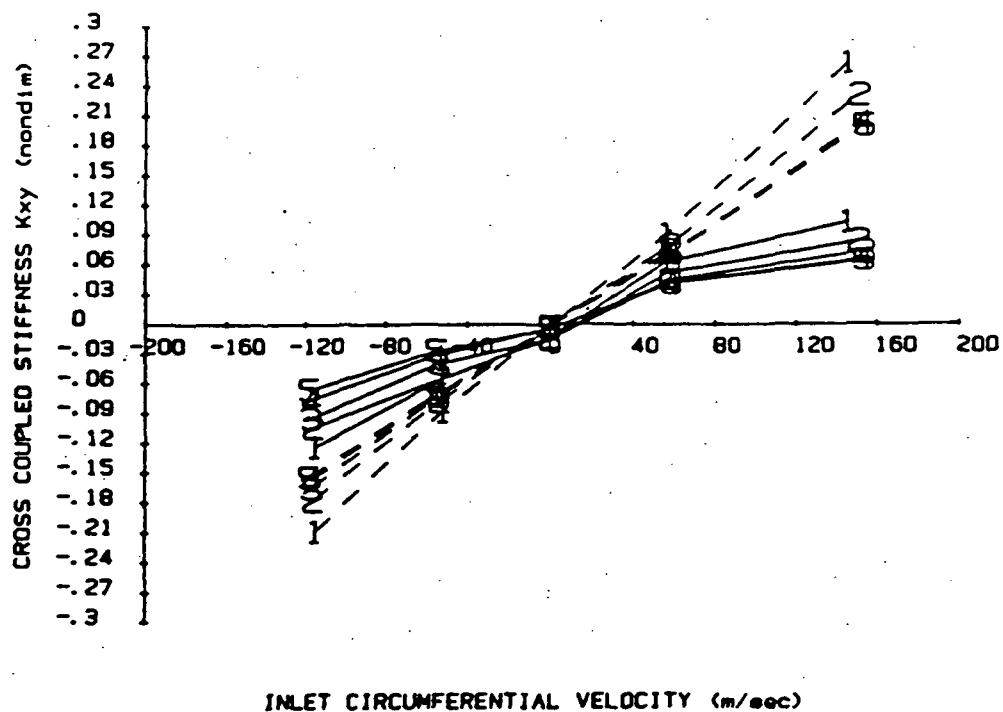
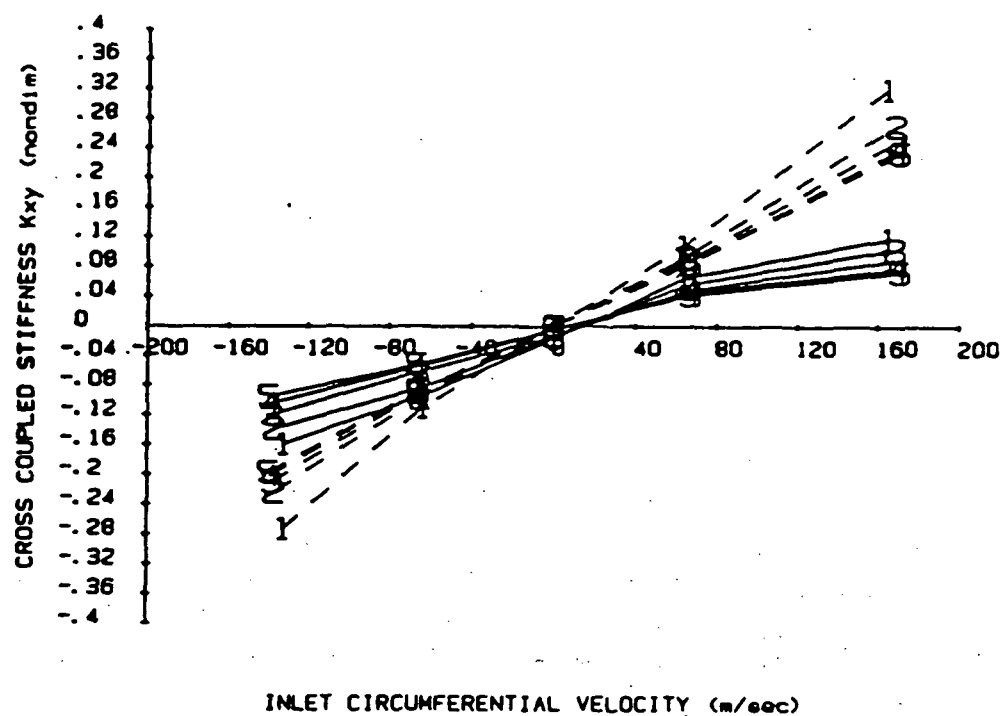


Fig. A10 Normalized cross-coupled stiffness of seal 1.5 at 3000 rpm (above) and 16000 rpm (below). See Table 4 for pressure symbol definitions.

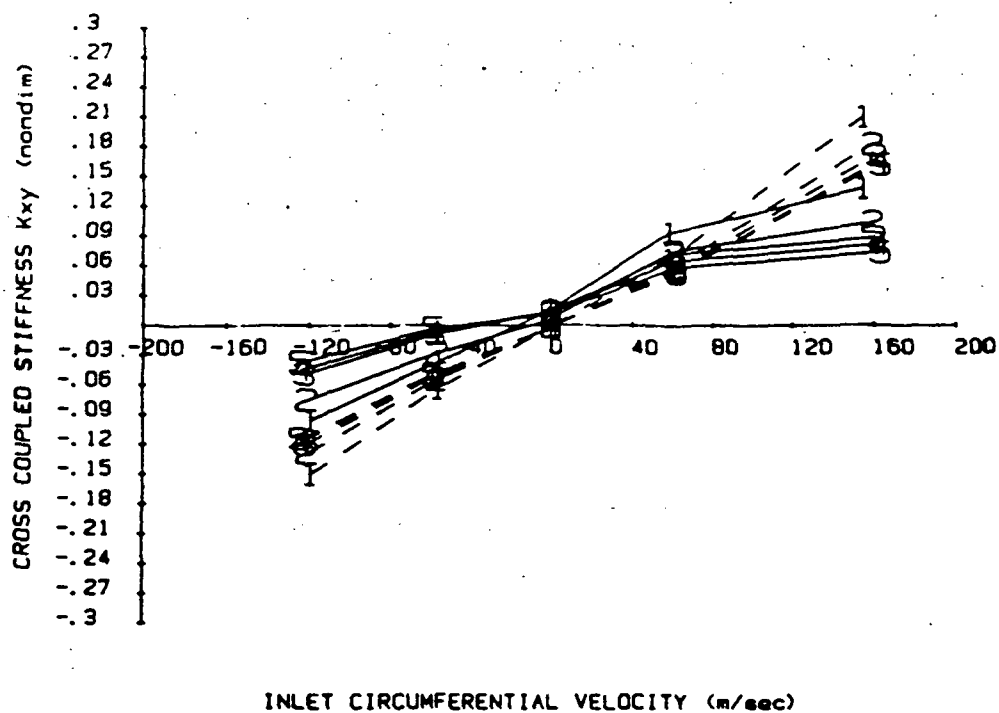
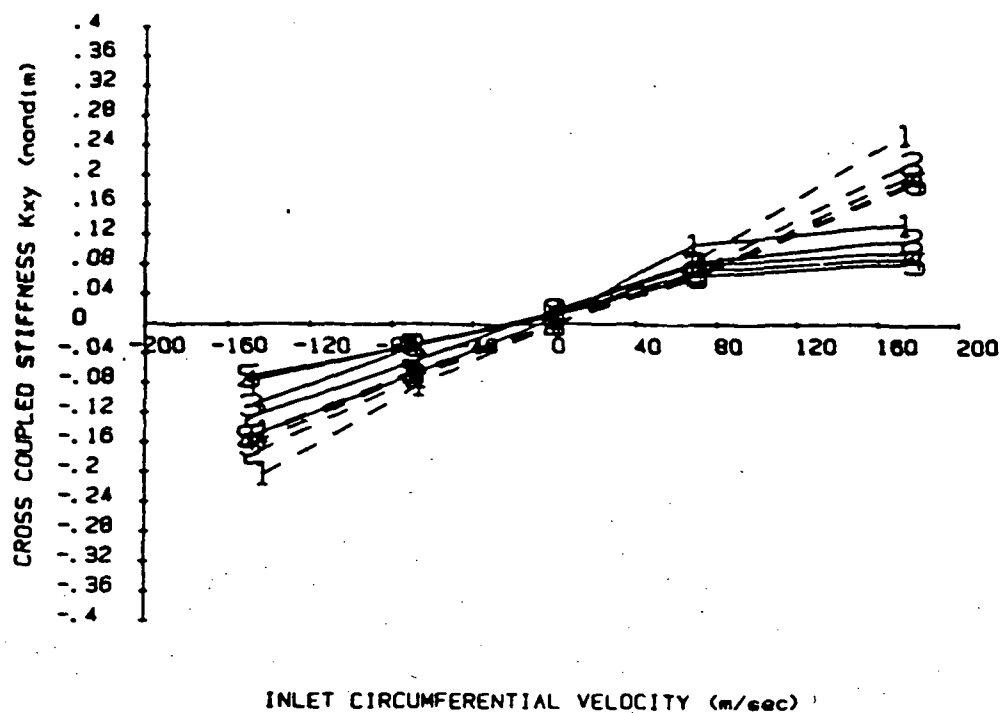
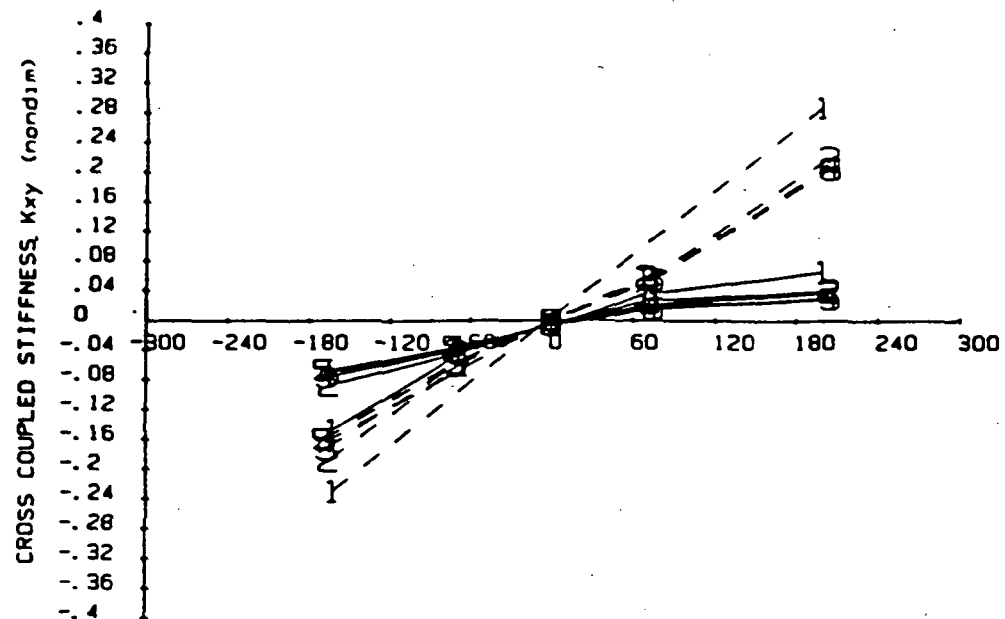
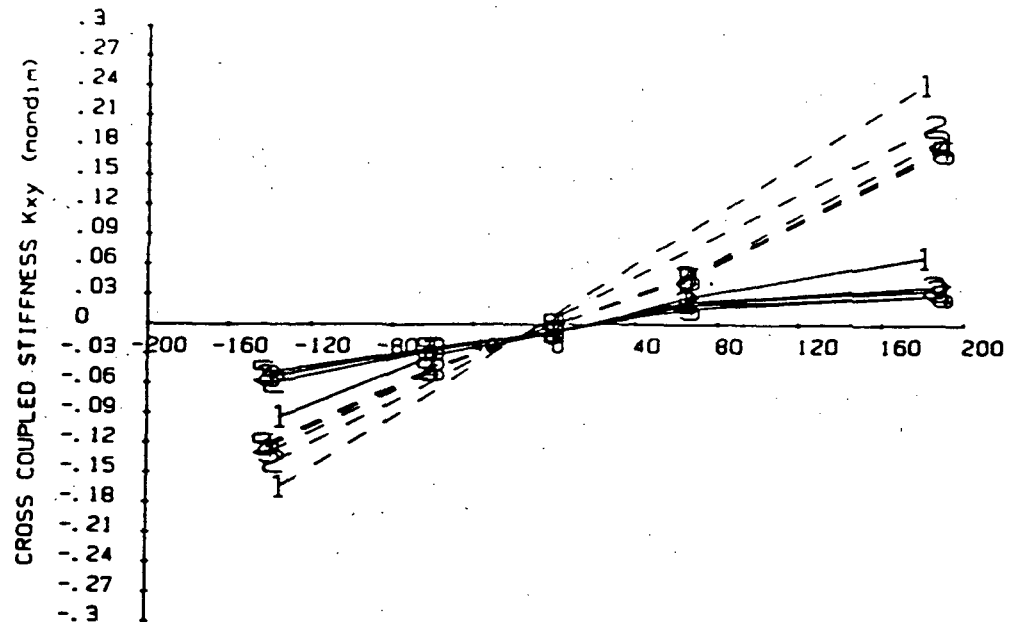


Fig. A11 Normalized cross-coupled stiffness of seal 2.0 at 3000 rpm (above) and 16000 rpm (below). See Table 4 for pressure symbol definitions.



INLET CIRCUMFERENTIAL VELOCITY (m/sec)



INLET CIRCUMFERENTIAL VELOCITY (m/sec)

Fig. A12 Normalized cross-coupled stiffness of seal 2.5 at 3000 rpm (above) and 16000 rpm (below). See Table 4 for pressure symbol definitions.

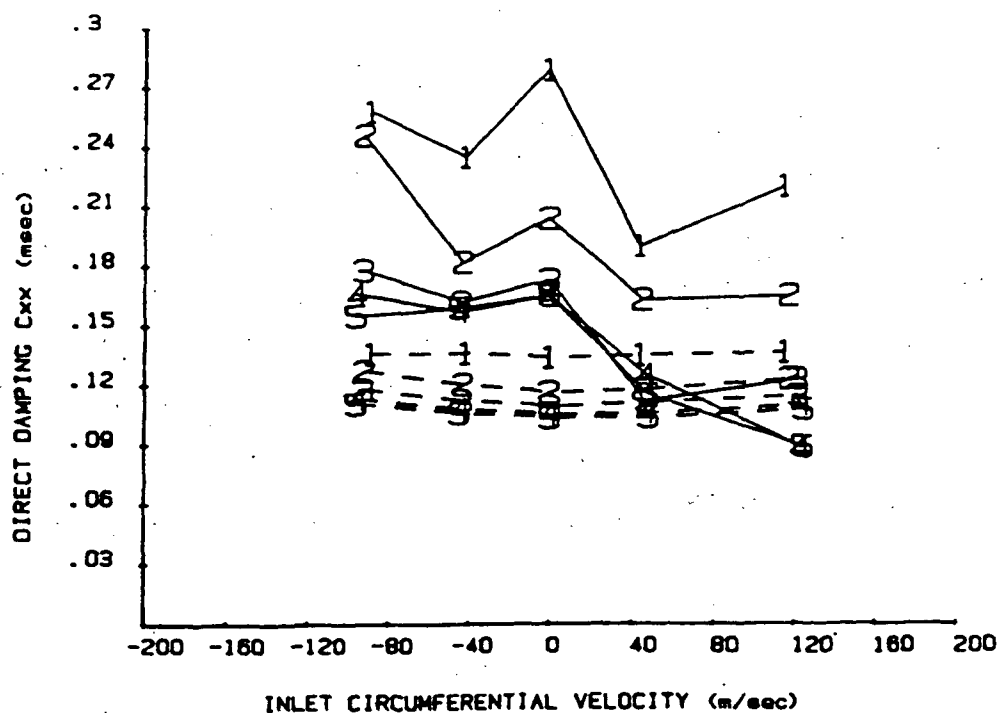
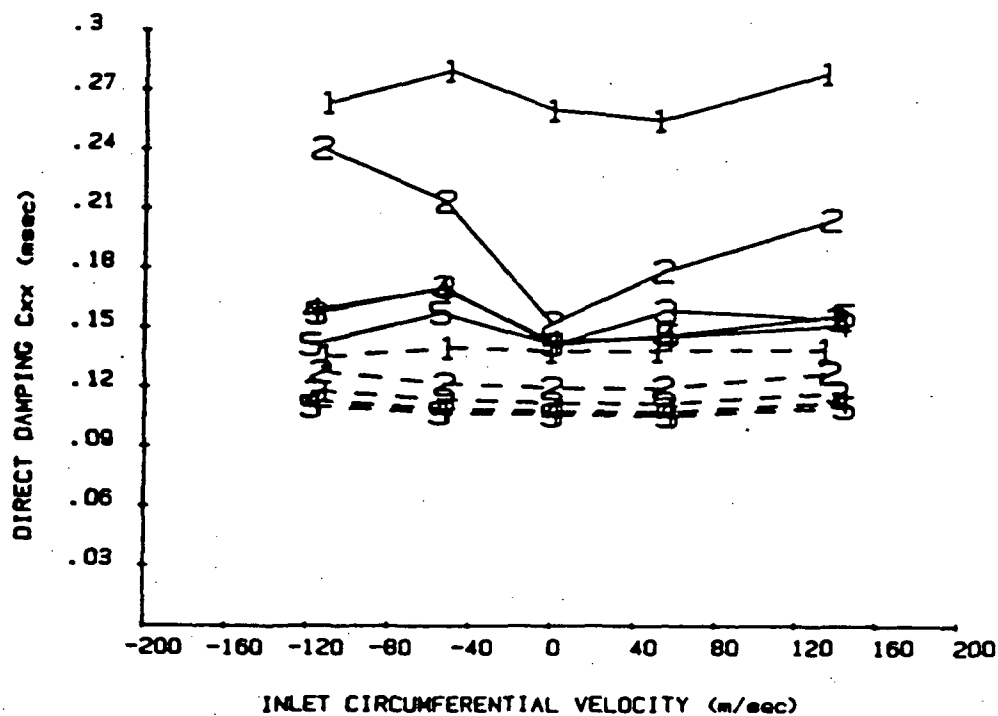


Fig. A13 Normalized direct damping of seal 1.0 at 3000 rpm (above) and 16000 rpm (below). See Table 4 for pressure symbol definitions.

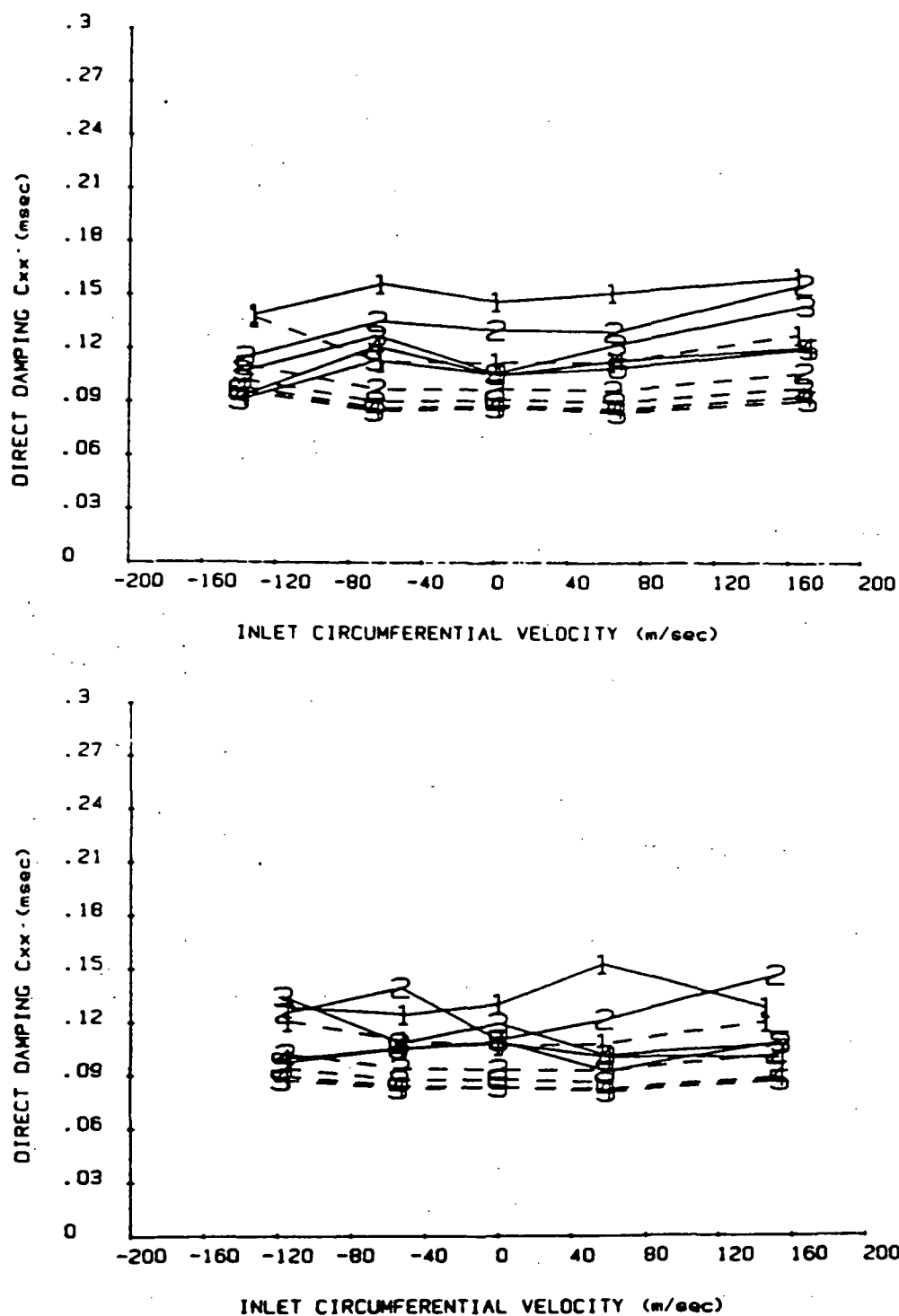


Fig. A14 Normalized direct damping of seal 1.5 at 3000 rpm (above) and 16000 rpm (below). See Table 4 for pressure symbol definitions.

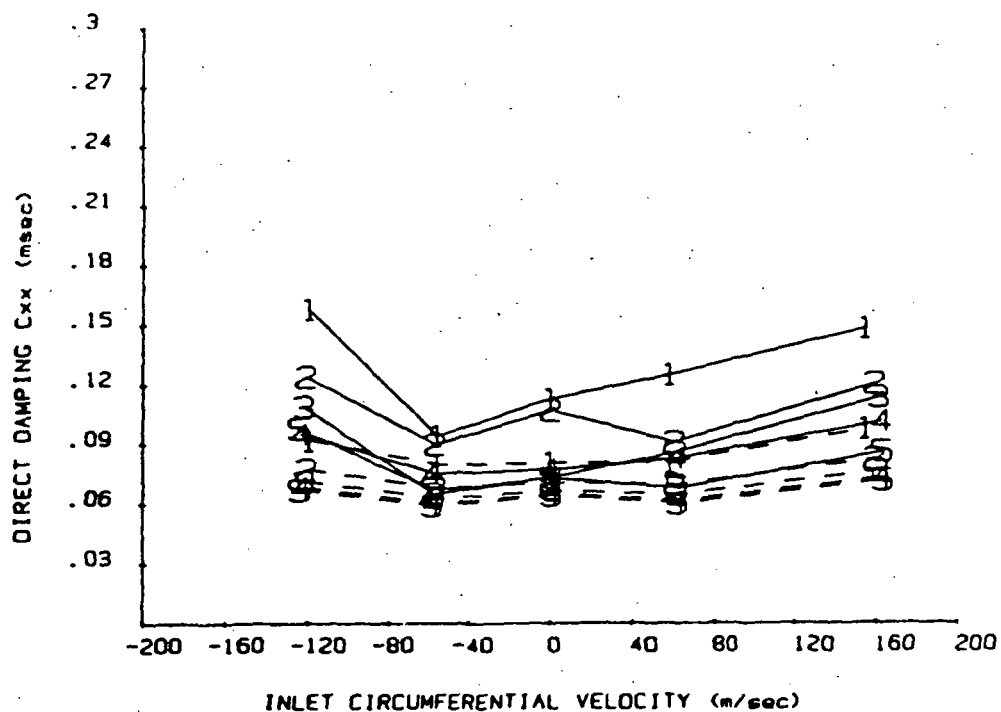
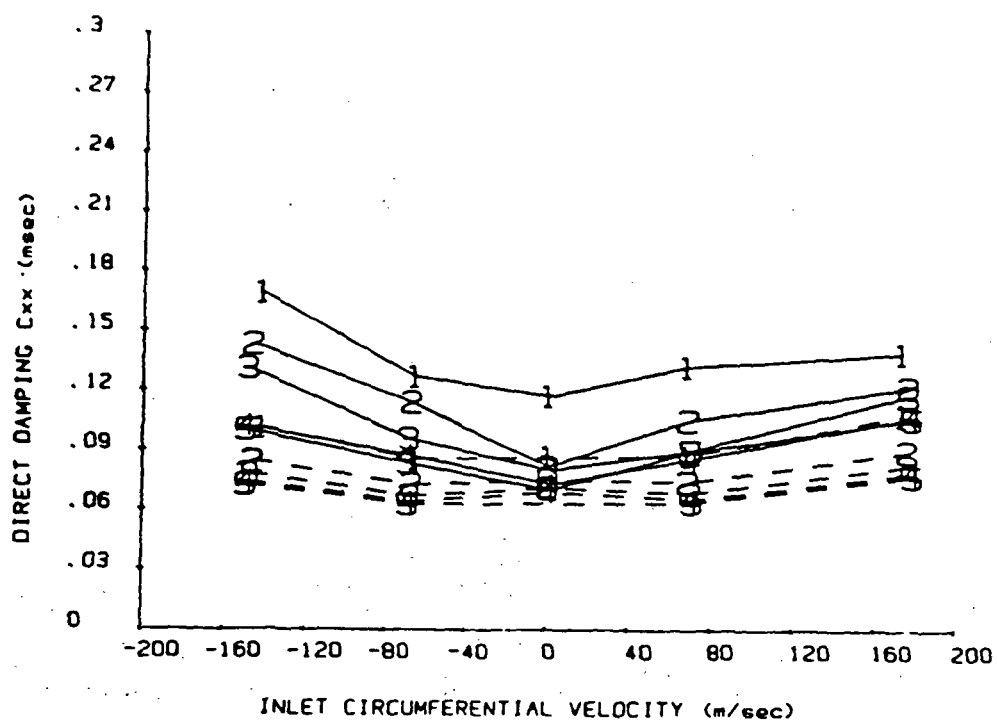


Fig. A15 Normalized direct damping of seal 2.0 at 3000 rpm (above) and 16000 rpm (below). See Table 4 for pressure symbol definitions.

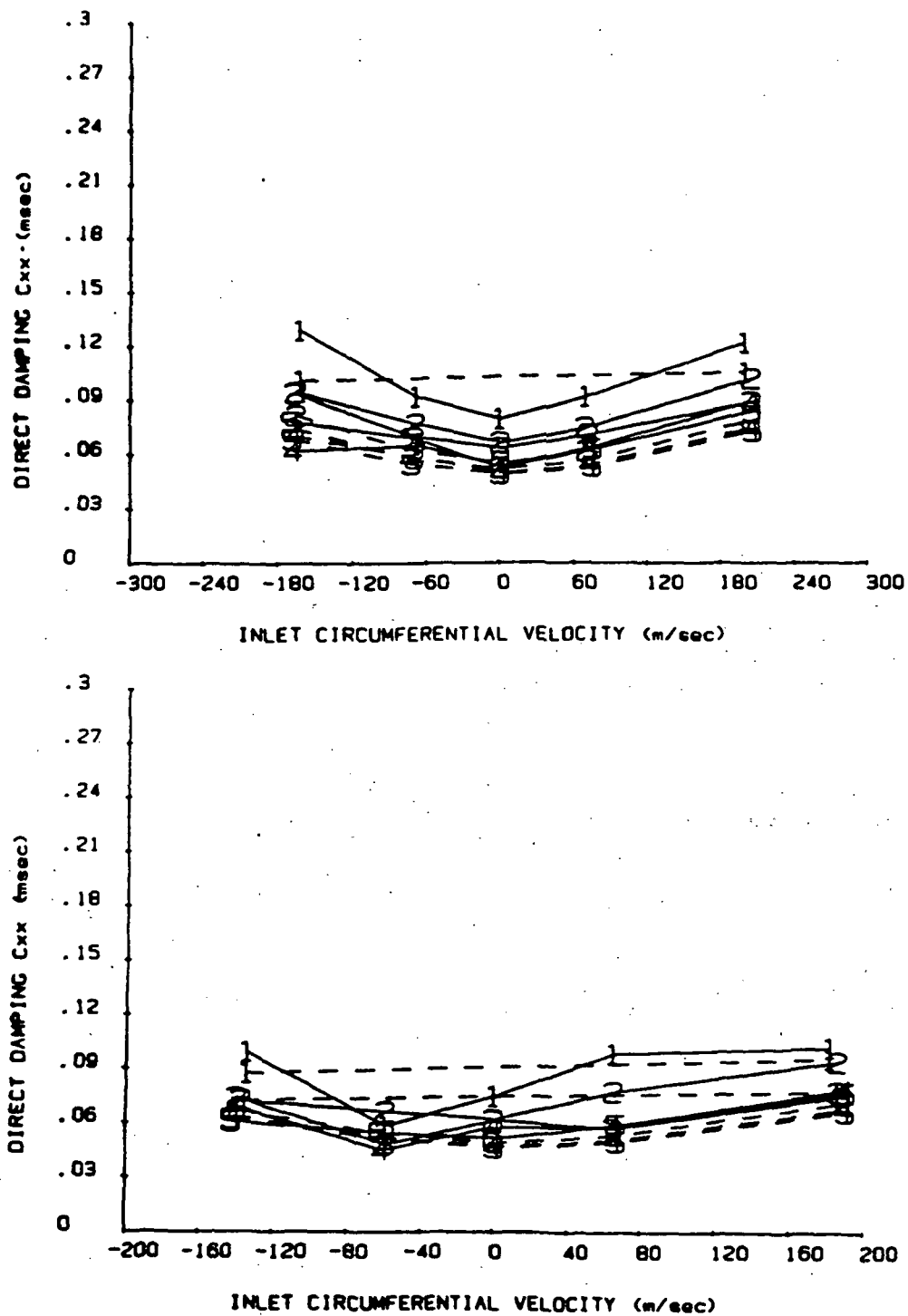


Fig. A16 Normalized direct damping of seal 2.5 at 3000 rpm (above) and 16000 rpm (below). See Table 4 for pressure symbol definitions.

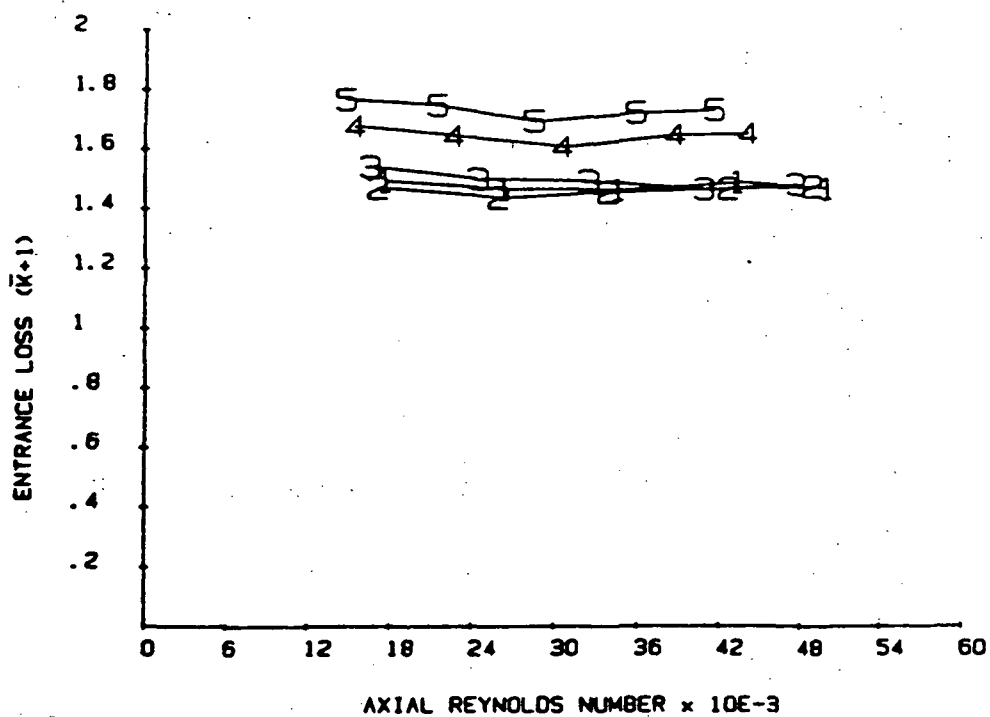
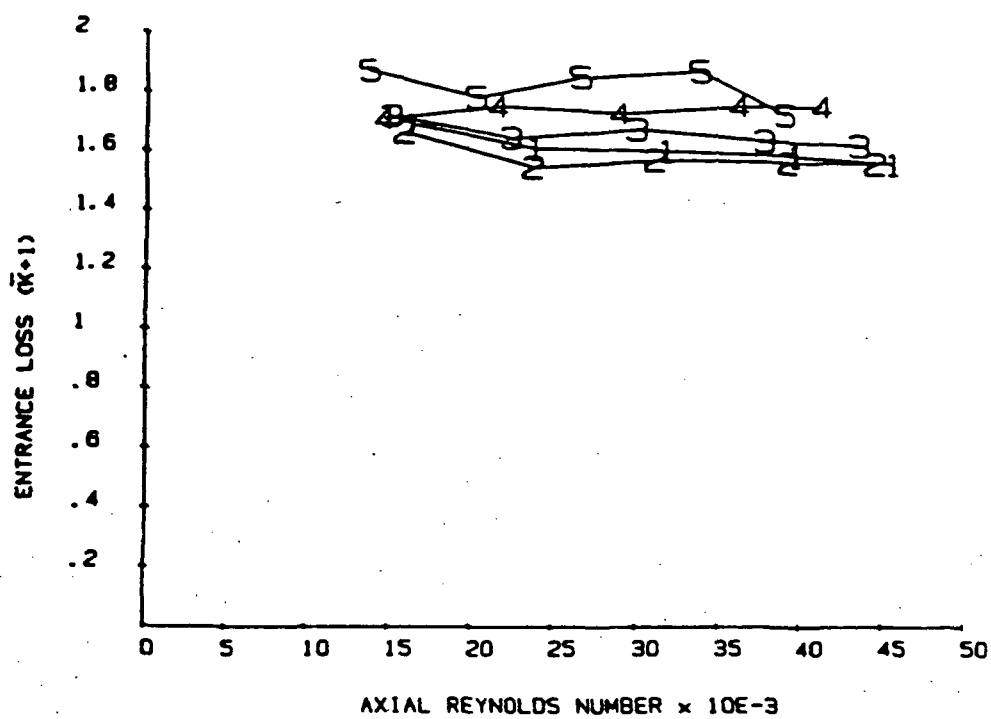


Fig. A17 Entrance loss of seal 1.0, inlet air swirls 1 (top) and 2 (bottom) from Table 4. Curves are numbered by rotor speeds listed in Table 4.

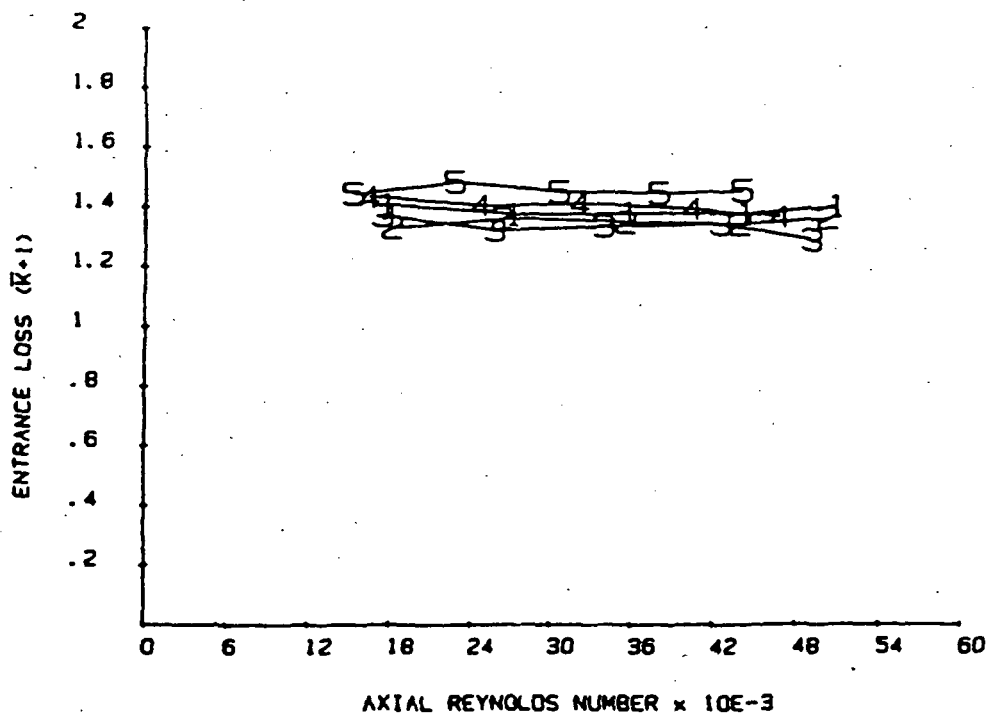
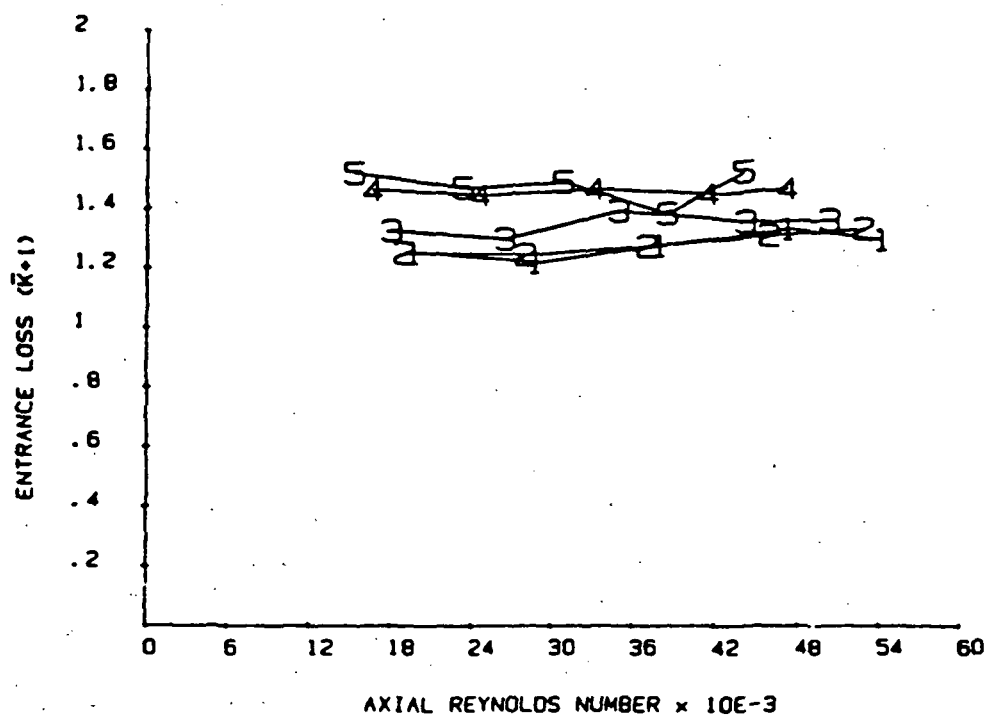


Fig. A18 Entrance losses of seal 1.0, inlet air swirl 3 (top) and 4 (bottom) of Table 4. Curves are numbered by rotor speeds of Table 4.

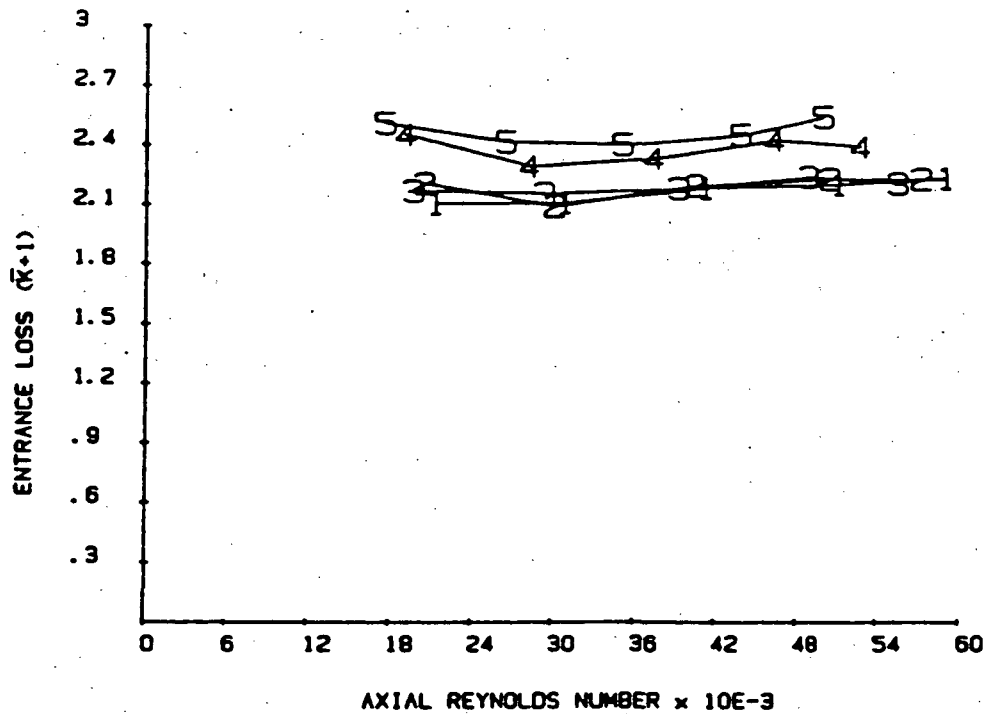
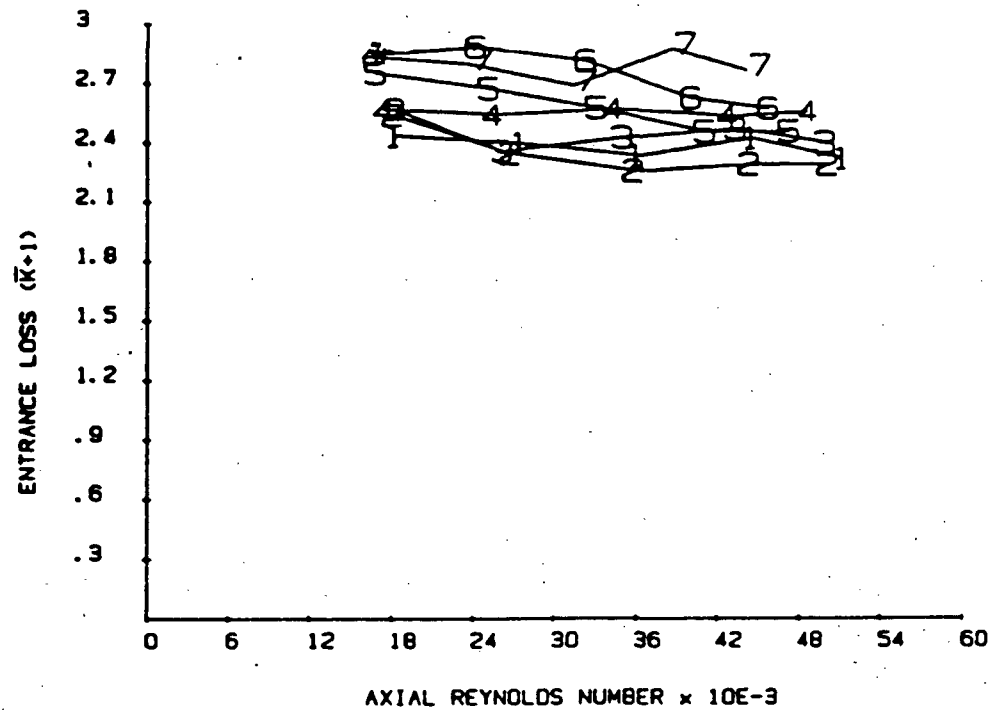


Fig. A19 Entrance losses of seal 1.5, inlet air swirl 1 (top) and 2 (bottom) of Table 4. Curves are numbered by rotor speeds of Table 4.

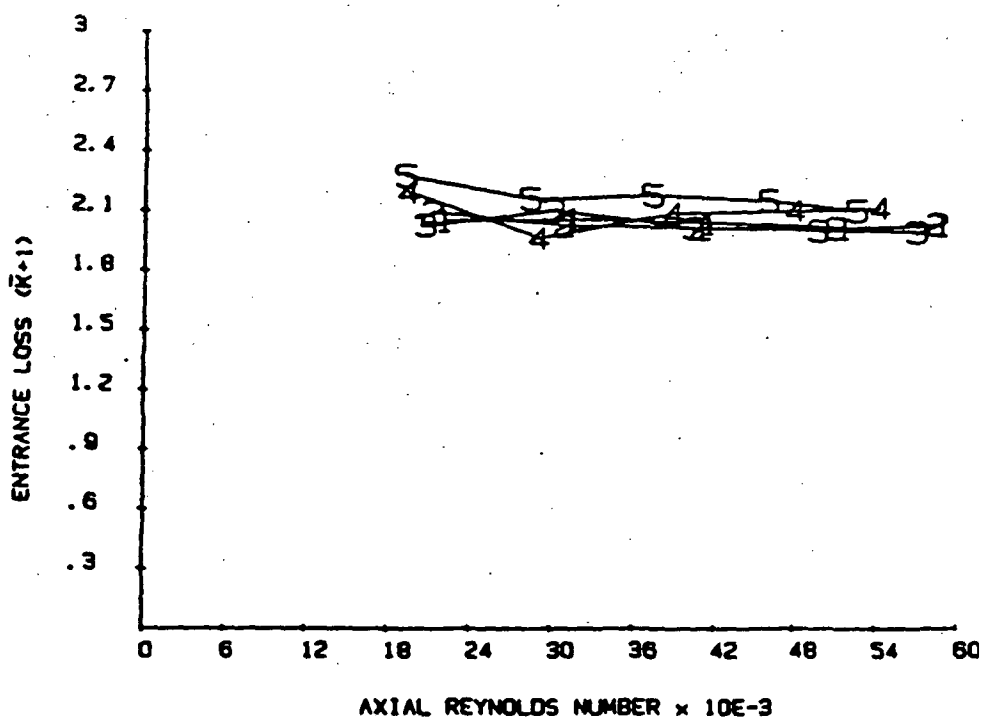
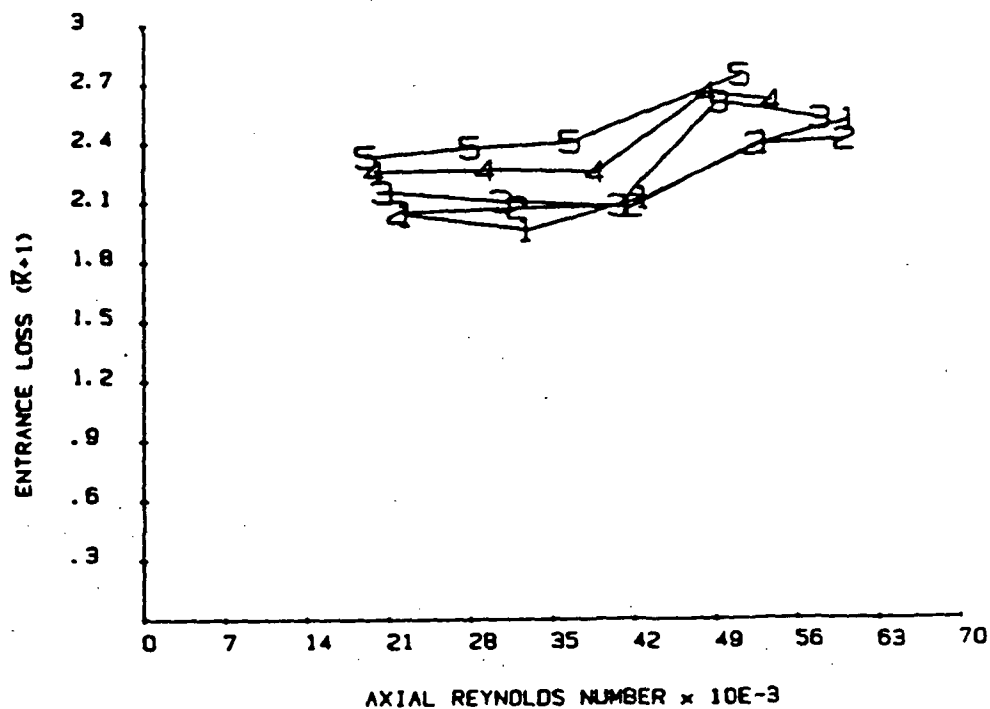


Fig. A20 Entrance losses of seal 1.5, inlet air swirls 3 (top) and 4 (bottom) of Table 4. Curves are numbered by rotor speeds of Table 4.

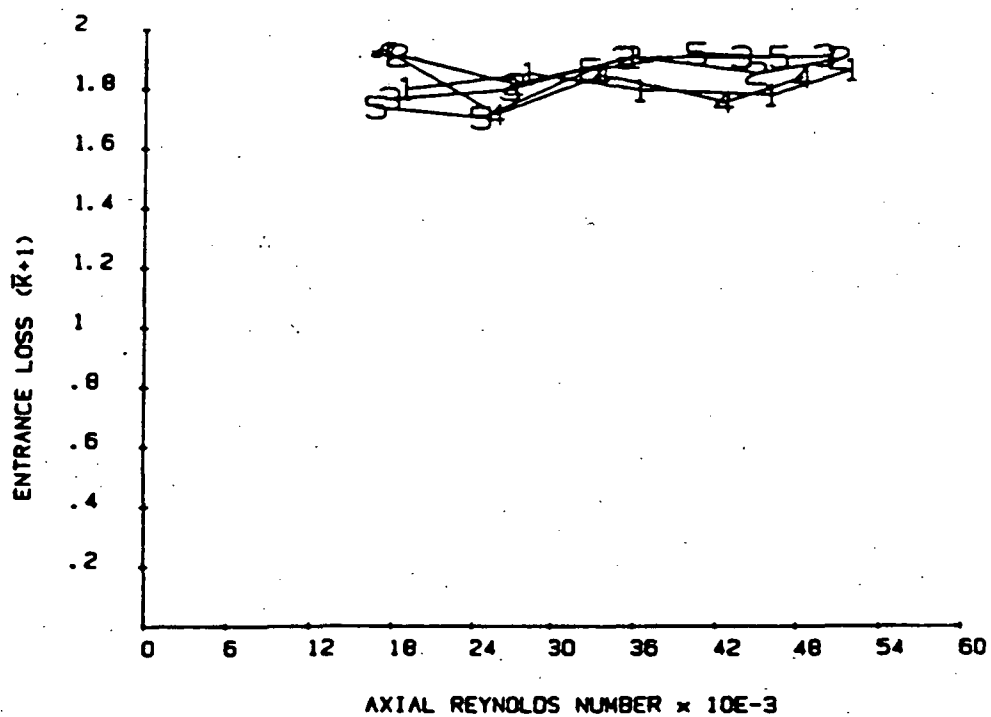
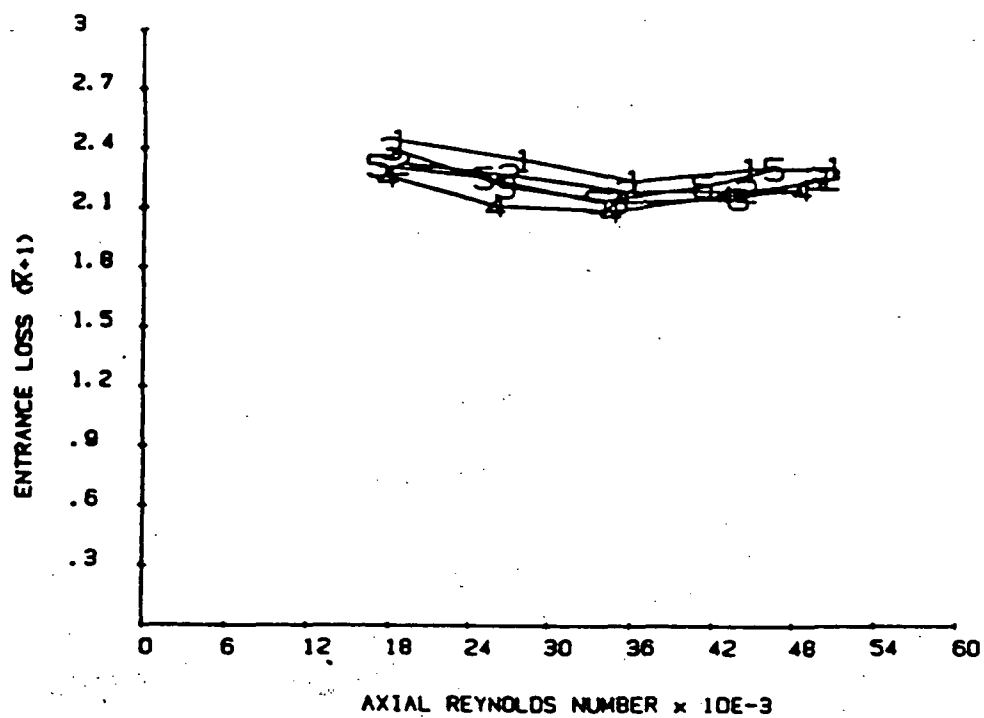


Fig. A21 Entrance losses of seal 1.5 inlet air swirl 5 (top) and seal 2.0 inlet air swirl 1 (bottom). Curves numbered by rotor speeds of Table 4.

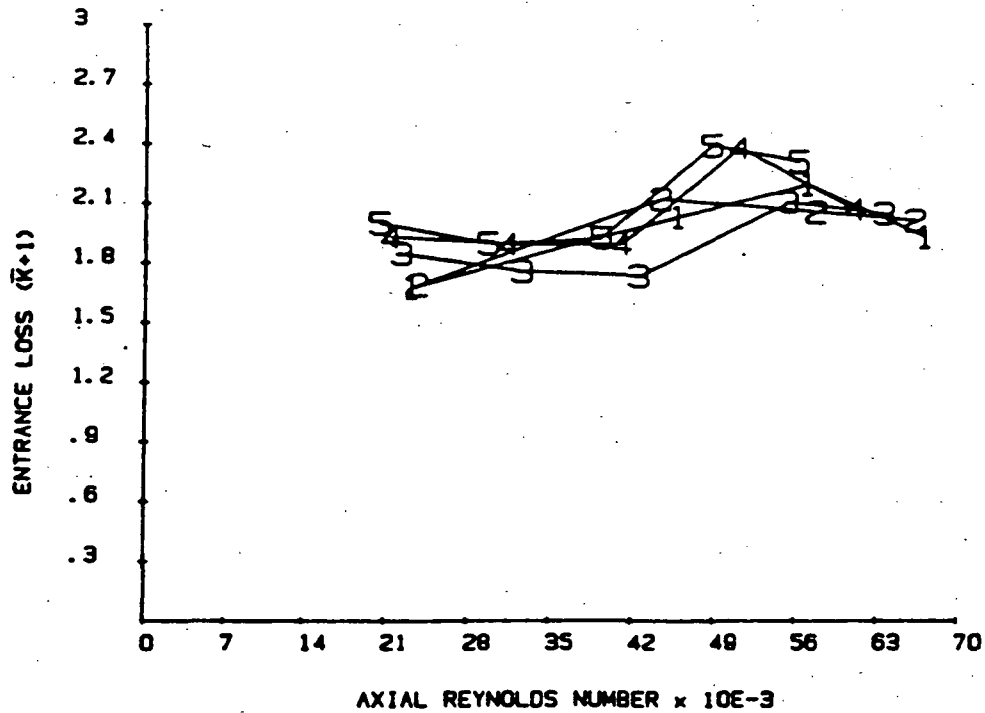
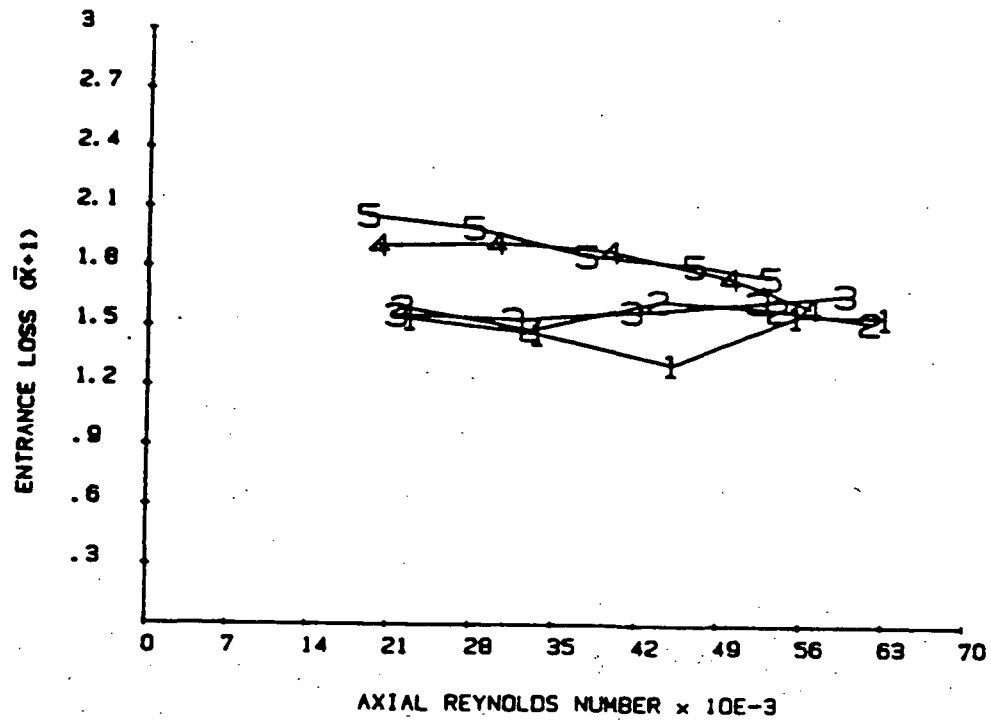


Fig. A22 Entrance losses of seal 2.0, inlet air swirls 2 (top) and 3 (bottom). Curves numbered by rotor speeds of Table 4.

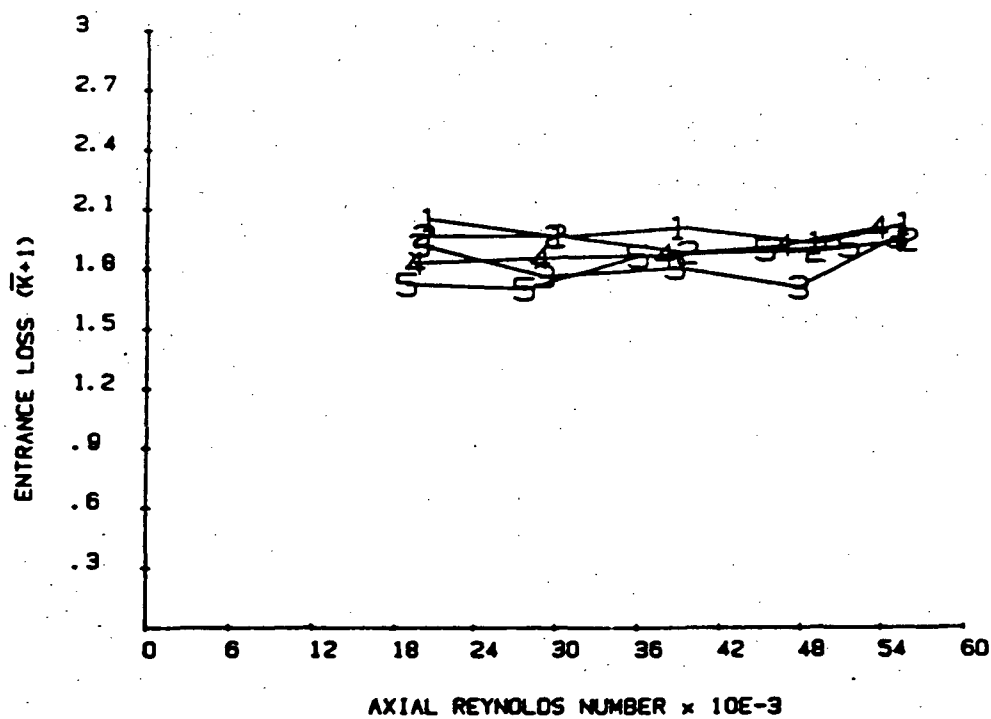
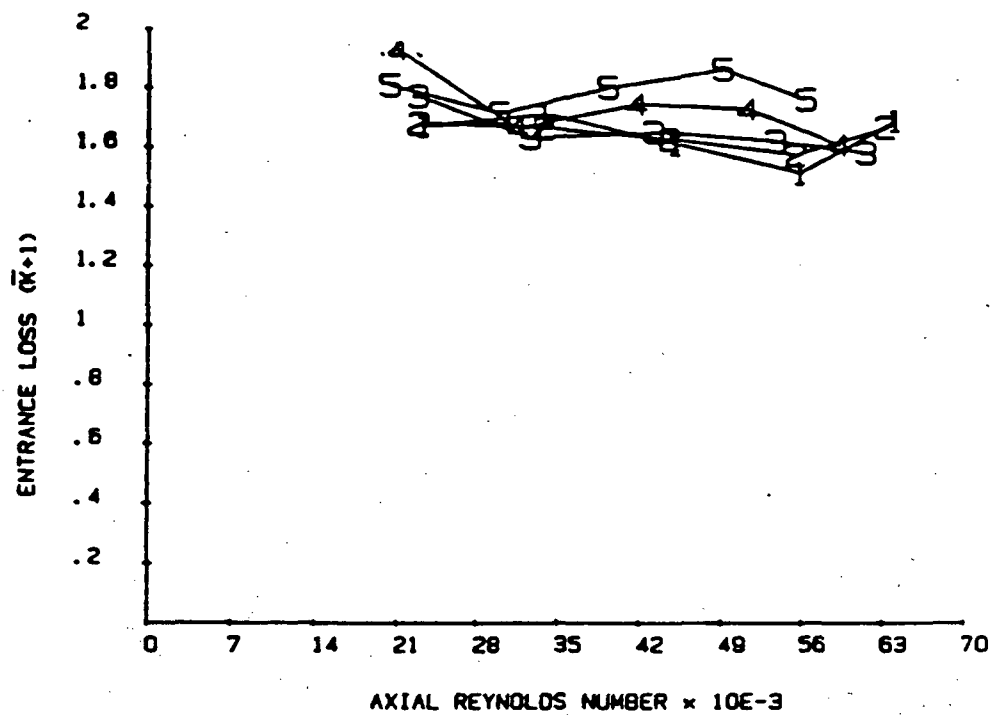


Fig. A23 Entrance losses of seal 2.0, inlet air swirls 4 (top) and 5 (bottom). Curves numbered by rotor speeds of Table 4.

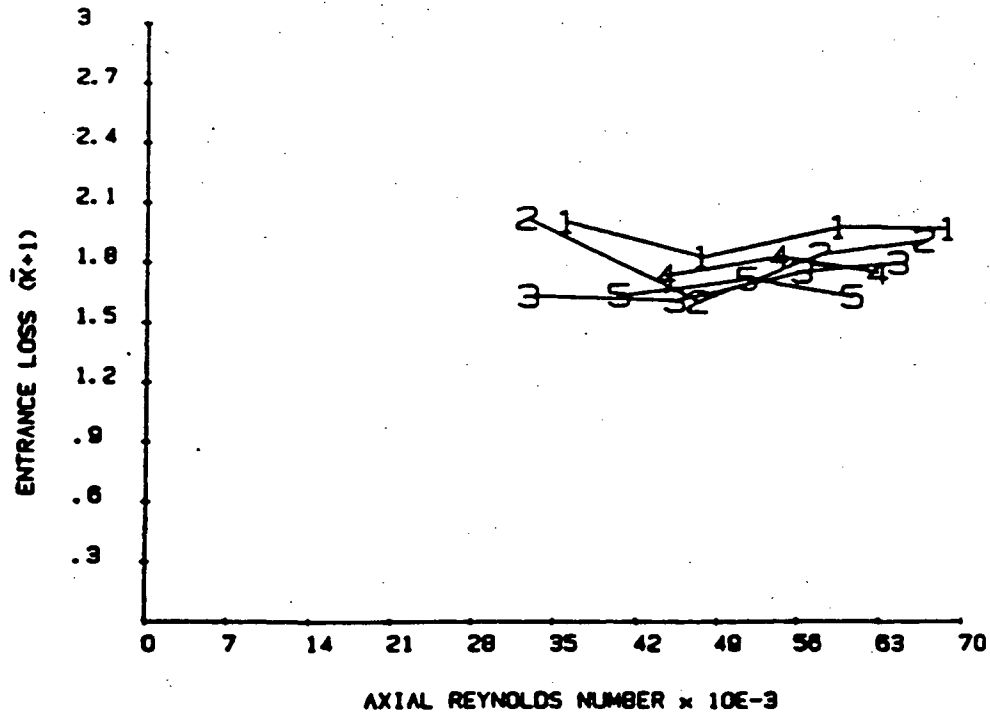
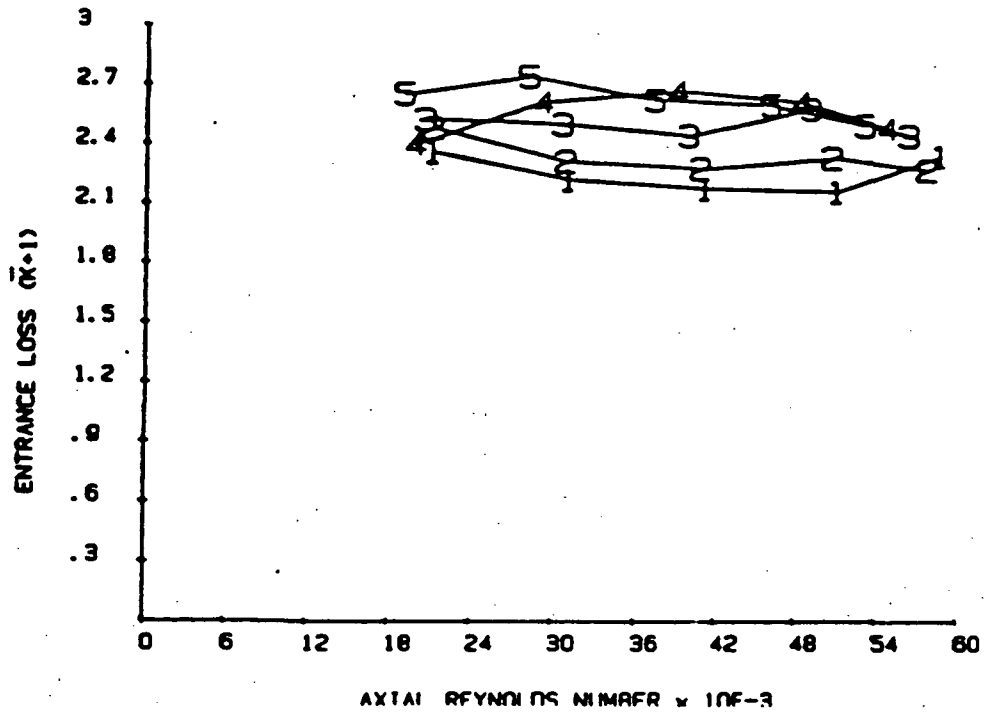


Fig. A24 Entrance losses of seal 2.5, inlet air swirl 1 (top) and 2 (bottom). Curves numbered by rotor speeds of Table 4.

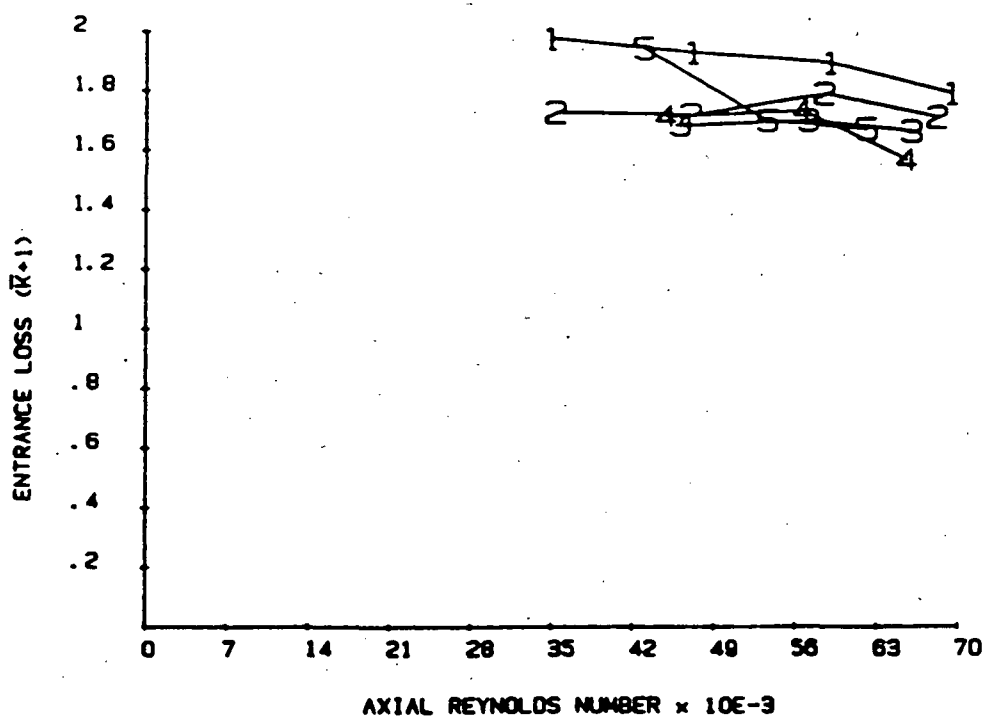
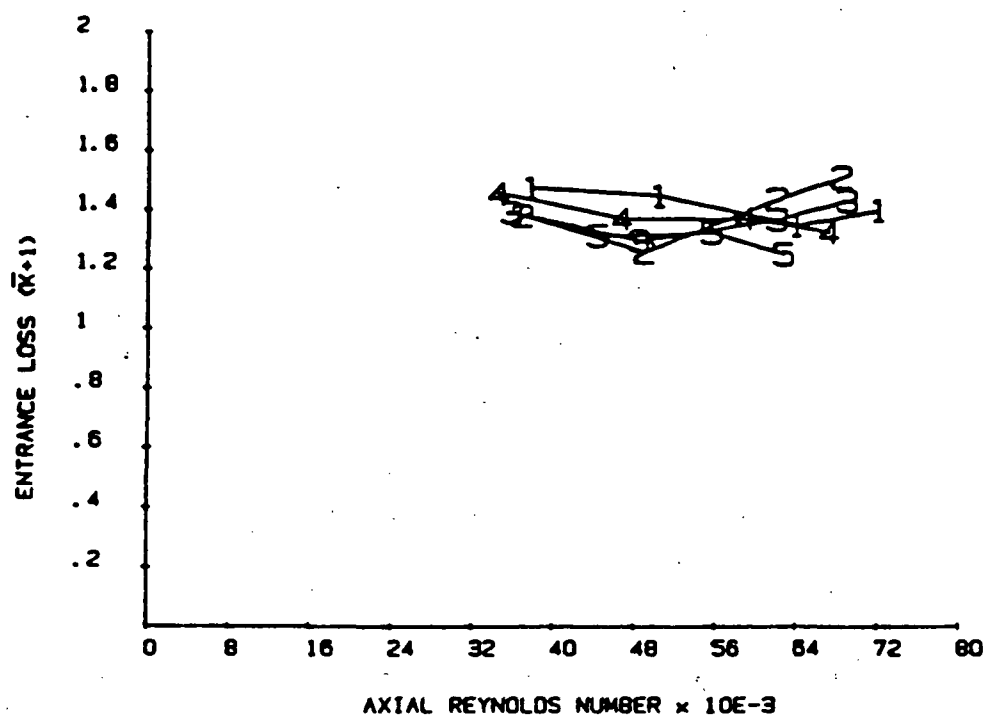


Fig. A25 Entrance losses of seal 2.5, inlet air swirls 3 (top) and 4 (bottom). Curves numbered by rotor speeds of Table 4.

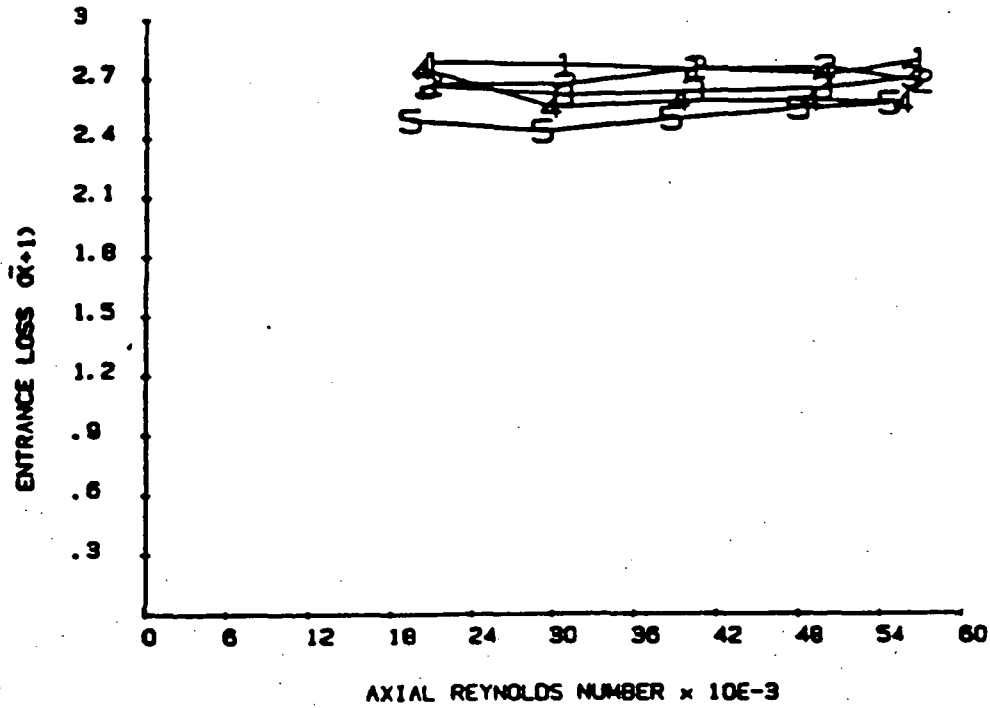


Fig. A26 Entrance losses of seal 2.5, inlet air swirl 5. Curves numbered by rotor speeds of Table 4.

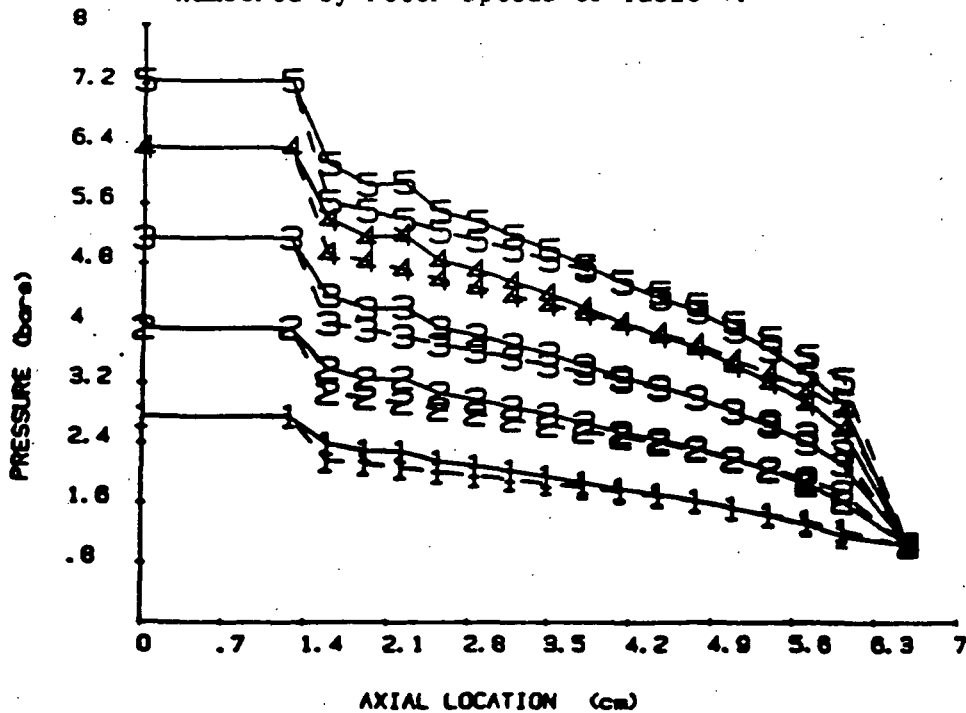


Fig. A27 Pressure gradients of seal 1.0, inlet swirl 1. Solid lines - experimental data; broken lines - theory.

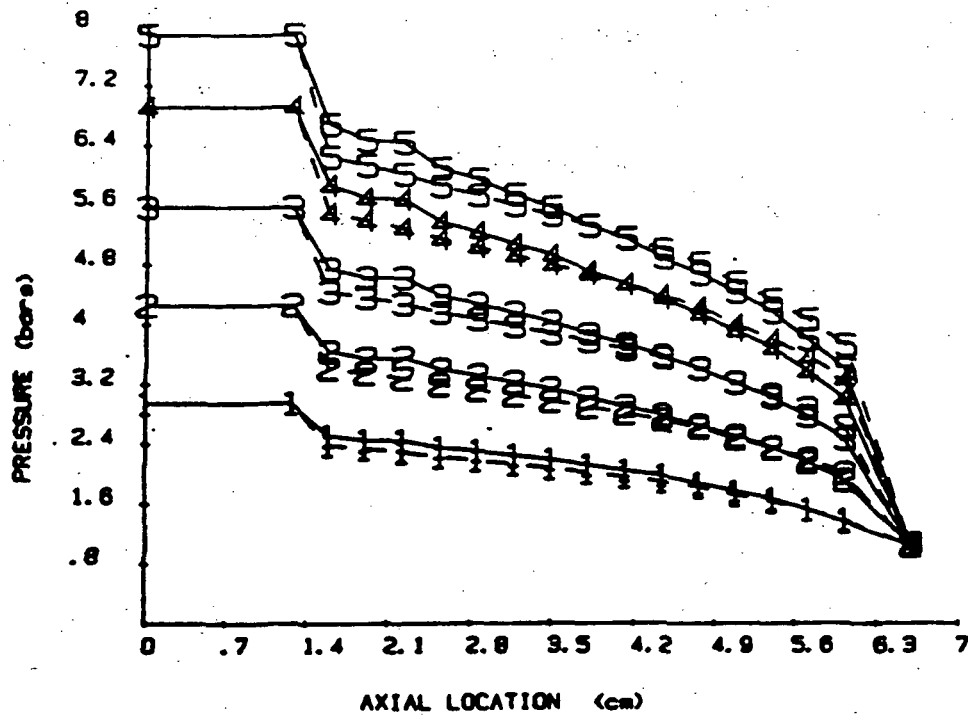
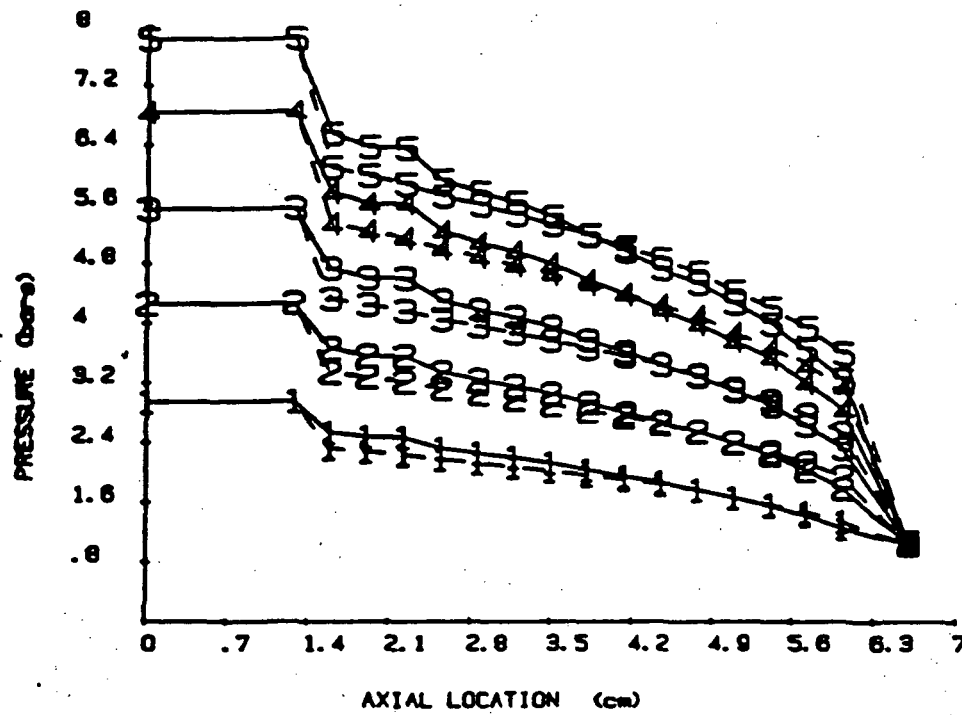


Fig. A28 Pressure gradients of seal 1.0, inlet air swirls 2 (top) and 3 (bottom). Solid lines - experiment; broken lines - theory

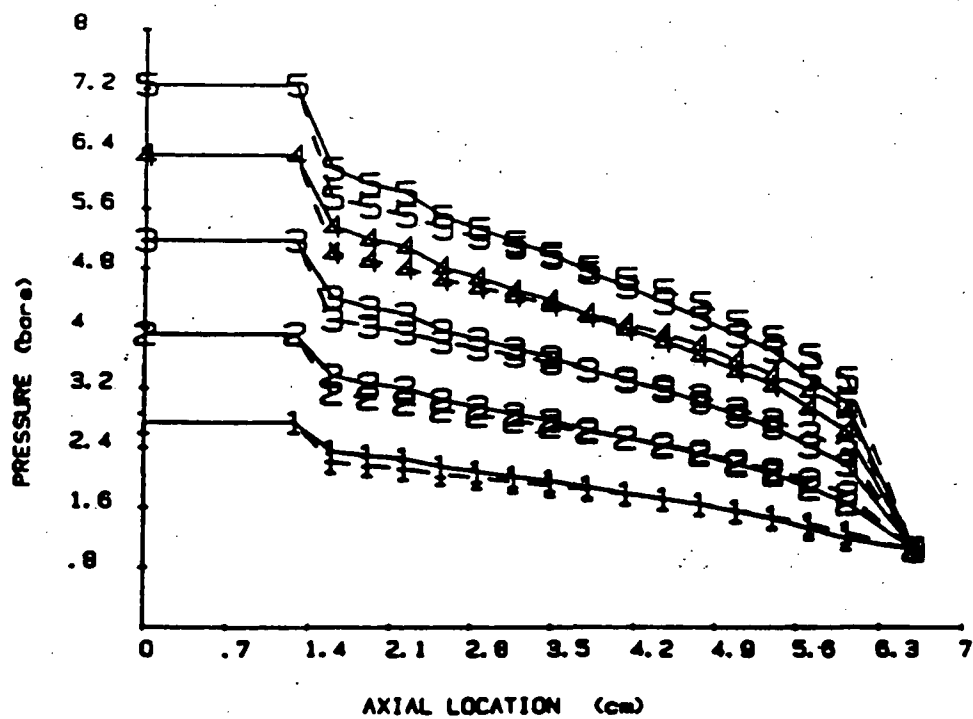
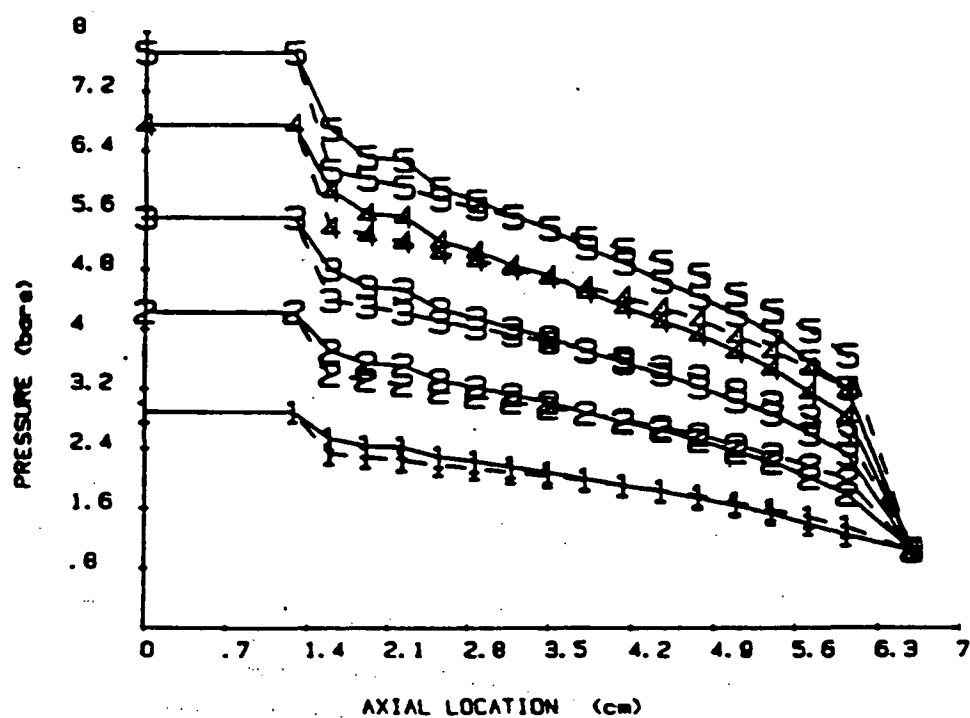


Fig. A29 Pressure gradients of seal 1.0, inlet air swirls 4 (top) and 5 (bottom). Solid lines - experiment; broken lines - theory

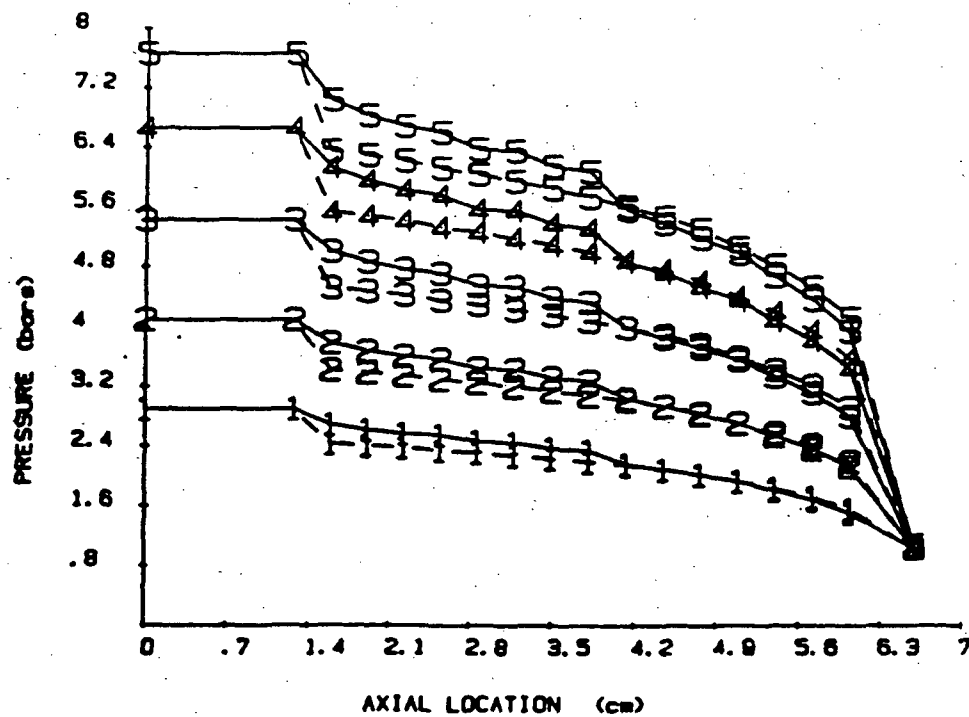
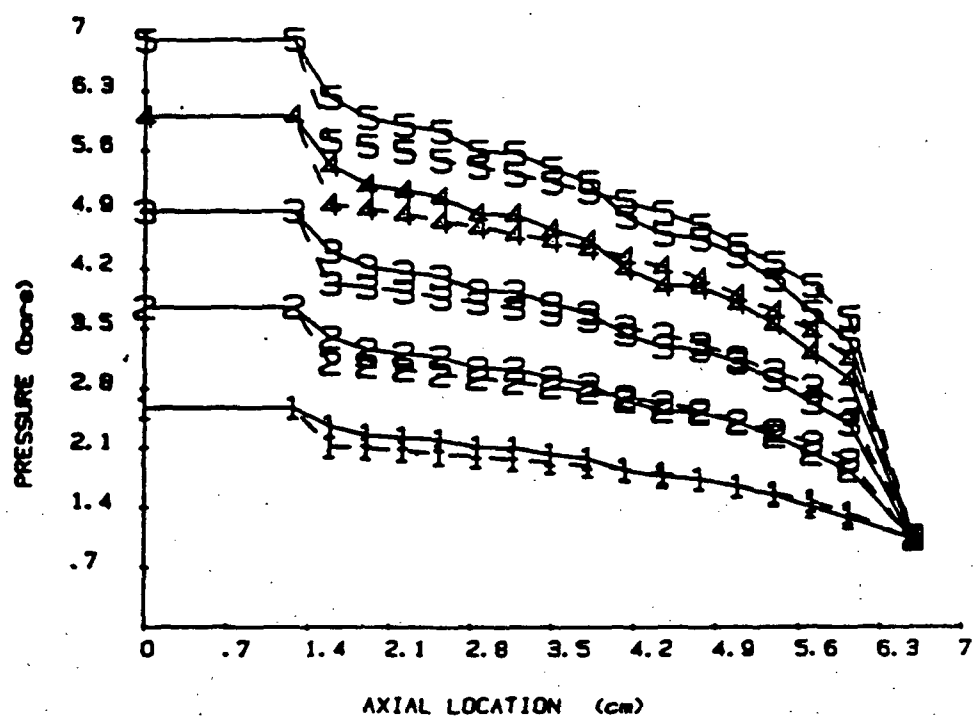


Fig. A30 Pressure gradients of seal 1.5, inlet air swirls 1 (top) and 2 (bottom). Solid lines - experiment; broken lines - theory

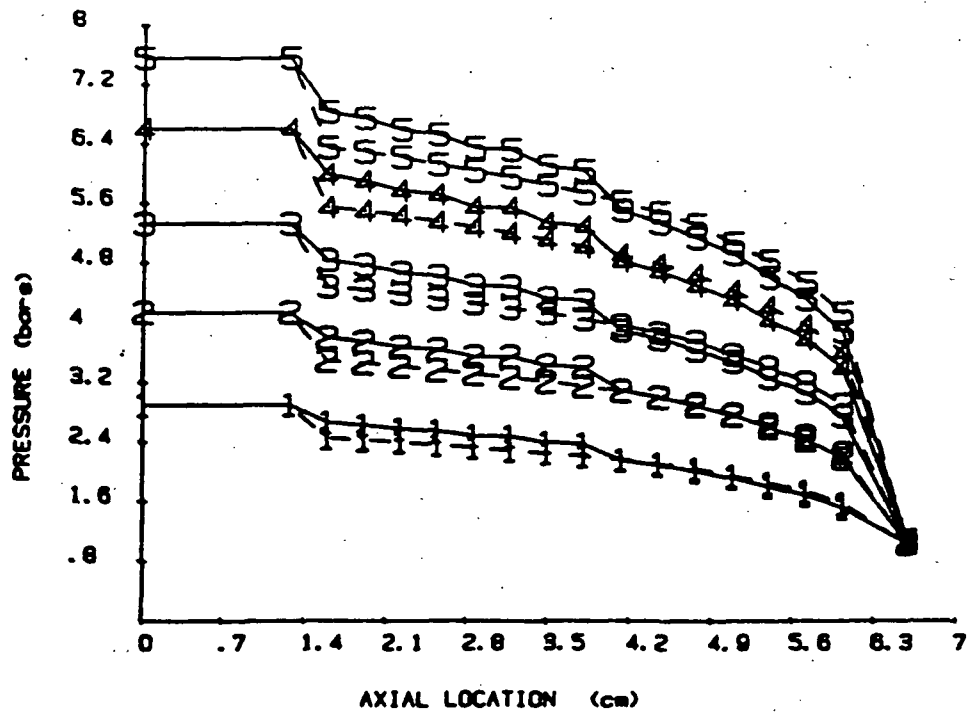
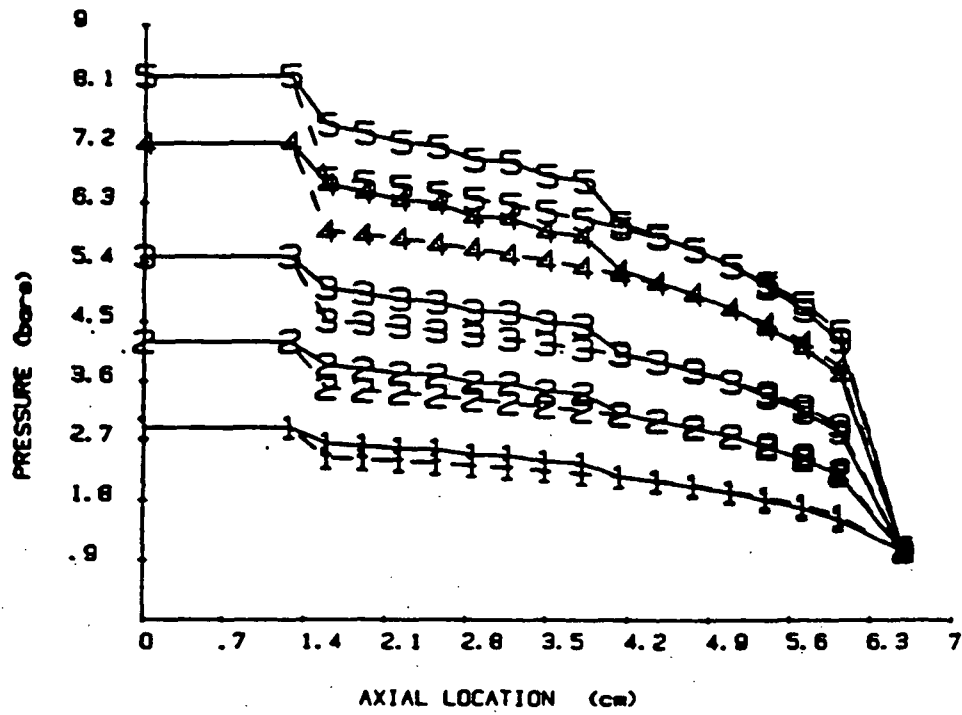


Fig. A31 Pressure gradients of seal 1.5, inlet air swirls 3 (top) and 4 (bottom). Solid lines - experiment; broken lines - theory

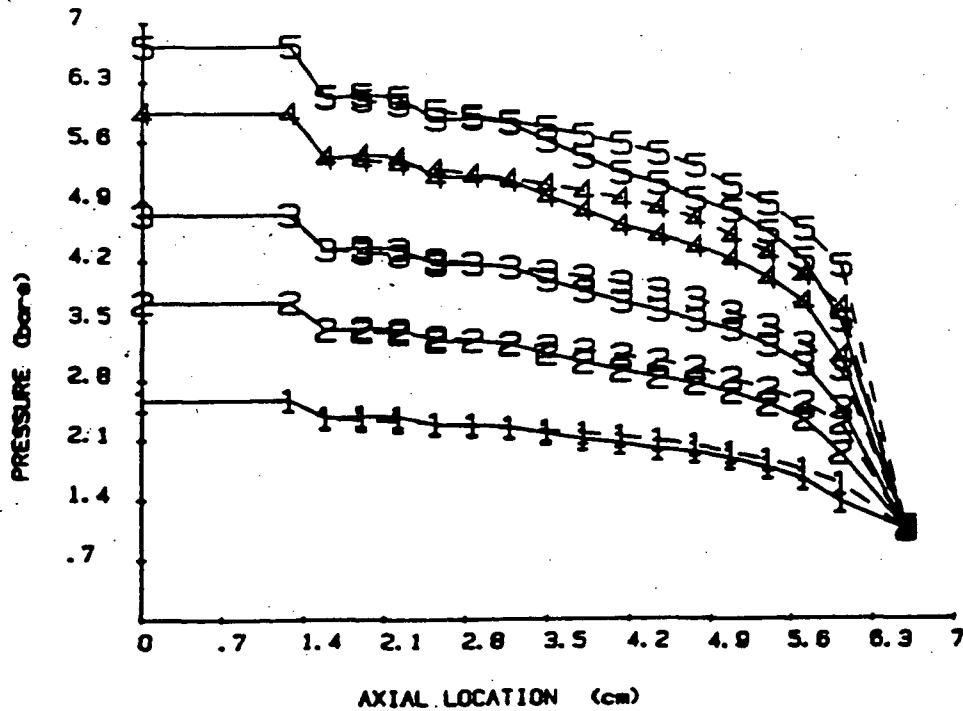
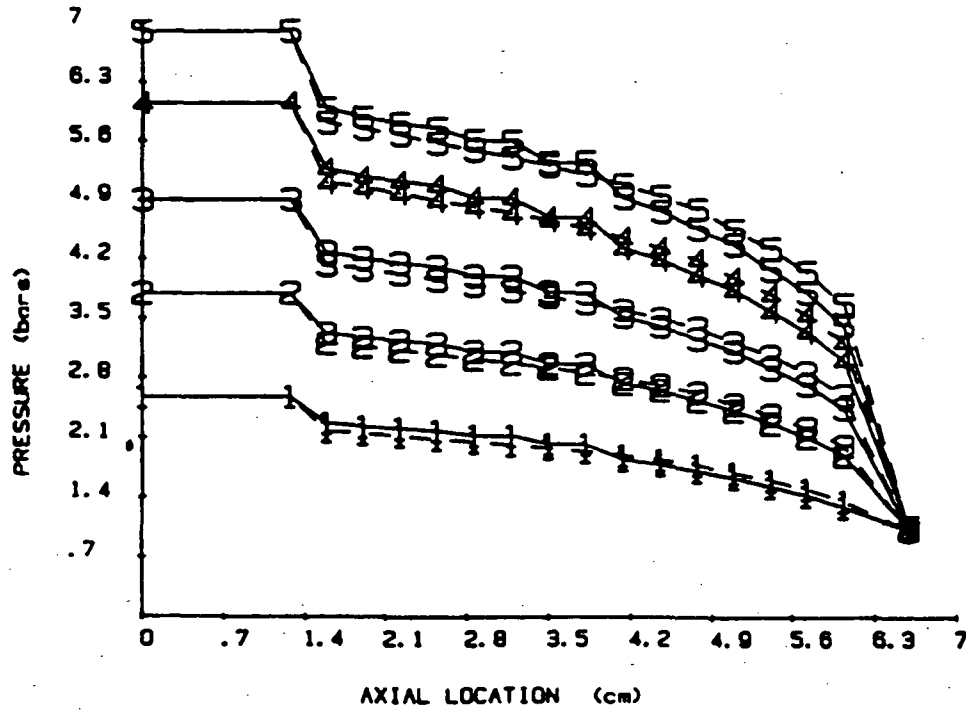


Fig. A32 Pressure gradients of seal 1.5 inlet air swirl 5 (top) and seal 2.0 inlet air swirl 1 (bottom). Solid lines - experiment; broken lines - theory. See Table 4 for symbol definitions.

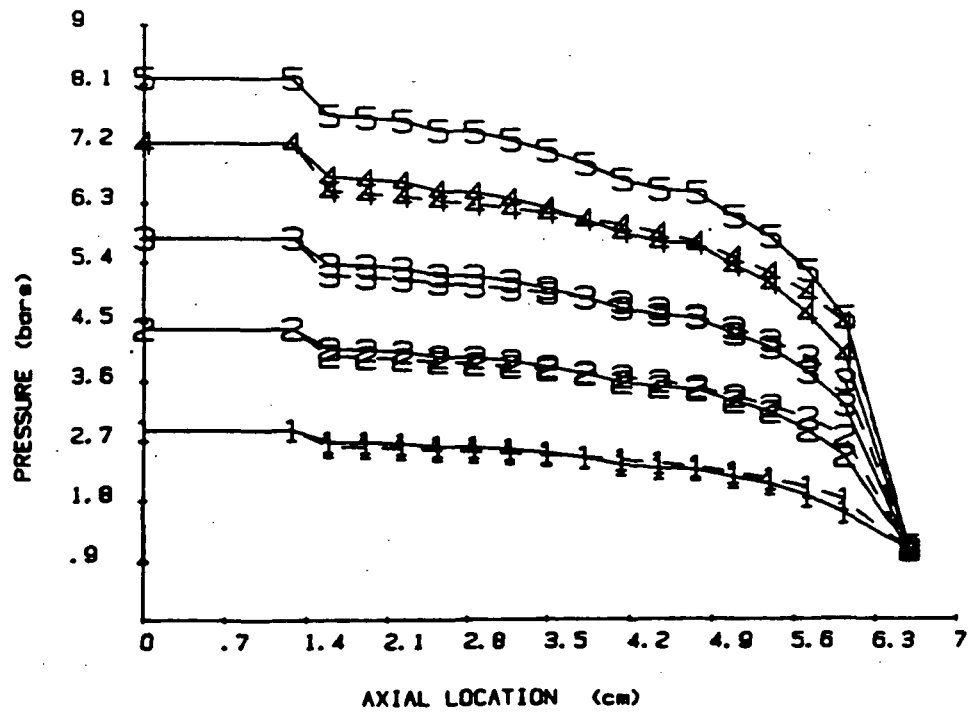
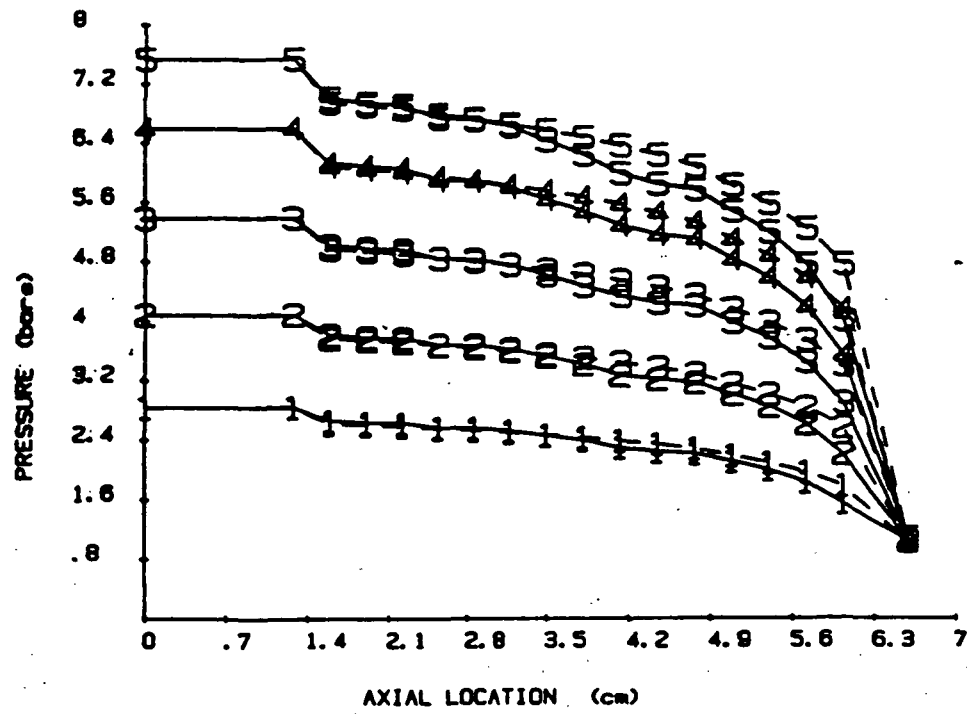


Fig. A33 Pressure gradients of seal 2.0, inlet air swirls 2 (top) and 3 (bottom). Solid lines - experiment; broken lines - theory

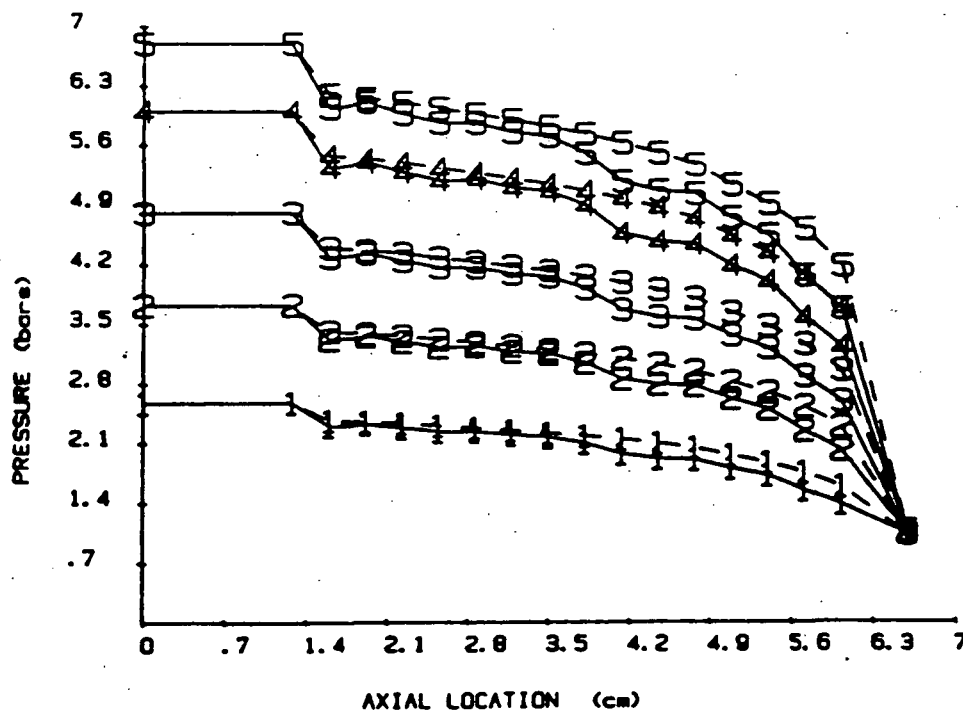
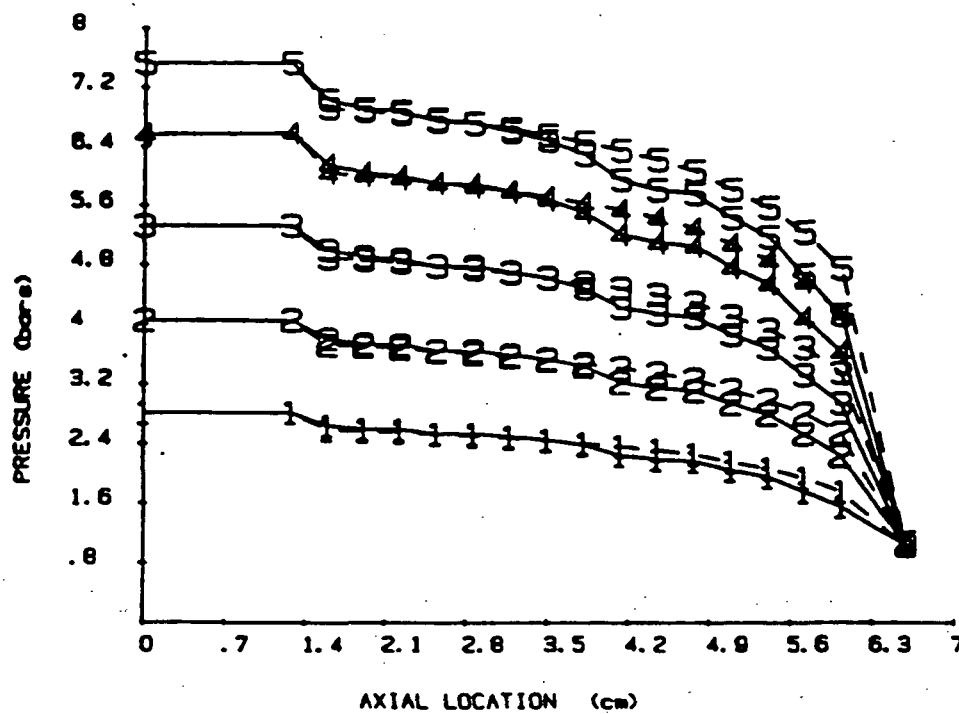


Fig. A34 Pressure gradients of seal 2.0, inlet air swirls 4 (top) and 5 (bottom). Solid lines - experiment; broken lines - theory

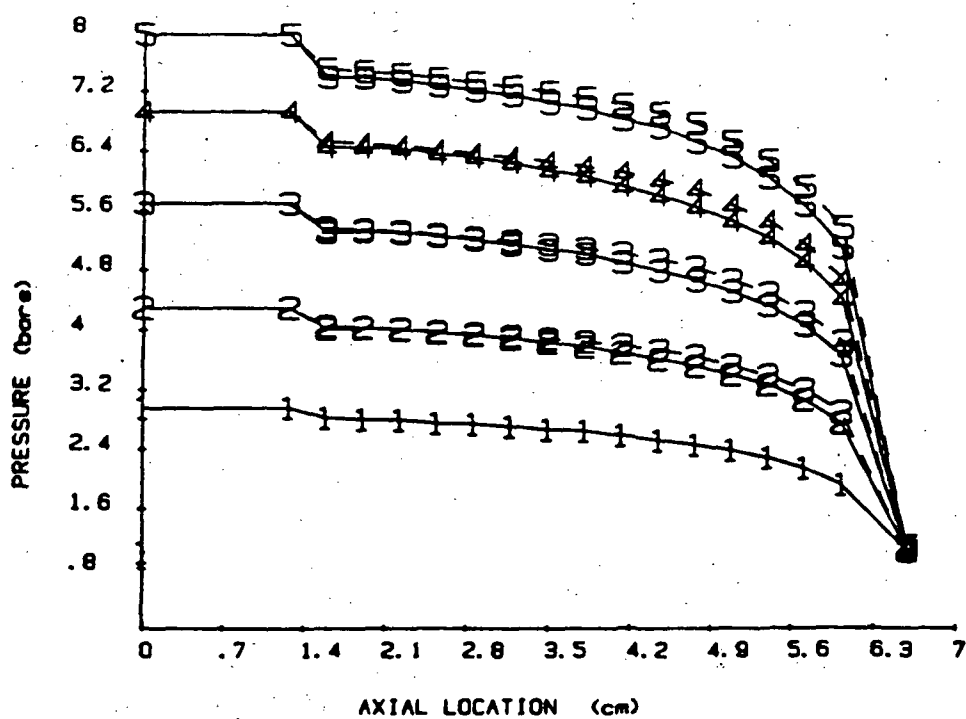
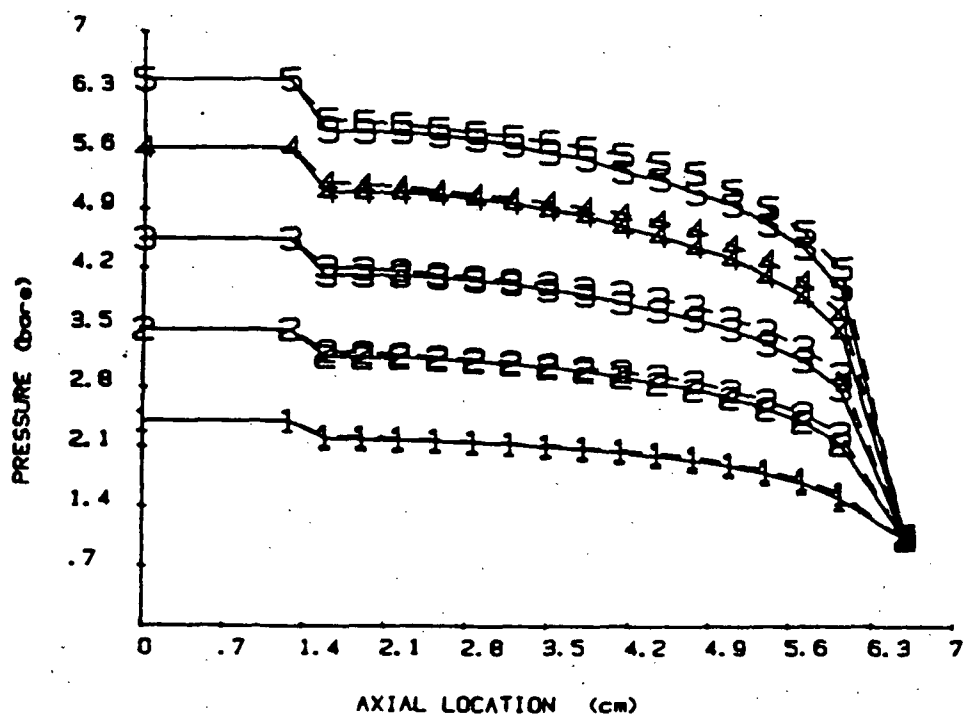


Fig. A35 Pressure gradients of seal 2.5, inlet air swirls 1 (top) and 2 (bottom). Solid lines - experiment; broken lines - theory.

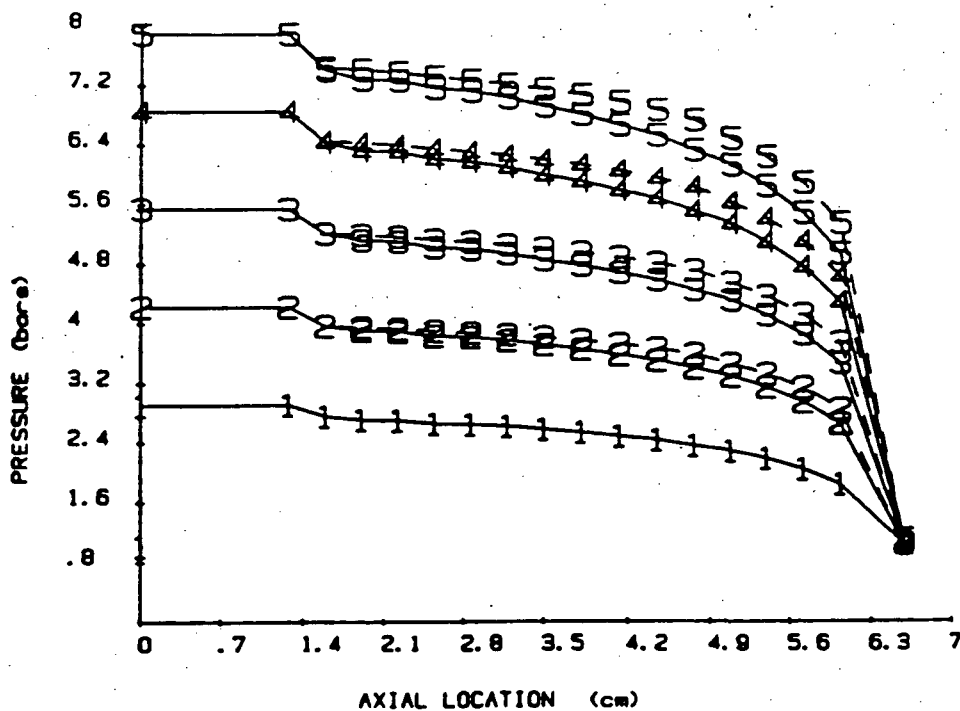
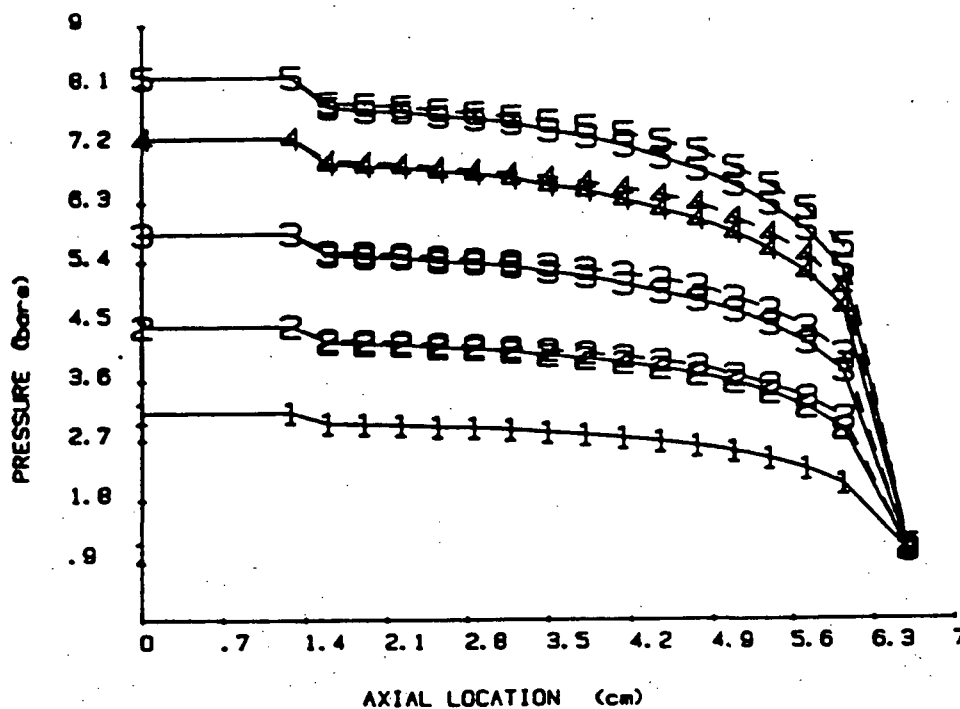


Fig. A36 Pressure gradients of seal 2.5, inlet air swirls 3 (top) and 4 (bottom). Solid lines - experiment; broken lines - theory

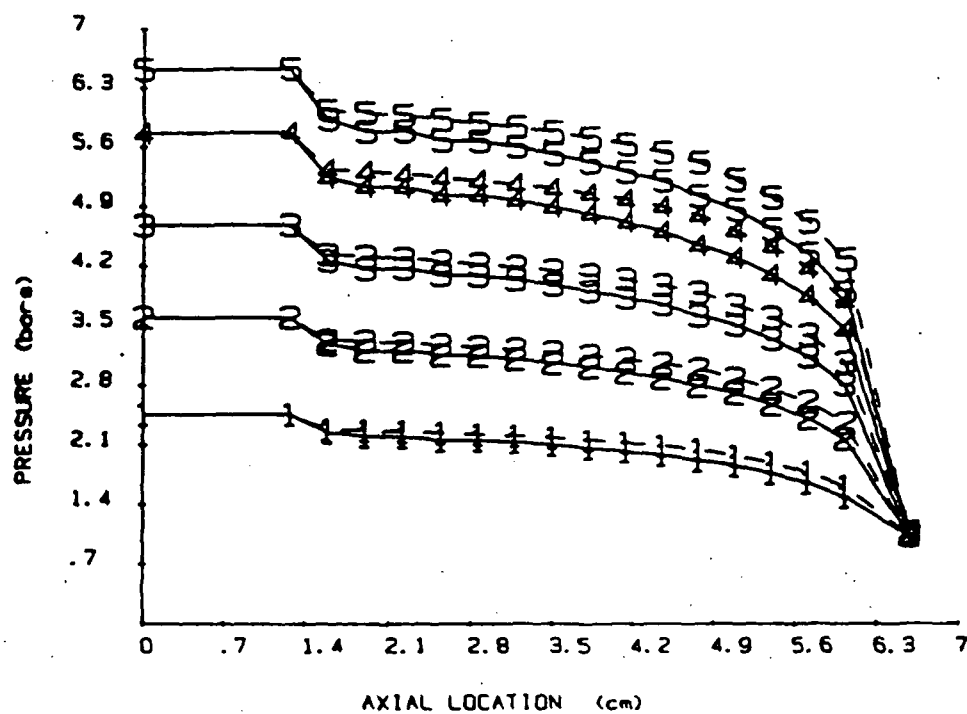


Fig. A37 Pressure gradients of seal 2.5, inlet air swirl 5.
 Solid lines - experiment; broken lines - theory.
 See Table 4 for definitions of symbols.

